

Evaluation of Biodegradable Magnesium Alloys for Orthopaedic Applications

Hyungseop Han

Wolfson College, University of Oxford

A thesis submitted for the degree of

Doctor of Philosophy

in Musculoskeletal Science

Hilary 2019

Abstract

The use of bio-materials in medical applications has risen exponentially in recent years, where applications range from the treatment of early stage disease to implants for major trauma. Particularly, research on biodegradable metallic materials have demonstrated potential step-change technologies which may revolutionise the treatment of broken bones. Implants made with biodegradable metals are significantly stronger than their polymer counterparts. They are also fully biodegradable *in vivo*, removing the need for secondary surgery. After a decade of laboratory and early translational research, these new materials are now showing significant clinical potential with the ability to create a paradigm shift in the way we treat musculoskeletal conditions.

To contribute to the clinical translation of the biodegradable metals, this thesis explored the biological response to a novel biodegradable Mg5wt%Ca-1wt%Zn alloy developed for orthopaedic repair, to study the bone remodelling process and assess the potential of the new implant. The main objectives of the research were to explore the impact of active Mg alloy biodegradation on the OB cells cultured in a perfusion bioreactor system and to further understand the bone healing process in and around a degrading Mg alloy by assessing angiogenesis and coupled osteogenesis at the Mg alloy implanted site.

Results demonstrate that the simulated key aspects of the *in vivo* environment recapitulated in these studies such as blood flow-induced magnesium corrosion, hydrogen evolution, and local pH change, contribute to a statistically significant increase in cellular proliferation and differentiation in the presence of degrading Mg alloys. The released ions from both fast and slowly degrading alloy showed a positive effect on the progress of bone formation. However, fast corroding alloy showed a detrimental effect on osteoblast cells, while osteoblast proliferation and differentiation were improved by released metal ions from optimized alloy with a much slower corrosion rate. These findings suggested that the release of metal ions consisting of Mg, Ca and Zn also sufficiently stimulate the bone formation process. *In vivo* experimental results observed using second harmonic generation and immunohistological staining confirmed that the optimized mechanical properties and corrosion rate of Mg-5wt%wt%Ca alloy leads to release of metallic Mg, Ca and Zn ions at a rate that facilitate both angiogenesis and coupled osteogenesis for better bone healing without causing adverse effect at the implantation site.
To conclude, this thesis tests a new *in vivo* model system to evaluate biodegradable metals and validate the potential of the newly developed Mg-Ca-Zn alloy as orthopaedic implant material. Furthermore, this work supports ongoing development and refinement of biodegradable metal systems to act as crucial portal technology with potential to revolutionize a myriad of clinical applications.

Acknowledgment

First of all, I would like to express my deepest gratitude and appreciation to my advisors, Prof. James Edwards and Prof. Sion Glyn-Jones for their continuous support and guidance which empowered me to complete my work at Oxford. I am also very thankful to Prof. Afsie Sabokbar for her supervision, cheerful encouragement, and useful suggestions throughout this research work.

I am very thankful to my closest friend and lab mate Dr. Indong Jun for his friendship and invaluable comments. The tea breaks after a long day of experiments were the highlights of many days in the lab.

I would like to thank Dr. Cathy Hua Ye and Dr. Pierre-Alexis Mouthuy for giving me thoughtful academic advice as examiners of the thesis.

It is with sincere appreciation that I thank the members of KIST team: Dr. Yu-Chan Kim, Dr. Hyun-Kwang Seok, Dr. Hojeong Jeon, Dr. Myoung-Ryul Ok, Mr. Jimin Park, Mr. Hyunsun Seo and U&I Corporation: President Ja-Kyo Koo, Director Sung Chul Hwang, Dr. Hwa Chul Jung for their assistance. This study has been made possible with the funding support from the U&I Corporation, Wolfson College and Clarendon Scholarship.

I am as ever, especially indebted to my parents, Seog-soo Han and Jeong-soon Lee for their unconditional love and support throughout my life. As mentors in my life, they taught me everything I know and provided me with strength and wisdom. I would like to express my love and appreciation to Duc Nguyen and Men Pham for their encouragement and support in life. I also wish to thank my brother, Euy-seop Han for keeping me focused during my study. Moreover, my sincere thanks go to Edwards Lab members: Prof. Claire Edwards, Dr. Emma Morris, Dr. Sam Olechnowicz, Dr. Srinivasa Rao, Dr. Beatriz Gamez Molina, Aneka Sowman, Christina Turner, Jessica Whitburn, Houfu Leng, Felix Richter.

Last but by no means least, it gives me an immense pleasure to thank the love of my life, Thuy-Duong N. Han and three sons Gil, Zune and Seung. I could never imagine a world without them and my work is dedicated entirely to them.

List of publications

Journal Papers

Hyung-Seop Han, Sergio Loffredo, Indong Jun, James Edwards, Yu-Chan Kim, Hyun-Kwang Seok, Frank Witte, Diego Mantovani, Sion Glyn-Jones. "Current status and outlook on the clinical translation of biodegradable metals." *Materials Today*, 2018, ISSN 1369-7021, https://doi.org/10.1016/j.mattod.2018.05.018.

Hyung-Seop Han, Gun Hyuk Jang, Indong Jun, Hyunseon Seo, Jimin Park, Sion Glyn-Jones, Hyun-Kwang Seok, Kwan Hyi Lee, Diego Mantovani, Yu-Chan Kim & James R. Edwards. "Transgenic zebrafish model for quantification and visualization of tissue toxicity caused by alloying elements in newly developed biodegradable metal." *Scientific Reports*. Volume 8, Article number: 13818 (2018).

Hyung-Seop Han (Co 1st Author), Hee-Kyoung Kim, Kang-Sik Lee, Dong-Ho Lee, Jee Wook Lee, Hojeong Jeon, Sung-Yoon Cho, Hyoung-Jin Roh, Yu-Chan Kim, Hyun-Kwang Seok. "Comprehensive study on the roles of released ions from biodegradable Mg–5 wt% Ca–1 wt% Zn alloy in bone regeneration." *Journal of tissue engineering and regenerative medicine*. Volume 11 (2017), Page 2710-2724.

Conferences

Hyungseop Han, James Edwards, Sion Glyn-Jones. “The Dissapearing Metal Bone Screws.” STEM for Britain 2018. Westminster, United Kingdom.

Hyungseop Han, James Edwards, Sion Glyn-Jones. “Development of Biodegradable Magnesium Alloy for Orthopaedic Applications.” 74th Annual International Magnesium Association (IMA) World Magnesium Conference. Singapore. 2017 Winner of Award of Excellence.

Abbreviations

ACL: anterior cruciate ligament

Al: Aluminium

ALP: alkaline phosphatase

AOFAS: American orthopedic foot and ankle society

ARCO: association of research circulation osseous

ATCC: American Type Culture Collection

Ca: Calcium

CC3: cleaved caspase 3

Ce: Cerium

CFDA: Chinese food and drug administration

cmlc: cardiac myosin light chain

Col I: collagen type I

CT: computed tomography

Dy: Dysprosium

EBM: endothelial basal medium

EGFP: enhanced green fluorescent protein

EGM: endothelial Cell Growth Medium

Er: Erbium

Eu: Europium

FBS: Fetal Bovine Serum

FDA: food and drug administration

Fe: Iron

FLIM: fluorescence lifetime imaging

flk: fetal liver kinase

Gd: Gadolinium

GFAP: glial fibrillary acidic protein

GDF-5: growth/differentiation factor 5

HA: hydroxyapatite

hFOB: human fetal osteoblast

Ho: Holmium

HUVEC: human Umbilical Vein Endothelial Cells

IL-1: interleukin-1

IL-6: interleukin-6

IL-11: interleukin-11

IL-16: interleukin-18

KFDA: Korea Food and Drug Administration

La: Lanthanum

lfabp: liver-type fatty acid-binding protein

LPS: lipopolysaccharide

Lu: Lutetium

M-CSF: macrophage colonystimulating factor

Mg: Magnesium

MTPJ: metatarsophalangeal joint

MSCs: mesenchymal stem cells

Nd: Neodymium

OB: osteoblast

OC: osteoclast

OCN: osteocalcin

olig: oligodendrocyte transcription factor

ONFH: osteonecrosis of the Femoral Head

OPN: osteopontin

PGA: poly(glycolic acid)

PLGA: poly(lactic acid-co-glycolic acid)

PLLA: poly(l-lactic acid)

Pr: Praseodymium

PVP: polyvinylpyrrolidone

RANKL: receptor activator of nuclear factor kappa B ligand

REEs: rare earth elements

RFP: red fluorescent protein

ROM: range of motion

SD: standard deviation

SDF-1: stromal cell-derived factor 1

SD rats: Sprague Dawley rats

SHG: second harmonic generation

Sm: Samarium

Tb: Terbium

TGF-β2: transforming growth factor-beta2

TGF-β3: transforming growth factor-beta3

Ti: Titanium

Tm: Thulium

TNF-α: tumor necrosis factor-α

TNFR1: tumor necrosis factor receptor 1

TNFR2: tumor necrosis factor receptor 2

TRAP: tartrate resistant acid phosphatase

UCS: ultimate compressive strength

UTS: ultimate tensile strength

VEGF: vascular endothelial growth factor

WST: water-soluble tetrazolium salt

Y: Yttrium

Yb: Ytterbium

YS: yield strength

ZOMB: Zebrafish Resource Bank

Zn: Zinc

Contents

1. Introduction 1

1.1 Background 1

1.2 Objectives 7

2. Literature Reviews 9

2.1 Orthopaedic application of biodegradable metals 9

2.2 The bone fracture healing process 11

2.2.1 Inflammation reaction phase 11

2.2.2 Renewal phase 13

2.2.3 Remodelling phase 14

2.3 Translational research on biodegradable metals 15

2.3.1. Pure Mg 18

2.3.2 Mg-Al alloys 20

2.3.3 Mg-Rare Earth alloys 22

2.3.4 Mg-Zn Alloys 25

2.3.5 Mg-Ca Alloys 28

2.3.6 Fe-based alloys 30

2.3.7 Zn-based Alloys 31

2.4 Clinical trials of biodegradable metallic screws 32

2.4.1 Pure Mg 33

2.4.2 MgYREZr Alloy (Magnezix) 35

2.4.3 MgCaZn Alloy (Resomet) 37

2.5 Development and optimization of Mg5Ca1Zn alloy 39

3. Comprehensive *in vitro* evaluation of Magnesium alloy ions and extracts 43

3.1 Introduction 43

3.2 Materials and Methods 47

3.2.1 Pure Mg and Mg alloy extracts preparation 47

3.2.2 Cell culture 48

3.2.3 Assessment of osteoblast proliferation 48

3.2.4 Measurement of cytosolic alkaline phosphatase (ALP) activity 49

3.2.5 Assessment of mineralized matrix formation 50

3.2.6 Measurement of Tartrate Resistant Acid Phosphatase (TRAP) activity 50

3.2.7 Resorption pit assay 51

3.2.8 Statistics 52

3.3 Results 53

3.3.1 Chemical composition and degradation profile of pure Mg and Mg alloy extracts 53

3.3.2 Effect of Mg alloy extracts on osteoblasts cells and bone formation in presence of released metallic ions 56

3.3.3 Effect on osteoclast activities by the Mg alloy extracts and in presence of released metallic ions 62

3.4 Discussion 66

3.5 Conclusion 71

4. Evaluation of bone formation using hydroxyapatite scaffold in a perfusion bioreactor 72

4.1 Introduction 72

4.2 Materials and Methods 75

4.2.1 Perfusion bioreactor for 3D cell culture 75

4.2.2 Micro-computed tomographic analysis 76

4.2.3 Molecular diffusivity experiment simulation 77

4.2.4 Cell culture 77

4.2.5 Adhesion of osteoblasts on Hydroxyapatite (HA) 79

4.2.6 Immunofluorescence staining for Cleaved Caspase-3 as an apoptosis marker 79

4.2.7 Fluorescence-activated cell sorting for cell proliferation 79

4.2.8 Second harmonic generation (SHG) 80

4.2.9 Assaying the levels of differentiated osteoblasts 81

4.2.10 Live computer tomography of rat femoral condyle 81

4.3 Results and Discussion 83

4.3.1 Flow-induced corrosion of Magnesium alloy implanted on hydroxyapatite scaffold inside the perfusion bioreactor 83

4.3.2 *in vitro* cellular response to flow induced loading and biodegradation of Mg alloy 87

4.4 Conclusion 98

5. Evaluation of angiogenesis and coupled osteogenesis from magnesium alloys 99

5.1 Introduction 99

5.2 Preliminary *in vitro* angiogenesis assay 101

5.2.1 Cell viability 101

5.2.2 Endothelial cell proliferation 104

5.2.3 Endothelial cell migration 105

5.2.4 Angiogenesis gene expression 107

5.3 Methods for *ex vivo* and *in vivo* study 113

5.3.1 Fetal Mouse metatarsal angiogenesis assay 113

5.3.2 Angiogenic cytokine arrays 113

5.3.3 Surgical preparation of *in vivo* model 114

5.3.4 Sample preparation for second harmonic generation and immunohistochemistry 114
5.3.5 Second harmonic generation 115
5.3.6 Immunohistochemistry 115
5.3.7 Cell sorting by flow cytometry 116
5.4 Results and Discussion 117
5.4.1 Fetal mouse metatarsal assay for evaluation of angiogenetic effect from degrading particles 117
5.4.2 Evaluation of collagen profile near implanted Magnesium implant through second harmonic generation 122
5.4.3 Immunohistological evaluation of degrading implant 127
5.5 Conclusion 137
6. Zebrafish model for evaluation of *in vivo* toxicity for biodegradable metals 138
6.1 Introduction 138
6.2 Materials and Methods 142
6.2.1 Cell cultures 142
6.2.2 Cell viability assay 142
6.2.3 Zebrafish models 143
6.2.4 Chemical treatment of zebrafish embryos 143
6.2.5 Zebrafish embryo developmental toxicity test 144

6.2.6 Examination of heart function 144

6.2.7 Statistical analysis 144

6.3 Results and Discussion 146

6.3.1 Effects of MgCl2, ZnCl2, and CaCl2 *in vitro* and in a zebrafish model ..146

6.3.2 Biological effects of YCl3 *in vitro* and in a zebrafish model 153

6.3.3 Biological effects of AlCl3 in a zebrafish model 155

6.4 Conclusions 159

7. Conclusions and Future Work 161

7.1 Conclusions 161

7.2 Future Work 165

Bibliography 168

Appendix 196

List of Figures

Figure 1.1. The process of biodegradation for metals.

Figure 1.2. Timeline of representative clinical trials of biodegradable metals in cardiology (red) and orthopaedics (grey).

Figure 2.1. Optimal degradation behaviour of Mg-based implant in bone fracture healing.

Figure 2.2. Current state-of-the-art applications of biodegradable metals. (a) Clip applier with operative Mg clip, (b) MgF2 coated Mg-2wt%Nd alloy nasal stent, (c) Loaded Mg microclip in microlaryngeal forcep, (d) Mg stent for neurological application, (e) Mg-based intramedullary nail. Devices at clinical stages – (f) Resomet orthopaedic devices, (g) DREAMS 2nd generation stent, (h) Magnezix screw and pin, (i) Iron-based suture anchor, (j) Velox CD vascular closure device, (k) Pure Mg Screws.

Figure 2.3. (a) Pitting corrosion of pure Mg observed with SEM. (b) magnified view of local corrosion initiation point. (c) WDS element mapping of the corresponding region showing Fe impurity in the area of (b). (d) corrosion rate of pure Mg depending on the impurity of Mn.

Figure 2.4. Slow and gradual degradation rate of LAE442 sample observed by loss of residual density and volume over 72 weeks in rabbit tibia.

Figure 2.5. Micro-CT and histological analysis of WE43 alloy screw implanted on mandible of miniature pigs for 12 and 24 weeks. Mg implants with plasmaelectrolytic coating show absence of gas cavity.
Figure 2.6. Comparison of hydrogen gas cavity formation for (a) Mg metallic glass material and (b) crystalline Mg alloy implanted on subcutaneous tissue of pigs.
Figure 2.7. Difference in formation hydrogen gas pockets and recovered implants from subcutaneous tissue of SD rats after 12 weeks. (a) casted Mg-Ca alloy, (b) extruded Mg-Ca alloy, (c) casted Mg-Ca-Zn alloy, and (d) extruded Mg-Ca-Zn alloy.
Figure 2.8. X-ray image of patient that received implantation of pure Mg screws at (a) preoperation, (b) 3 months, (c) 6 months, and (d) 12 months. (Zhao, Huang et al. 2016)
Figure 2.9. 16-month postoperation X-ray image of 29-year-old female patient that received MgYREZr alloy screw after distal metatarsal osteotomy.
Figure 2.10. Representative clinical trial result of the Resomet implant. Scaphoid fracture was treated with conventional stainless-steel pin whereas distal radius fracture was treated with Mg alloy screw. After 1 year, fracture site shows complete degradation of Mg alloy screw and bone healing.
Figure 2.11. Development of in-house melting furnace and extrusion machine for optimization of material development process.
Figure 2.12. Microstructure of optimized Mg5Ca1Zn alloy after extrusion.
Figure 2.13. Toludine blue stain and micro CT image of mg alloy screw implanted on femoral condyle of New Zealand white rabbits for 12 weeks.
Figure 3.1. Cell viability of metal ions and alloy extract samples. The cytotoxicity of Mg,Ca, Zn ions and extracts from control Titanium alloy(Ti64), pure Mg and

Mg5Ca1Zn alloy samples were determined respectively. hFOB1.19 cells and RAW264.7 cells were cultured with test ions/extracts for 24 hours and the cytotoxicity was measured by using Cell Counting Kit-8 (CCK-8). The cytotoxicity of (a) hFOB1.19 and (b) RAW264.7 in presence of 1~64mM of MgCl2, 1~64mM of CaCl2 and 1~1000uM of ZnCl2. The cytotoxicity of (c) hFOB1.19 and (d) RAW264.7 in prepared alloy extracts.

Figure 3.2. hFOB1.19 proliferation in presence of alloy extracts and metal ions. Cells were cultured for 3 continuous days in test samples and cell proliferation ELISA BrdU kit was used to measure the proliferation. The colorimetric changes were read at 370 nm. (a) hFOB1.19 proliferation in extracts from Ti64 and Mg alloy. (b) hFOB1.19 proliferation in presence of 1~20mM of $MgCl_2$ and (c) 1~50uM of $ZnCl_2$.

Figure 3.3. The ALP activity evaluation of hFOB1.19 cells cultured with metallic ions and alloy extracts. The cells were cultured for 7 continuous days in media containing test samples supplemented with differentiation factors. The ALP activity of cell lysates was measured and normalized to total cellular protein content. (a) The ALP activity from differentiated hFOB1.19 cells in pH-uncontrolled and pH-controlled test sample extracts. (b) The ALP activity from differentiated hFOB1.19 cells in the presence of 1~20mM of $MgCl_2$ and 1~50uM of $ZnCl_2$.

Figure 3.4. Evaluation of extracellular matrix mineralization of hFOB1.19 cells in the presence of test sample extracts by alizarin red-S staining. The cells were cultured for 30 continuous days with test sample extracts supplemented with differentiation factors and mineralized matrix was detected with alizarin red-S staining.

Figure 3.5. Evaluation of extracellular matrix mineralization of hFOB1.19 cells in presence of Mg and Zn ions. The cells were cultured for 30 continuous days with differentiation culture media containing 1~20mM of $MgCl_2$ and 1~50uM of $ZnCl_2$ for and mineralized matrix was detected with alizarin red-S staining. (a) AR-S staining of hFOB1.19 in presence of Mg and Zn ions. (b) Quantitative results summarized in graph.

Figure 3.6. Evaluation of RAW264.7 cell activity in pH uncontrolled and controlled alloy extracts. The cells were cultured for 5 continuous days with test sample extracts supplemented with differentiation factors. (a) The AP activity of differentiated RAW264.7 in test alloy extracts at 5 days normalized to total cellular protein content. (b) TRAP staining and resorption pit assay of differentiated RAW264.7 cells.

Figure 3.7. Evaluation of RAW264.7 cell activity in presence of Mg and Zn ions. The cells were cultured for 5 continuous days with differentiation culture media containing 1~20mM of MgCl2 and 1~50uM of ZnCl2. (a) Quantified AP activity of differentiated RAW264.7 cells in presence of 1~20mM of MgCl2 and 1~50uM of ZnCl2 normalized to total cellular protein content. (b) TRAP staining and resorption pit assay of differentiated RAW264.7 cells. Scale bar represents 50 μm.

Figure 3.8. The quantitative analysis of pro-inflammatory cytokine IL-1β (a),IL-6 (b) and TNF-α (c) in RAW264.7 cultured in presence of 100ng/ml of LPS and alloy extracts or metal ions.

Figure 4.1 Figure 4.1 U-Cup direct perfusion bioreactor installed in incubator (adapted from Cellec Biotek AG).

Figure 4.2 HA scaffolds implanted with Mg5Ca1Zn sample (1 mm in diameter and 2 mm in length) and uCT image of the implanted sample in the HA scaffold.
Figure 4.3 Schematic of 3D cell culture process. HA scaffold implanted with Mg alloy sample is placed in the chamber of perfusion bioreactor and medium is circulated through the chamber. hFOB 1.19 Cells (2x106) are seeded on top of the HA scaffold and then cultured under perfusion.
Figure 4.4 μCT comparison of Mg5Ca1Zn samples immersed in static conditions with a thick layer of corrosion by-product on the surface of Mg and perfusion condition without accumulation of corrosion by-product on the surface after 4 weeks.
Figure 4.5 4 weeks postoperation *in vivo* CT of femoral condyle of SD rat implanted with Mg5Ca1Zn.
Figure 4.6 Confocal Z stack image showing human fetal osteoblastic cell proliferation and penetration through 1mm wide and 2 mm deep defect made on HA scaffold under static and perfusion condition after 1 day of culture.
Figure 4.7 Water molecular diffusivity simulation showing the flow of media through the open porous structure of hydroxyapatite scaffold.
Figure 4.8 Cytoskeletal structures hFOBs after 24 h of culture on the HA, Mg-based alloy implanted HA and titanium implanted HA. The images were acquired by fluorescence staining for F-actin (red), and DAPI (nuclei)
Figure 4.9 FACS results of hFOB proliferation after 24 h of culture under static and dynamic conditions using control HA, HA implanted Titanium and HA implanted with two different type of Mg-based alloys. The intensity value of BrdU from each sample

was measured for comparison.

Figure 4.10 Analysis of apoptosis by Cleaved Caspase-3 staining (a) representative images of hFOBs stained for Cleaved Caspase-3. (b) Quantification of Cleaved Caspase-3 positive cells.

Figure 4.11 Quantification of DNA contents

Figure 4.12 (a) Second harmonic generation (SHG) imaging of cells on metal alloy. (b) ELISA analysis of the Collagen I content of cells on metal alloy.

Figure 4.13 Quantification of production of (a) ALP, (b) OCN and (c) OPN bone protein.

Figure 5.1 Live and dead staining of HUVEC depending on different concentration of Mg, Ca and Zn ions.

Figure 5.2 Cellular viability of HUVEC treated with increasing concentration of Mg, Ca and Zn ions.

Figure 5.3 Proliferation of HUVEC treated with different concentration of Mg, Ca and Zn ions over time.

Figure 5.4 Scratch assay test on HUVEC treated with Mg ions at 0, 8, 16 hr post-injury.

Figure 5.5 Scratch assays test on HUVEC treated with Ca ions at 0, 8, 16 hr post-injury.

Figure 5.6 Scratch assays test on HUVEC treated with Zn ions at 0, 8, 16 hr post-injury.

Figure 5.7 Expression of proangiogenic genes after 72 hours from HUVEC treated with increasing content of Mg ions
Figure 5.8 Expression of proangiogenic genes after 72 hours from HUVEC treated with increasing content of Mg ions
Figure 5.9 Expression of proangiogenic genes after 72 hours from HUVEC treated with increasing content of Zn ions
Figure 5.10 Quantified vessel density after 5 days of culture in alpha-MEM treated with different concentration of Mg, Ca and Zn ions.
Figure 5.11 (a) Representative fluorescent images of CD31 positive vessel outgrowth from metatarsal growth under different types of metal alloys. (b) Quantification of vessel density
Figure 5.12 Heat map of angiogenic cytokine expression
Figure 5.13 live μCT image of fast degrading Mg alloy in SD rats.
Figure 5.14 Thick cryosection of femoral condyle of SD rats implanted with Mg5Ca1Zn sample for 4 weeks and resulting SHG image of collagen deposits on the surface of implanted Mg5Ca1Zn sample.
Figure 5.15 SHG images of normal SD rat femur, empty defect site, titanium, Mg5Ca1Zn samples after 2 and 4 weeks postoperation. Scale bar represents 10 mm in length and white dash lines represent the original defect created during surgery.
Figure 5.16 Confocal microscropy images of immunostained sections from normal bone, empty defect site, titanium, Mg5Ca1Zn samples after 4 weeks postoperation (Endomucin – Red, Osterix – Green, DAPI – Blue).

Figure 5.17 High resolution confocal microscropy images of immunostained sections Mg5Ca1Zn samples after 4 weeks postoperation (Endomucin – Red, Osterix – White, DAPI – Blue).
Figure 5.18 Flow cytometry dot plots showing expression of PECAM and Endomucin from the cells collected from femoral head of SD rats with empty defect site, Titanium or Mg5Ca1Zn after 2 and 4 weeks postoperation.
Figure 5.19 Flow cytometry dot plots showing expression of Osterix and Endomucin from the cells collected from femoral head of SD rats with empty defect site, Titanium or Mg5Ca1Zn after 2 and 4 weeks postoperation.
Figure 6.1. The *in vivo* toxicity assessment of most commonly used biodegradable metal alloying elements in zebrafish.
Figure 6.2. Evaluation of biological effect from increasing concentration of Mg, Zn, and Ca ions. (a) *in vitro* cellular viability of HL-1, Huh7 and HUVEC after treatment with different concentration of Mg, Zn, and Ca ion solution for 12 h. (b) Biological status of Zebrafish embryos (normal or defects) at 6 hpf after treatment with indicated concentration of Mg, Zn and Ca ion solutions. (c) Biological defects rate in Zebrafish embryos at 6 hpf after treatment with indicated concentration of Mg, Zn and Ca ion solutions.
Figure 6.3. (a) Biological defects from ion treated Zebrafish embryos at 72 hpf (b) The change in the heart size of ion treated Zebrafish embryos after 96 hpf. (c) The heart rate of zebrafish embryos subsequent to 72 and 96 hpf treatments with increasing concentrations of Mg, Zn, and Ca ions. (d) Relative liver size area of

zebrafish embryos after treatment with 64 mM Mg. 500 μM Zn, and 128 mM Ca ions. (e) The change in liver size of ion-treated zebrafish embryos at 96 hpf.

Figure 6. 4. (a) Cellular viability of HL-1, Huh7, and HUVEC after treatment of Mg, Zn, and Ca ion solutions for 12 h. (b) Biological status of Zebrafish embryos (normal or defects) at 6 hpf after treatment with indicated concentration of Y ion solutions. (c) Biological defects rate in Zebrafish embryos at 6 hpf after treatment with indicated concentration of Y ion solutions. (d) Biological defects from ion treated Zebrafish embryos at 72 hpf. (e) The heart rate of zebrafish embryos subsequent to 72 and 96 hpf treatments with increasing concentrations of Y ions. (f) The change in liver size of ion-treated zebrafish embryos at 96 and 168 hpf. (e) Relative liver size area of zebrafish embryos after treatment of Y ions 96 hpf and 168 hpf.

Figure 6. 5. Biological effect of Al^{3+} *in vitro* and in a zebrafish model. (a) Viability of HL-1 and Huh7 cells and HUVEC after treatment with indicated ion solutions for 12 h. (b) Biological status of embryos (normal or defects) at 6 hpf after treatment with indicated ion solutions. (c) Biological defects in embryo at 6 hpf after treatment with indicated ion solutions. (d) Representative images of ion-treated zebrafish embryo used to determine heart rate. (e) Mean heart rate of zebrafish embryos following 48-, 72-, and 96-h treatments with different concentrations of Al^{3+}. (f) Representative images of ion-treated zebrafish embryo used to determine liver size at 96 and 168 hpf. (e) Mean liver size of zebrafish embryos following 96-and 168-h treatments with indicated concentrations of Al^{3+}.

Figure 6.6. Evaluation of Al ion on neuronal growth A) Tg(olig2:DsRed) zebrafish treated with 100 μM of Al ion after 144 hpf. B) Tg(GFAP:EGFP) zebrafish treated with 100 μM of Al ion after 144hpf.

List of Tables

Table 2.1. Summary of recent clinical trials of orthopaedic devices

Table 3.1. Chemical composition (wt.%) of Mg alloys.

Table 3.2. Change of pH over time and accumulation of released ions from the alloy extracts. Values are expressed as the mean ± standard deviation from the mean.

Table 5.1 The oligonucleotide primer sequences

Table 6.1. Measured heartrate per 15 second after treatment with different concentration of Mg, Zn, Ca, Y, Al ions 48, 72 and 96 hpf

Table 6.2. Detailed recorded biological defects from increasing concentration of alloying elements

Chapter 1

Introduction

1.1 Background

The recent decades have evidenced an unprecedented rise in the use of biomaterials, particularly in the field of medical application. The associated improvement in medical treatments combined with enhanced knowledge of chronic medical conditions has thus yielded a more active ageing population as compared to the preceding generation. While such demographic transition has altered the scope of treatment for several terminal medical conditions, an increase in the active ageing population has led to a substantial demand for adequate healthcare resources and placed a great burden on the worldwide economy. Consequently, there is an increased emphasis by healthcare professionals and commissioners on advancing early disease treatments and augmenting the efficiency of the available treatment interventions.

The use of titanium, stainless steel, and cobalt alloys and other inert metals has been traditionally evident in the fabrication of orthopaedic and cardiovascular implants. This specific use can be attributed to the robust mechanical properties with respect to local biological tissues as well as the corrosion resistant characteristics of these elements (Park and Bronzino 2002). The metallic implants (made of bioinert materials that has

minimal interaction with its surrounding tissue) currently in production and use are structured to provide a permanent replacement of the original tissues in the body. However, the complete tissue replacement concept fails to account for treatment conditions, which essentially warrant a temporary supporting function, i.e., until the damaged tissue is completely healed. Due to this void in design, the use of permanent inert materials in treatments mandating temporary support function, has, in fact, led to several complications such as bone weakening, time progressive stress-shielding, diagnostic image distortions, and secondary surgery for implant removal (Chen and Thouas 2015).

As alternatives, the Food and Drug Administration (FDA) has approved the use of biodegradable synthetic polymer compounds (like, poly(lactic acid-co-glycolic acid) (PLGA), poly(l-lactic acid) (PLLA), and poly(glycolic acid) (PGA)) for use in specific clinical applications (Ramakrishna, Mayer et al. 2001). In addition to functional restoration, the biodegradable implants allow for complete tissue healing without foreign implant materials remaining in situ. The conventional implants remain permanently in place to restore the tissue functionality but fail to restore tissue back to its original state. It has been evidenced in prior research that in orthopaedics, the procedures involving the removal of permanent implants constitute for 30% of all elective procedures (Acklin, Michelitsch et al. 2016). Specifically, in Germany, 180,000 total additional surgeries were performed in the year 2010 for permanent fixture removals. This statistic propelled this procedure globally, to fourth place for most commonly performed orthopaedic surgical procedure after surgical fracture fixation, arthroscopies, and intervertebral disc interventions (Reith, Schmitz-Greven et

al. 2015). Hence, the utilization of degradable implants could result in the elimination of additional procedures for permanent fixture removal, thereby projecting dual benefits to the patient as well as the healthcare system, in terms of reduced surgery time and lower healthcare costs, respectively. However, the practical use of biodegradable polymer implants has seen a decrease owing to (i) the tissue acidification that causes tissue inflammation in areas adjacent to degrading synthetic polymers and (ii) weak mechanical structure that leads to early implant fracture (Bostman and Pihlajamaki 2000).

There are few reported applications of natural polymers (chitosan, collagen, and keratin) as biodegradable implant materials. This limited use is attributed to the inadequacy of their mechanical properties which are too weak to withstand the loading during the degradation process (Venkatraman, Boey et al. 2008).

Several scholars (Di Mario, Griffiths et al. 2004, Staiger, Pietak et al. 2006, Witte 2010) have highlighted the impending revolution in orthopaedic treatment of broken bones with the recent advances in biodegradable metallic material technology. In comparison to their polymer counterparts, biodegradable metallic implants are found to be significantly stronger and the degraded metal particles present the characteristics of being fully dissolvable in body fluids. In fact, the excess amount of degraded metal particles can be dissolved by phagocytic cells (including macrophages), and safely excreted in the urine (Saris, Mervaala et al. 2000, Staiger, Pietak et al. 2006, Song 2007). . In physiological settings, a series of anodic and cathodic reactions result in the degradation of the biodegradable metal (‘corrosion’ and ‘degradation’ convey the same meaning in this work). Metal degradation, typically, is known to occur by the

conversion of metallic material into a more stable ion. Figure 1.1 depicts the process of metal oxidization resulting from body fluid contact and also the process of cathodic reactions consuming the generated electrons. In addition to hydroxide, hydrogen gas is released with these reactions forming a protective metal oxide layer on the surface. For magnesium alloys, a high chloride ion concentration in the body fluid results in the weakening of this protective oxide layer which in turn accelerates the degradation process. Subsequently, with the progression of this process, the metal oxide layer is covered with calcium phosphate deposits due to the local alkalization, as well as the presence of saturated calcium and phosphate in the body fluid. Eventually, this leads to the adherence of cells on the surface to form tissues.

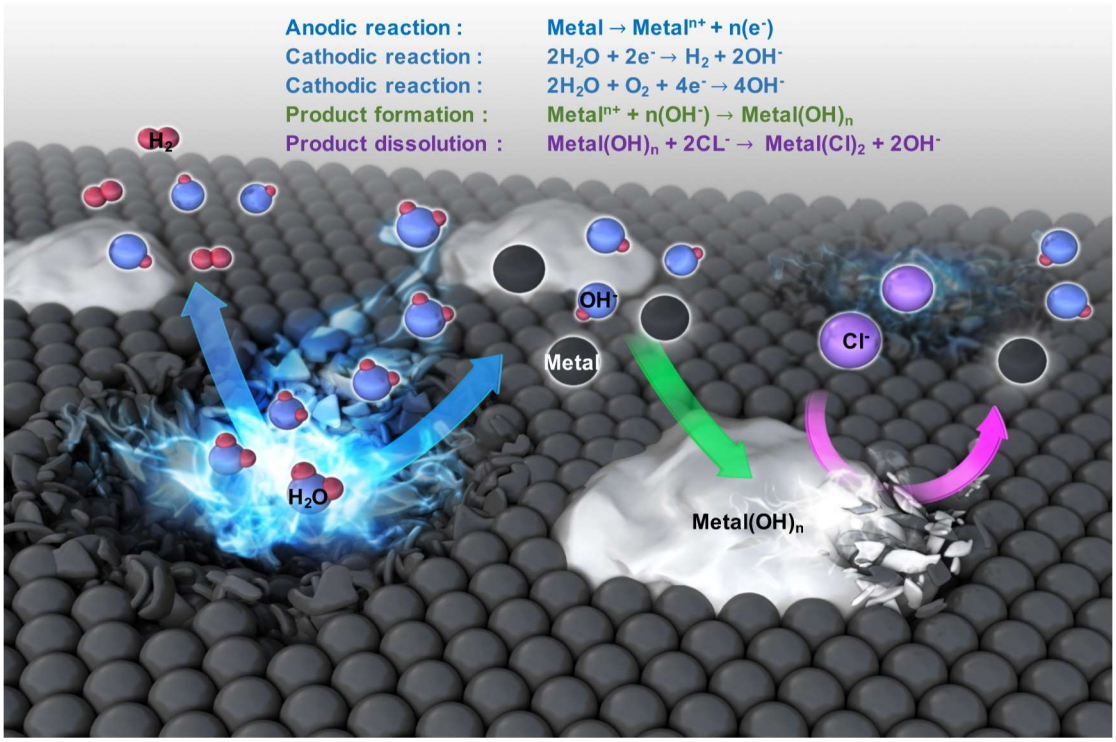


Figure 1.1. The process of biodegradation for metals. Figure adapted from (Han, Loffredo et al. 2018)

In humans, the first recorded application of a biodegradable implant material has been traced to over a century ago. In 1878, the first successful pure magnesium wire ligature usage to stop bleeding was reported by Edward C. Huse (Huse 1878). The procedure was done without the knowledge of the biodegradable property of magnesium at the time. This was followed by a series of clinical trials that utilized the Mg-based implants, but they demonstrated a fast degradability and premature failures due to the absence of sufficient metallurgical technology (Figure 1.2). However, recent advancement in metal purification technology and several alloying techniques have allowed the development of significantly stronger and slower degrading material, which realigned the focus on application of biodegradable metals as orthopaedic implant material. After almost two decades of extensive laboratory and early translational research (Zberg, Uggowitzer et al. 2009, Cha, Han et al. 2013, Waizy, Diekmann et al. 2014, Zhang, Xu et al. 2016), a significant clinical potential is now apparent within these new metals to impact a paradigm shift in the treatment of musculoskeletal conditions (Windhagen, Radtke et al. 2013, Lee, Han et al. 2016).

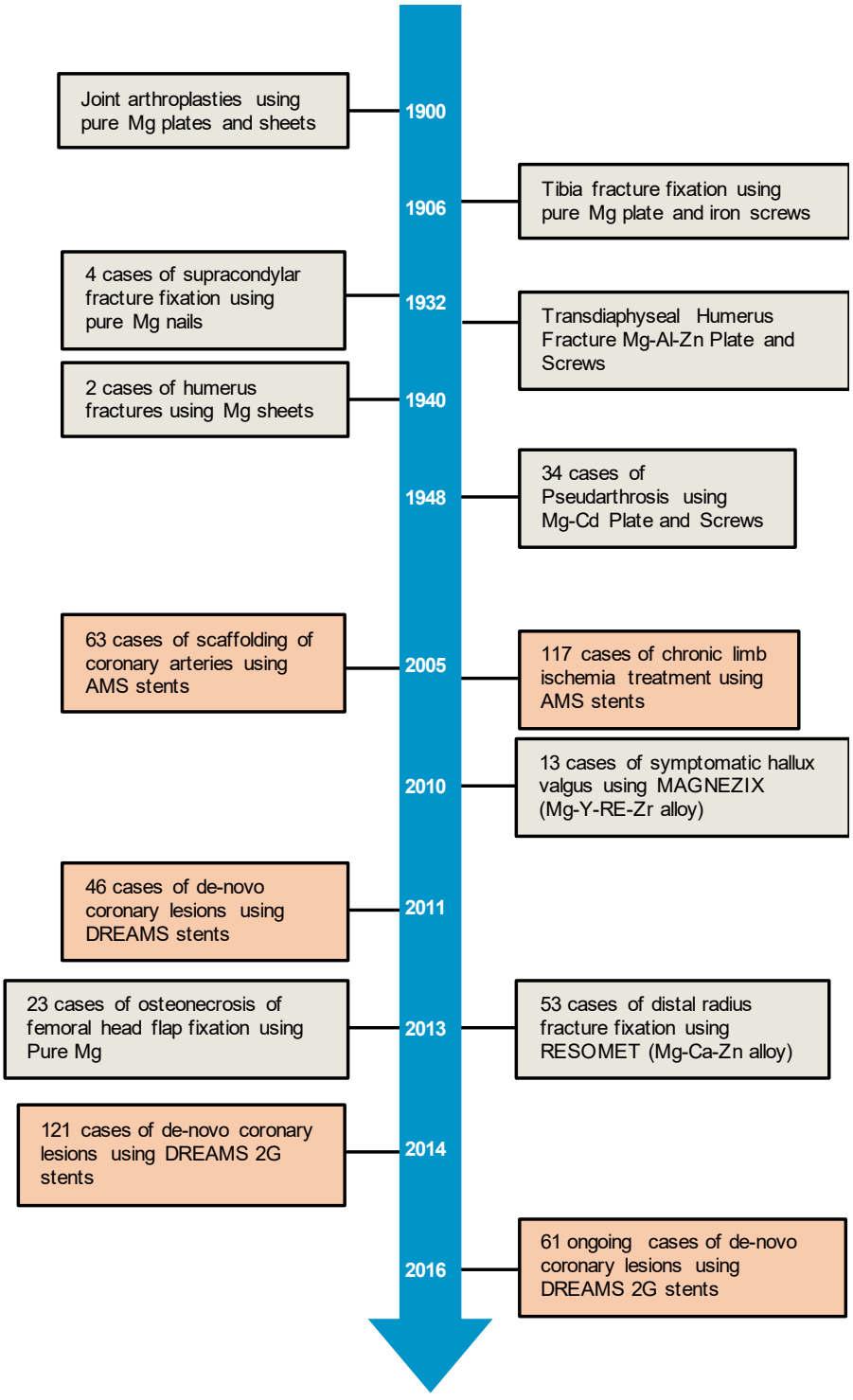


Figure 1.2. Timeline of representative clinical trials of biodegradable metals in cardiology (red) and orthopaedics (grey). Figure adapted from (Han, Loffredo et al. 2018)

Recently, Cha *et al* (2013) reported the development of metallic biodegradable Mg-Ca-Zn alloy system for orthopaedic applications with the addition of intrinsically biocompatible elements. Studies have shown that this alloy is well-tolerated in pre-clinical and clinical settings and provides adequate mechanical support during the initial phase of healing, before it is replaced by new bone. However, the lack of fundamental understanding in bone formation and remodelling mechanism in the presence of degrading particles is limiting the clinical application of the developed material.

1.2 Objectives

The objective of this research is to explore the biological response to a novel biodegradable Mg5wt%Ca-1wt%Zn (Mg5Ca1Zn) alloy developed for orthopaedic repair, to study the bone remodelling process and assess the potential of the new implant. In order to achieve this, the experimental work initially aims to identify the mechanisms underpinning the interaction of the alloy system with osteoclast (OC) and osteoblast (OB) cells through conventional *in vitro* analysis. Following which, the study explores the active Mg alloy's biodegradation impact on the 3D cultured OB cells wherein the experiment is performed within a perfusion bioreactor system to mimic an environment similar to the native bone tissue and explicate the benefit of simulated flow-induced loading in this system. Also, to further understand the bone healing process in and around a degrading Mg alloy, a comparison between an *ex vivo*

quantitative analysis of blood vessel growth and *in vivo* assessment of angiogenesis and coupled osteogenesis at the Mg alloy implanted site was performed.

In addition, this work explores a potential substitute for the use of mammalian systems offering a delicate and expedited evaluation of the *in vivo* toxicity of newly developed biodegradable metallic materials.

Chapter 2

Literature Review

2.1 Orthopaedic application of biodegradable metals

According to Becker (1999), the use of metallic implants has been evidenced over several millennia through the replacement materials found in the skull and teeth of ancient human skeletons. Several scholars (Geetha, Singh et al. 2009, Chen and Thouas 2015) have inferred the concept of bone replacement as a main factor of the orthopaedic implant development. In addition, for nearly a century, conventional bioinert materials like stainless steel, cobalt alloy, and titanium have been extensively used without substantial changes, for trauma treatment in the human body. These foreign materials, irrespective of their clinically proven biocompatibilities, continue to indefinitely remain in the body, thereby, projecting potential complications upon reaching their expected working life. Researchers have been propelled by these limitations towards conducting an investigation of biodegradable materials with characteristics pertaining to sufficient initial mechanical integrity and over time degradation to ensure a new tissue formation latticework prior to the complete natural healthy tissue replacement (Zheng, Gu et al. 2014). In paediatric applications, such implant materials offer

significant benefits, as even after implantation the patient's tissue often continues to grow.

It has been observed that biodegradable metal based (mostly magnesium) orthopaedic implants present elastic modulus similar to bone and safely biodegrade when implanted into physiological surroundings through reaction with chloride ions. According to Zhao, Witte et al. (2017), now, biodegradable metallic alloys can be designed through incorporation of advanced metallurgy techniques to gradually transfer load from the implant to the tissue and match the process of bone healing and remodelling.

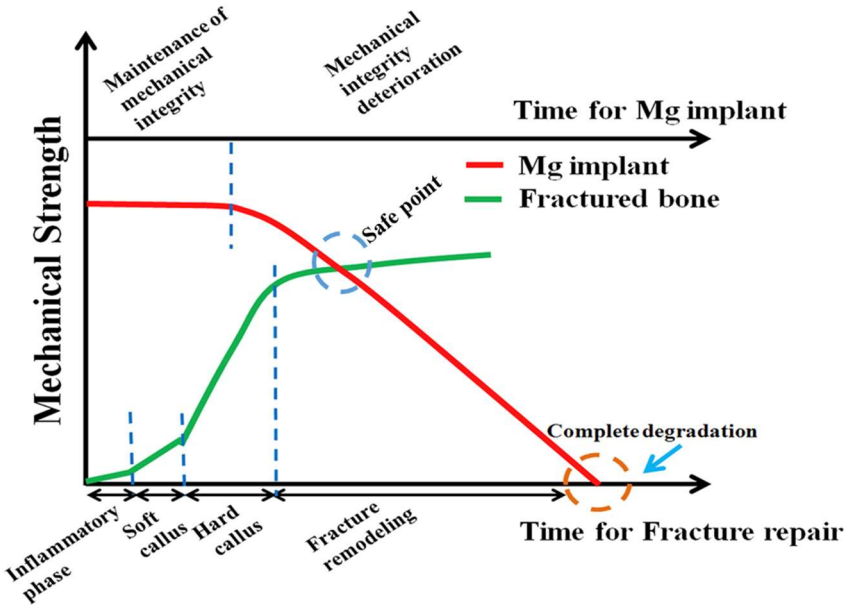


Figure 2.1. Optimal degradation behaviour of Mg-based implant in bone fracture healing. Figure adapted from (Zhao, Witte et al. 2017).

Typically, the orthopaedic implant is required at the early healing stage of a bone fracture to maintain the structural integrity. Systemically designed biodegradable implants allow for sufficient load support at initial stages of repair while slowly degrading at an optimized rate allowing for the complete healing of fractured bone

(Chen, Xu et al. 2014). Recently, Zhang et al. (2016) reported that magnesium promotes calcitonin gene-related polypeptide-α mediated osteogenic differentiation, thereby illustrating a potential mechanism and highlighting the therapeutic potential in orthopaedics of biodegradable metals (Zhang, Xu et al. 2016).

2.2 The bone fracture healing process

As mentioned before, the initial healing of fractured bone requires the biodegradable implant to maintain structural integrity. Optimized alloy systems provide sufficient load support at this early stage while degrading at an optimal rate for complete bone healing and it is crucial to first understand the bone fracture healing process in human body to systemically design an alloy system.

2.2.1 Inflammation reaction phase

Immediately following a fracture, cells from the blood and bone marrow start to accumulate, generating a hematoma at the injury site. The injury starts the inflammatory response that is required for the bone healing process and this response leads to coagulation of the hematoma at the fractured bones to form a template for the formation of callus (Gerstenfeld, Cullinane et al. 2003). In general, prolonged release of inflammatory cytokines cause adverse effect on bone but the secretion of regulated proinflammatory molecules after the acute injury is believed to be essential for bone

healing (Gerstenfeld, Cullinane et al. 2003). Such acute inflammatory response reaches its peak during the first 24 hours and is usually completed after one week (Cho, Gerstenfeld et al. 2002).

Initially, factors that are involved with the recruitment of inflammatory cells and promotion of angiogenesis such as tumor necrosis factor-α (TNF-α), interleukin-1 (IL-1), interleukin-6 (IL-6), interleukin-11 (IL-11) and interleukin-18 (IL-18) are secreted by the proinflammatory response (Gerstenfeld, Cullinane et al. 2003). TNF-α facilitate the osteogenic differentiation of mesenchymal stem cell into chondrocytes and osteoblasts through activation of tumor necrosis factor receptor 1 (TNFR1) and tumor necrosis factor receptor 2 (TNFR2) (Kon, Cho et al. 2001, Balga, Wetterwald et al. 2006). The recruitment of MSC is believed to be mediated by the stromal cell-derived factor 1 (SDF-1) and its G-protein-coupled receptor CXCR4 (Ma, Ge et al. 2005, Granero-Moltó, Weis et al. 2009).

For bone healing, IL-1 and IL-6 are believed to play the most crucial role. IL-1 is produced by the macrophages during acute inflammation phase and promotes IL-6 production in osteoblasts, formation of cartilaginous callus, and angiogenesis by activating IL1RI or IL1RII (Kon, Cho et al. 2001, Lee and Lorenzo 2006). IL-6 facilitates osteoblast and osteoclast differentiation, production of vascular endothelial growth factor (VEGF) and angiogenesis (Yang, Ricciardi et al. 2007).

Eventually, fibroblasts and MSC migrate to fracture site to form a fibrin-rich granulation tissue (Marsell and Einhorn 2011).

2.2.2 Renewal phase

In the granulation tissue, endochondral ossification starts to occur external to periosteal sites and in between the fracture site (Marsell and Einhorn 2011). The soft callus formed by the cartilaginous tissue provide the fracture with mechanical stability. The intramembranous ossification occurs simultaneously at the distal and proximal end of the fracture to generate a hard callus. The final bridging of such hard callus provides the fractured bone a rigidity to support the weight (Gerstenfeld, Alkhiary et al. 2006). The generation of these callus tissues is dependent on the recruitment of MSCs from the surrounding soft tissues, cortex, periosteum, and bone marrow as well the systemic mobilization of stem cells into the peripheral blood from remote.

During this process, the transforming growth factor-beta2 (TGF-β2), the transforming growth factor-beta3 (TGF-β3), and Growth/differentiation factor 5 (GDF-5) are known to facilitate the chondrogenesis and endochondral ossification, while BMP-5 and BMP-6 is believed to promote proliferation of cells at periosteal sites during intramembranous ossification (Cho, Gerstenfeld et al. 2002, Marsell and Einhorn 2009).

The primary soft cartilaginous callus must be resorbed and get replaced by the hard-bony callus for the progression of bone regeneration. The proliferation of fracture callus chondrocyte increases its volume and causes calcification of the extracellular matrix. The resorption of such calcified and mineralized cartilage is then initiated by the macrophage colonystimulating factor (M-CSF), osteoprotegerin (OPG), receptor

activator of nuclear factor kappa B ligand (RANKL), and TNF-α (Barnes, Kostenuik et al. 1999, Gerstenfeld, Cullinane et al. 2003). M-CSF, OPG and RANKL are believed to support the recruitment of bone cells and osteoclasts to create woven bone during this process (Marsell and Einhorn 2011). Particularly, TNF-α plays an important role of initiating the chondrocyte apoptosis and further promoting the MSC recruitment for osteogenic purposes (Gerstenfeld, Cullinane et al. 2003).

The mitochondria play a big role in calcification process by accumulating the granules containing calcium formed in hypoxic fracture condition. Following the elaboration into the fractured callus chondrocytes cytoplasm, the granules of calcium precipitate with phosphate to create mineral deposits for formation of apatite crystals (Ketenjian and Arsenis 1975). With the progression of hard callus formation and woven bone replacement of calcified cartilage, the callus gains mechanical strength and rigidity for load bearing purposes (Gerstenfeld, Alkhiary et al. 2006).

2.2.3 Remodelling phase

The formation of hard callus provides the strength and mechanical stability for the fracture, but it does not restore the biomechanical functionalities of the natural bone. The second resorption phase is initiated to restore such functionalities and change hard callus into a lamellar structure with central medullary cavity (Gerstenfeld, Cullinane et al. 2003). The lamella bone structure gradually replaces the external callus and the remodelling of internal callus recreates medullar cavity characteristic (Marsell and Einhorn 2011). This phase shows high expression level of IL-1 and

TNF-α. BMP2 also shows relatively high expression but TGF-β2 and TGF-β3 shows very little expression during this phase (Marsell and Einhorn 2009). The remodelling process of bone is orchestrated by a harmonious resorption of hard callus and deposition of lamellar bone. The complete remodelling of fractured bone to obtain original bone structure could take years to finish even though the process is started at 3-4 weeks after the fracture (Wendeberg 1961). The healing process is reported to be faster in younger patients and the loading on the healing bone seem to facilitate the bone formation process. A sufficient blood supply at the fracture site and mechanical stability is a key factors of successful bone remodelling (Carano and Filvaroff 2003).

2.3 Translational research on biodegradable metals

Largely, the developmental research on biodegradable metals for orthopaedic application has focused on magnesium and its alloys which can be attributed to their sufficient mechanical properties and outstanding biocompatibility. Saris, Mervaala et al. (2000) explicate that Mg is fourth most abundant mineral in the body which is mostly stored in bones and teeth. A positive impact on the surrounding hard tissues has been demonstrated by the rapid ionization process from active magnesium implant degradation, and the kidneys have shown to secrete excess amounts of Mg (Vormann 2003). Furthermore, Mg-based alloys (41-45GPa) have an elastic modulus that shows a distinct similarity with human bones (3-20 GPa). This characteristic allows for a natural load transfer to the surrounding bone tissues to stimulate the remodelling

process. According to Witte (2015), the initial attempts to use Mg as an orthopaedic implant device date back to early 1900s. However, the extensive use was subsequently limited due to the excessive corrosion of magnesium in the human body attributed to the lack of magnesium refinement technology. The impurities inside the Mg implant at the time resulted in large corrosion potential differences to cause pitting and rapid galvanic corrosion of the material. Galvanic corrosion occurs when two or more metals with different electrode potentials come into contact. The difference in the electropotential accelerates the attack on the metal that acts as anode and dissolves into the electrolyte. After nearly a century later in 1999, research was initiated by scientists at the University of Hannover in Germany with a focus on exploiting the magnesium alloy's bioactive properties and proposed a novel concept of biodegradable metallic materials. In 2003, the development of a magnesium alloy stent was explored by a German implant manufacturing company, and subsequently Korea, Japan, China and United States initiated intensive research programs into biodegradable metallic materials in 2005. After a decade of developmental research, the extensive findings have allowed for the projection of a road map for the next generation of magnesium implants with incorporation of different alloying elements (Figure 2.1). The developmental process of these alloy systems has been extensively studied by several scholars (Chen, Xu et al. 2014, Zheng, Gu et al. 2014, Zhao, Witte et al. 2017) and this literature review chapter discusses and provides an overview of the Mg alloy systems that are nearing or currently in the clinical stage. It will include the general degradation behaviour of system, *in vivo* performances, translation efforts, and their clinical benefits.



Figure 2.2. Current state-of-the-art applications of biodegradable metals. (a) Clip applier with operative Mg clip, (b) MgF2 coated Mg-2wt%Nd alloy nasal stent, (c) Loaded Mg microclip in microlaryngeal forcep, (d) Mg stent for neurological application, (e) Mg-based intramedullary nail. Devices at clinical stages – (f) Resomet orthopaedic devices, (g) DREAMS 2nd generation stent, (h) Magnezix screw and pin, (i) Iron-based suture anchor, (j) Velox CD vascular closure device, (k) Pure Mg Screws. Figure adapted from (Han, Loffredo et al. 2018)

2.3.1 Pure Mg

For the magnesium based orthopaedic devices, pure magnesium is the simplest form of a material system. In the context of a heavy load-bearing implant, pure magnesium displays relatively low mechanical strength for its effective utilization and application. The yield tensile strength of pure Mg is reported to be 21 MPa, 95-105 MPa and 115-140 MPa for as-cast, as-extruded and as-rolled, respectively (Zheng, Gu et al. 2014). However, the toxicity concern of other alloying elements is eliminated with its usage. In addition, the comparatively low degradability percentage in the exceptionally high-purity magnesium (>99.99%) offers it as the most ideal alternative for low load-bearing orthopaedic applications. The impurity volume control is, in fact, one of the greatest challenges in working with pure Mg. Specifically, trace amount of impurities in pure Mg can initiate local degradation processes due to corrosion differences, which can further lead to pitting corrosion processes and a rapid total erosion as shown in Figure 2.2 (Han, Lee et al. 2012). Studies have reported 3 to 60 times faster degradation rates for pure Mg when the concentration of iron impurity increased to 26 to 48 ppm (Qiao, Shi et al. 2012). Such accelerated corrosion rates lead to the formation of gas cavities, as significant amount of hydrogen gas is generated at the early implantation stage that surpasses local saturation hydrogen levels in blood and tissue. Ultimately, creating the possibility of mechanical disturbances at the implantation site due to the excessive pressure resulting from callus formation attributed to excessive hydrogen gas within these cavities (Kraus, Fischerauer et al. 2012). This has been evidenced as a factor in decreased survival rates in various studies, which demonstrate that in tested rats these

gas cavities resulted in a disturbed balance of blood cell parameters as well as causing massive subcutaneous emphysema (Noviana, Paramitha et al. 2016). Correspondingly, the experimental research involving pure Mg implant development has concentrated on advanced purification techniques for reduced degradation rates and the current preclinical application ranges from bone screws, plate and screw systems, and interference screws (Chaya, Yoshizawa et al. 2015, Han, Cheng et al. 2015, Cheng, Han et al. 2016, Wang, Xu et al. 2016, Zhao, Huang et al. 2016, Wang, Xu et al. 2017). As such, the latest research has shown a crucial emphasis on the development of interference screws for Anterior Cruciate Ligament (ACL) reconstruction, in addition to the bone screw system (detailed in the subsequent clinical trial section). In ACL reconstruction rabbit models, the recent studies demonstrated an accumulation of bone morphogenetic protein-2 and vascular endothelial growth factor due to the release of Mg ions from high-purity Mg interference screws that, in turn, lead to early phase tendon-bone healing process (Cheng, Han et al. 2016). Moreover, at the remodelling phase, the expression of matrix metalloproteinase-13 by Mg interference screws is reduced, consequently leading to an inhibitory effect on tendon graft degradation, thereby providing a favourable preclinical outcome with attachment of an increased quantity of collagen fibres in the tendon graft to the bone (Cheng, Han et al. 2016). Another recent study by Wang, Xu et al. (2017) emphasised the excellent bone formation associated with Mg screws in a rabbit model with ACL reconstruction. This comparative study of high-purity Mg and Ti screws on tendon graft healing demonstrated improved early healing, with the prevention of bone tunnel widening, and thus highlight its potential clinical applications.

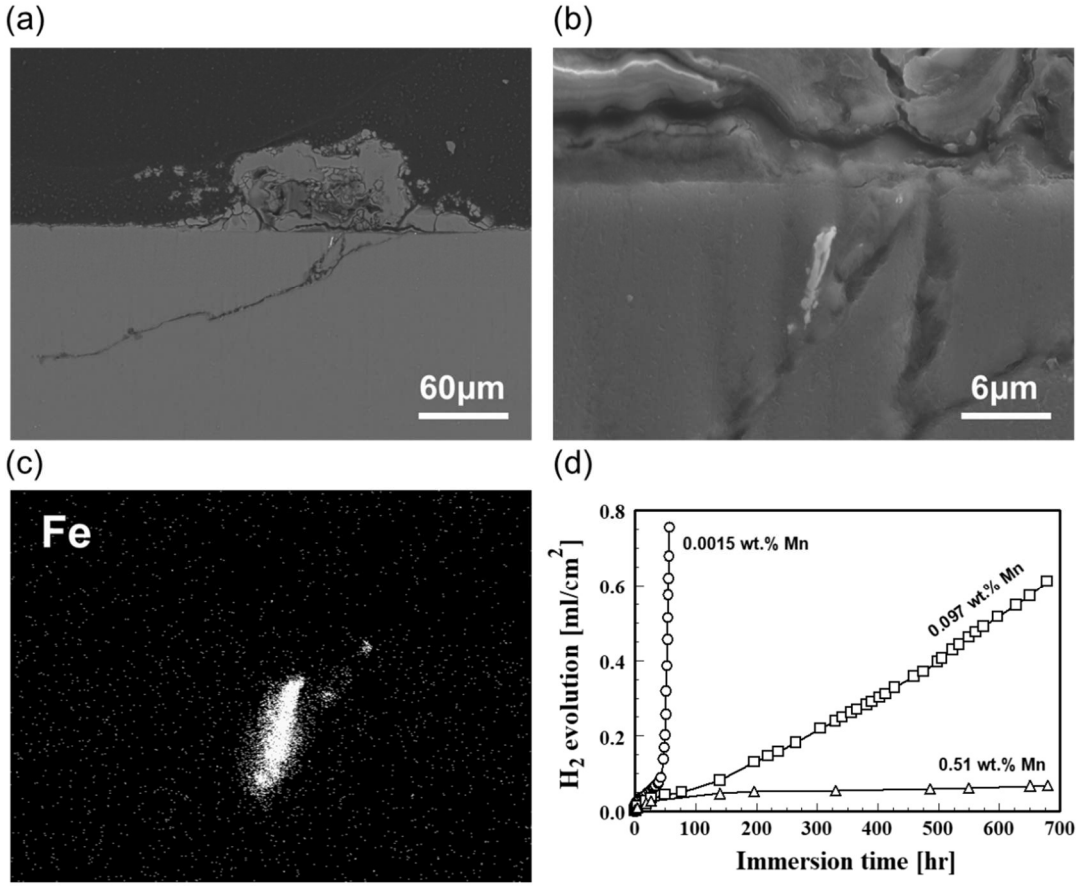


Figure 2.3. (a) Pitting corrosion of pure Mg observed with SEM. (b) magnified view of local corrosion initiation point. (c) WDS element mapping of the corresponding region showing Fe impurity in the area of (b). (d) corrosion rate of pure Mg depending on the impurity of Mn. Image adapted from (Han, Lee et al. 2012).

2.3.2 Mg-Al alloys

Aluminium, with a high maximum solubility of 12.7 wt% in Mg, has been one of the most extensively studied alloying elements for Mg based alloy system in the initial developmental stage of biodegradable orthopaedic implants, due to excellent

mechanical properties (YS of 290 MPa, UTS of 417 MPa and elongation of 8.45% after extrusion), castability and corrosion resistance (Chen, Xu et al. 2014). Aluminium containing Mg alloy systems like AM alloys and AZ alloys have been developed for industrial applications in the past and were readily available at the early material development stage for further optimization as implantable devices. The addition of increased Al concentration up to 6 wt.% in Mg based alloys typically results in increased ultimate tensile strength (UTS) and elongation. The formation of an aluminium oxide film from increased Al content also results in a decreased degradation rate (Zheng, Gu et al. 2014). Despite the established neurotoxicant nature of aluminium, in particular reference to Alzheimer's disease and dementia, (El-Rahman 2003), scholars argue that released quantity of aluminium is reasonably below the recommended intake limit for Mg alloy system with less than 5 wt.% aluminium and moreover, no direct detrimental effects have been evidenced in long term *in vivo* studies (Angrisani, Reifenrath et al. 2016). Using a rabbit tibia model, Angrisani et al. (2016) have shown post-implantation degradation of the LAE442 alloy system for almost three and half years, validating the safety of aluminium containing Mg-based alloy. As shown in Figure 2.3, the LAE442 alloy system showed a substantially slower degradation rate when compared to pure Mg and despite the lack of information regarding the exact neurological state of the animals, no significant accumulation of aluminium were reported in major organs such as brain, liver, spleen and kidney after three and half years of degradation inside the tibia (Angrisani, Reifenrath et al. 2016). However, the minimal aluminium (4 wt.%) content in the LAE442 alloy system could have caused such a non-toxicity result. Several scholars have discussed the latest Mg-

Al systems applications to range from the development of intramedullary nail systems to craniofacial screws (Henderson, Verdelis et al. 2014, Rossig, Angrisani et al. 2015, Sun, Zhang et al. 2016).

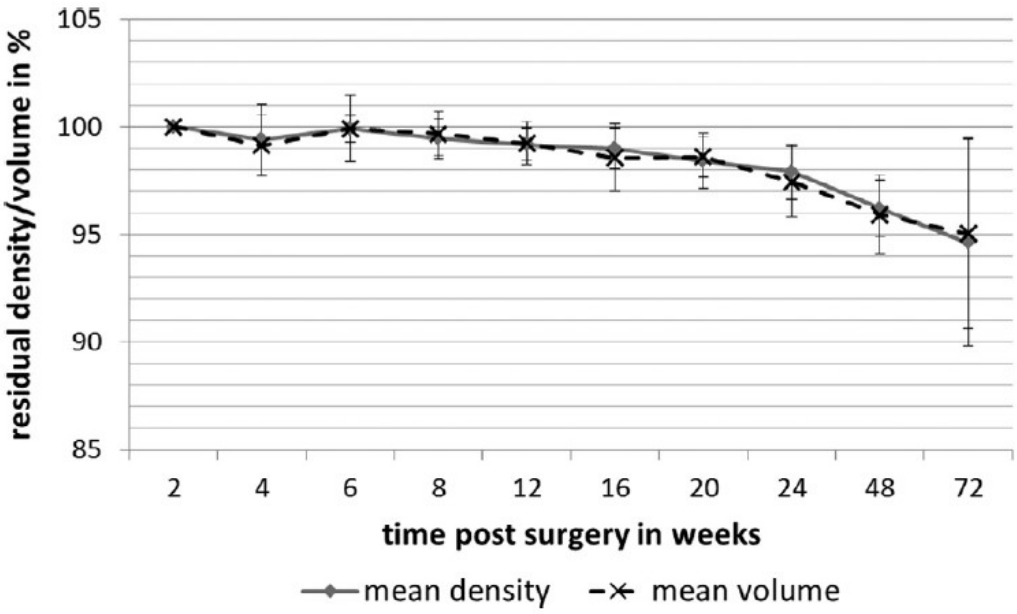


Figure 2.4. Slow and gradual degradation rate of LAE442 sample observed by loss of residual density and volume over 72 weeks in rabbit tibia (Angrisani, Reifenrath et al. 2016).

2.3.3 Mg-Rare Earth alloys

The rare earth elements (REEs) used for alloying of Mg-based system are generally divided into two categories depending on their solubility in magnesium. According to Zheng, Gu et al. (2014), the high solid-solubility group includes Yttrium (Y), Gadolinium (Gd), Terbium (Tb), Dysprosium (Dy), Holmium (Ho), Erbium (Er),

Thulium (Tm), Ytterbium (Yb), Lutetium (Lu), and the limited solid-solubility group includes Neodymium (Nd), Lanthanum (La), Cerium (Ce), Praseodymium (Pr), Samarium (Sm), and Europium (Eu). Initially, the addition of REEs was aimed at ensuring a significant increase in the creep and corrosion resistance of magnesium at room temperature and above (Hort, Huang et al. 2010, Mert, Blawert et al. 2012). However, the development of Mg-REE alloy systems has witnessed a robust progression due to several experimental studies concentrated on the exploration of different element compositions and their effect on mechanical and corrosion characteristics (Windhagen, Radtke et al. 2013, Guan, Xiong et al. 2014, Waizy, Diekmann et al. 2014, Biber, Pauser et al. 2016, Diekmann, Bauer et al. 2016, Marukawa, Tamai et al. 2016, Plaass, Ettinger et al. 2016, Schaller, Saulacic et al. 2016, Biber, Pauser et al. 2017, Schaller, Saulacic et al. 2017). In Mg-REE alloys, the most advanced system is the MgYREZr alloy. MgYREZr system is currently in clinical use and presents a similarity with the WE43 alloy system from a material perspective. It is constituted of >90 wt.% of magnesium; an average grain size of <5 μm; 275 MPa tensile strength; and 10% elongation. The Conformité Européene (CE) approval for human application was given to the material in 2013 and since then this alloy system has to date, been used in development of a wide range of implants.

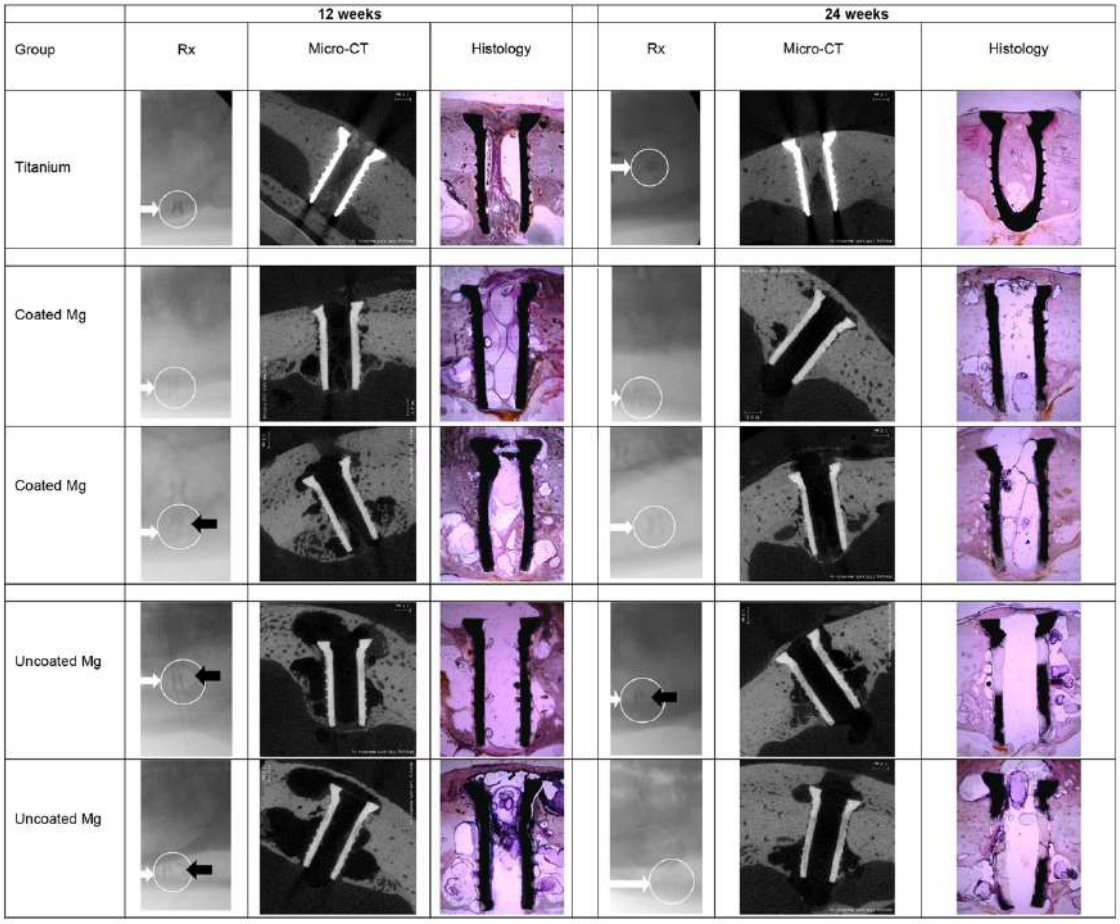


Figure 2.5. Micro-CT and histological analysis of WE43 alloy screw implanted on mandible of miniature pigs for 12 and 24 weeks. Mg implants with plasmaelectrolytic coating show absence of gas cavity. (Schaller, Saulacic et al. 2016)

In addition, *in vivo* models are being extensively used to test various surface treatment techniques with the aim of further optimizing the degradation properties. For example, Marukawa, Tamai et al. (2016) adopted a canine fracture model to draw direct comparisons between anodized WE43 screws and PLLA screws. It was found that all PLLA screws were broken after 4 weeks, which evidenced the superior mechanical strength of WE43 at load-bearing sites, and a reduced hydrogen gas inflammatory

response was additionally seen in anodized treatment of WE43. Furthermore, Diekmann, Bauer et al. (2016) in a recent pilot study tested the MG-REE alloys for application in ACL reconstruction, wherein, the results were found to be similar to a titanium control, thereby indicating their potential applicability. In addition, Schaller, Saulacic et al. (2017) have tested human standard-sized rivet screw implants made out of WE43 alloy in a miniature pig to demonstrate the effectiveness of plasmaelectrolytic coating on corrosion rate and superior mechanical properties of Mg-REE alloys. Screws coated with plasmaelectrolytic coating did not show the gas cavity around the implantation site and showed similar healing tendency to the conventional titanium implant.

2.3.4 Mg-Zn Alloys

Zinc is an essential element found in the cells all over the human body that plays a significant role in carbohydrate catabolism, the immune system, as well as promoting cellular interactions. Zinc has limited 6.2 wt.% solubility in magnesium based alloy system and Mg-Zn alloys demonstrate a maximum UTS of 216.8 MPa and 15.8% elongation at 4 wt.% of Zn (Zhang, Wang et al. 2011). Scholars have extensively studied the addition of various elements including Ca, Zr, Sr, Y, Mn, and Si to Mg-Zn alloy system to yield ZK alloys and ZX alloys systems which in comparison to the clinically approved WE alloys demonstrate superior mechanical properties (Huan, Leeflang et al. 2010). In general, the degradation rate of Mg-REE alloys is comparatively lower than Mg-Zn alloys but the systemically designed Mg-Zn alloy

system have shown a similar degradation pattern *in vivo* after 24 months in recent long-term animal studies using Sprague-Dawley rats. In addition, Wang, Ni et al. (2017) reported the application of the Mg-6Zn alloy system as a pin stapler to treat intestinal anastomosis. The study conducted a direct comparison, wherein, a titanium alloy underperformed in stimulation of the extra cellular matrix accumulation against Mg-6Zn alloy for improved intestinal anastomosis healing.

The involvement of metallic glass materials highlights an additional interesting aspect of Zn-containing Mg systems. A particular atomic arrangement is seen in conventional metallic materials which constitute specific crystalline structures. However, these experiments have been shown to yield non-crystalline amorphous metals with glass-like structures by utilizing a secondary process such as ion irradiation, extremely rapid cooling, or physical vapour deposition. In this secondary process, the metallic glass solidifies prior to crystallization, and usage of molds allows casting of such metallic glass into shaped functional bulk material. Typically, metallic glasses demonstrate high strength and low elasticity due to their unique irregular atomic arrangement and excellent corrosion resistance characteristics caused by the absence of crystal grain boundaries. Zberg et al. (2009) developed a biodegradable $Mg_{60+x}Zn_{35-x}Ca_5$ ($0 \leq x \leq 7$) metallic glass material with a characteristic of exceptionally high strength of a maximum 854 MPa in compression and 894 MPa in tension. In fact, this strength was 2–3 times higher than that of common crystalline Mg alloy systems. The absence of crystalline structure led to a significantly lower corrosion rate with negligible hydrogen evolution as shown in Figure 2.5, but it also led to critically low elongation of less than 2% (Zberg, Uggowitzer et al. 2009). In addition, production of lower hydrogen gas

yielded increased favourable clinical outcomes which was further augmented due to protective ZnO and $ZnCO_3$ film layer formation.

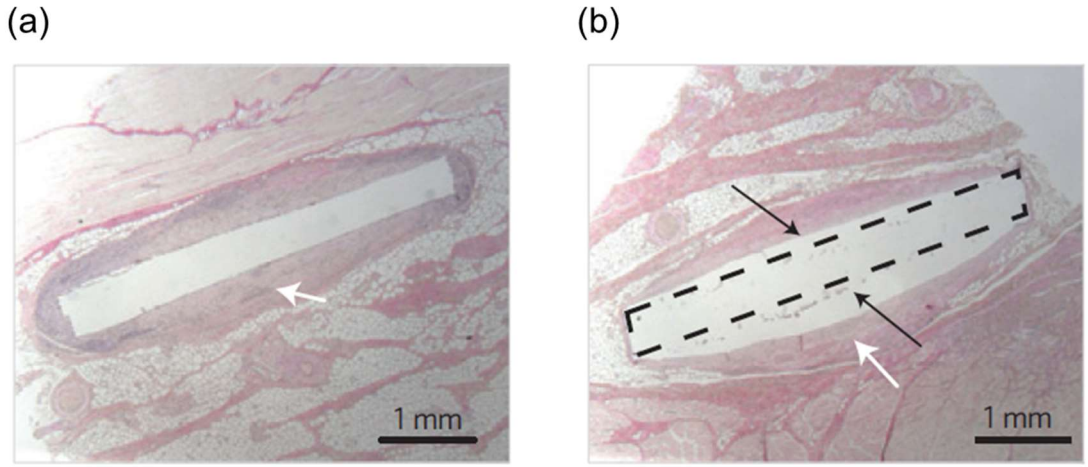


Figure 2.6. Comparison of hydrogen gas cavity formation for (a) Mg metallic glass material and (b) crystalline Mg alloy implanted on subcutaneous tissue of pigs. (Zberg, Uggowitzer et al. 2009)

Typically, galvanic corrosion is caused by the formation of secondary or tertiary phase formation from alloying of different elements in pure Mg. As such, in physiological systems, the mechanical integrity of biodegradable implant devices could deteriorate further due to the rapid and non-uniform progression of such corrosion. Thus, the usage of the metallic glass system provides a feasible alternative solution without clinically observable hydrogen evolution. For possible clinical applications however, it is imperative to overcome the brittleness of the metallic glass, which under severe loading would result in shattering of the implanted device.

2.3.5 Mg-Ca Alloys

Calcium, which is stored in high quantities in bone and teeth, plays a significant role in cell signalling and the maintenance of structure and function of skeletal tissues. Correspondingly, a positive bone healing effect has been demonstrated following the release of Ca ions into the local cellular environments. Concurrently, several studies have focused on developing clinically relevant Mg-Ca alloy systems. In general, the addition of calcium increases the mechanical property of the Mg-Ca alloy system. However, at 1.34 wt.% the solubility of Ca in Mg is very limited and saturation of calcium yields a secondary Mg_2Ca phase that can potentially result in an accelerated degradation rate as shown in Figure 2.6 (Li, Gu et al. 2008). In 2010, a team of Korean researchers reported the development of a clinically applicable Mg-Ca alloy system with the addition of 5 wt.% Ca for the first time (Cha, Han et al. 2013). The accelerated degradation rate from the addition of calcium was controlled by coordinating the corrosion potentials of two constituent phases Mg and Mg_2Ca which was done through selectively doping Zn into Mg_2Ca. The connectivity of the Mg_2Ca phases was disrupted by an optimized mechanical extrusion process which was done in order to avoid continuous corrosion and prevent development of a galvanic circuit, which causes severe corrosion of the Mg-Ca alloy.

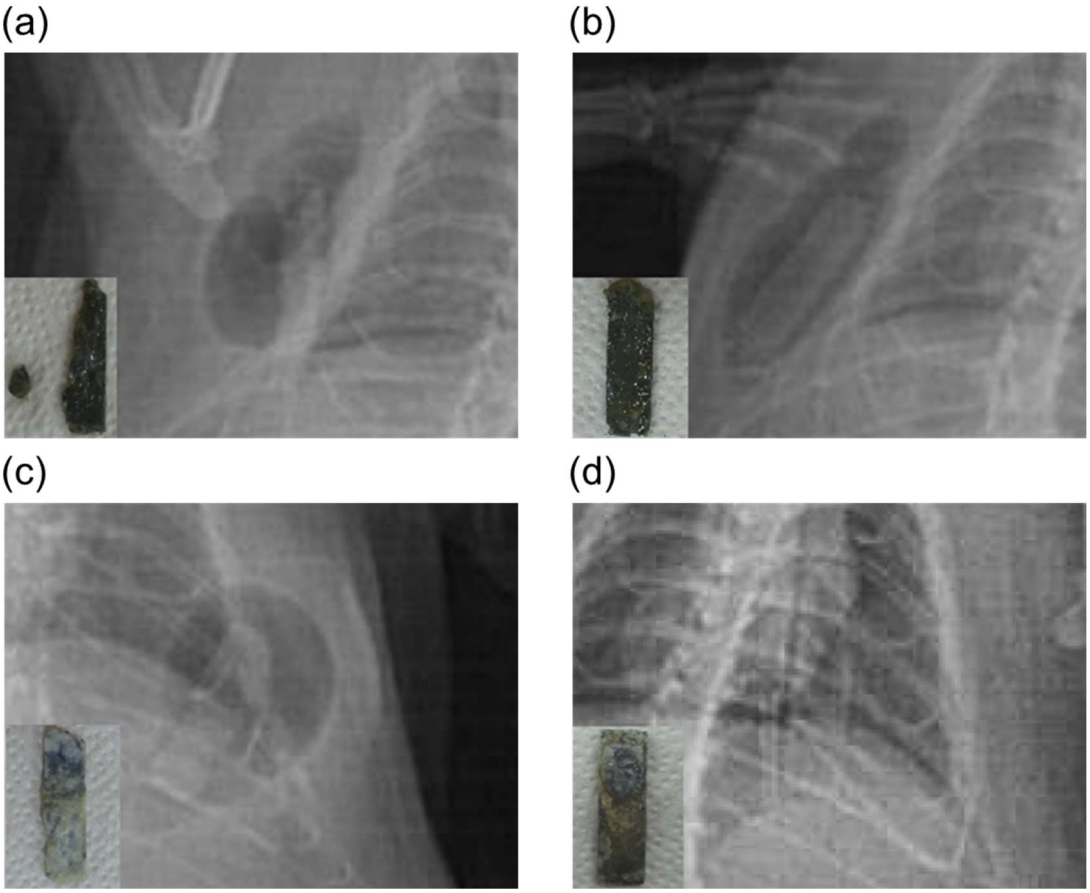


Figure 2.7. Difference in formation of hydrogen gas pockets and recovered implants from subcutaneous tissue of SD rats after 12 weeks. (a) casted Mg-Ca alloy, (b) extruded Mg-Ca alloy, (c) casted Mg-Ca-Zn alloy, and (d) extruded Mg-Ca-Zn alloy. (Cha, Han et al. 2013)

Moreover, reduced hydrogen gas formation and increased deposition of bone at the implantation site was revealed in long-term *in vivo* tests using New Zealand White Rabbits. This alloy system was approved for clinical applications by the Korean government in 2015 and by the CE for European market in 2018. A stimulatory effect on osteogenesis, is also reported with the addition of Sr into Mg-Ca alloys in recent studies and is known to be impacted through regulation of the activation of extracellular

signal-regulated kinases. Current research is focusing on developing more advanced application within the domain of load-bearing orthopaedic implants such as scaffolds, spinal cages, k-wires, bone plates, and scaffolds (Lee, Han et al. 2016, Li, He et al. 2016).

2.3.6 Fe-based alloys

In the human body, iron (Fe) is one of the most abundant metal elements. Frequently, ferrous-based alloys are used as a structural material due to good machinability and mechanical reliability of Fe (Schinhammer, Hänzi et al. 2010). The corrosion of Fe is a widely known phenomenon, which entails production of OH^- and Fe^{2+} ions when Fe is immersed in body fluid and this phenomenon yields oxidation of Fe^{2+} ions. The Fe and Fe-based alloys are known to produce biocompatible degradation products that acts as a barrier to continuous degradation by delaying the oxygen transport (Ulum, Arafat et al. 2014). As such, Fe degrades at a significantly slower rate in physiological environments and correspondingly, Fe alloy development based research is primarily focused on achieving higher corrosion rates of the alloy system (Schinhammer, Hänzi et al. 2010, Kraus, Moszner et al. 2014, Mohd Daud, Sing et al. 2014, Ulum, Arafat et al. 2014). Previously reported studies have experimented on alloying Fe-based alloys with different elements to accelerate the corrosion rate through inducing galvanic corrosion, but the results have failed to demonstrate sufficiently fast degradation rates, as in the physiological environment for a complete degradation, and where Fe based alloys have shown to require a time duration extending beyond a decade (Cheng, Huang

et al. 2014, Ulum, Nasution et al. 2015). Scholars have thereby suggested hydrolysis of polymers towards the provision of local acidity in order to accelerate dissolution of the degradation products with the purpose to overcome such slow degradation rates. When tested on human skin fibroblast cells for 72 hrs, accelerated iron degradation rates have been demonstrated in polymer-infiltrated porous iron materials without adversely affecting the cellular structure (Yusop, Daud et al. 2015). This research, however, requires further *in vivo* biocompatibility and degradation studies in order to assess the usability and practicality of such approaches in clinical practice.

2.3.7 Zn-based Alloys

Subsequent to establishment of Mg as a successful biodegradable material, Vojtech et al. (2011) reported the probability of biodegradable metallic materials based on Zn. This alloy system is completely different to the previously mentioned Zn-rich Mg glasses as the content of Zn is higher than that of Mg. It has been observed that when immersed in simulated body fluid with a pH7.4, the of Zn-based alloys' degradation rate is 1/4 slower than that of the pure Mg. Combined with good mechanical properties and excellent biocompatibility, the Zn-based alloy system provides a new alternative solution to address the issues surrounding Mg alloy systems (Murni, Dambatta et al. 2015, Alves, Prosek et al. 2017). Research conducted in mouse as regards implantation of three different Zn-based binary materials have shown corrosion rates of 0.17 mm/year, 0.19 mm/year, and 0.22 mm/year for Zn-1wt.%Mg, Zn-1wt.%Ca, and Zn-1wt.%Sr pins, respectively (Li, Xie et al. 2015). This study confirmed a threefold

increase in the compressive yield strength when compared to the pure Zn, and where the alloy system maintained its mechanical and structural integrity after 8 weeks of *in vitro* corrosion. Currently, research on Zn based alloys is largely focused on cardiovascular applications, but a rapid progress is expected in the development of orthopaedic applications in the near future.

2.4 Clinical trials of biodegradable metallic screws

For orthopaedic applications, clinical approval has been granted to three compositions of Mg-based alloy systems in different countries from their respective governing agencies. A compilation of these applications is presented in Table 2.1.

Table 2.1. Summary of recent clinical trials of orthopaedic devices

Device	Type of study	No patients	Conditions	Total duration	Outcomes
MAGNEZIX ® (Windhagen, Radtke et al. 2013)	Prospective and randomized controlled (according to EN ISO 14155–1:2009 and EN ISO 14155–2:2009)	26	Mild hallux valgus	6 months	Outstanding results for ROM, MTPJ, AOFAS. Equivalent performance to titanium screws for treatment of mild hallux valgus deformities.
RESOMET® (K-MET) (Lee, Han et al. 2016) #NCT02456415	Prospective, single center, single group, open (KFDA clinical trial approval for medical device no. 362)	53	Hand fractures	12months	Normal range of grip power. No change in ROM, DASH. At 12 months, screws were completely replaced by new bones.
Pure Magnesium (Zhao, Huang et al. 2016) # ChiCTR-TRC-13003238	Prospective and randomized pilot (Registered in the Chinese Clinical Trial registry)	48	Osteonecrosis of the femoral head	12 months	Increased bone flap stability. serum levels were normal. Two patient suffered collapse of the femoral head. At 12 months, higher Harris hip score than control.

indicate clinical trial identifiers retrieved on www.clinicaltrials.gov where available. Table adapted from (Han, Loffredo et al. 2018)

2.4.1 Pure Mg

In China, screws designed with exceptionally high purity (99.99%) magnesium have been tested for repair of vascularized bone flaps from patients presenting with Osteonecrosis of the Femoral Head (ONFH) (Zhao, Huang et al. 2016). A clinical trial registered in the Chinese Clinical Trial Registry (ChiCTR-TRC-13003238) performed

a prospective and randomized pilot trial with 48 patients suffering from association of research circulation osseous (ARCO) stage II/III. The 48 participants were aged 18 years to 55 years and divided into two groups. During the study, 23 out of those 48 patients were given the Mg screw fixation of the bone flaps during ONFH, and 25 were given the vascularized bone grafting without fixation. A subsequent Computed tomography (CT) analysis revealed higher mineral density around the Mg screws. Also, after implantation Mg screw degradation at 1, 3, 6, and 12 months was observed to be 3.7 ± 0.4%, 9.3 ± 0.8%, 13.7 ± 0.4%, and 25.2 ± 1.8%, respectively (Figure 2.7). Moreover, post-implantation in patients, Mg serum levels were observed to fall within the normal physiological range. Two patients from the Mg screw group and six patients from the control group suffered from collapse of the femoral head. A considerably higher Harris hip score in the Mg screw group after 12 months compare to control indicated a high potential for pure magnesium usage in medical applications. Recently, the Chinese FDA (CFDA) has approved the use of high purity Mg screws as a medical device; its further application for fractures of the femoral neck, femoral head, and metatarsals is actively being researched.

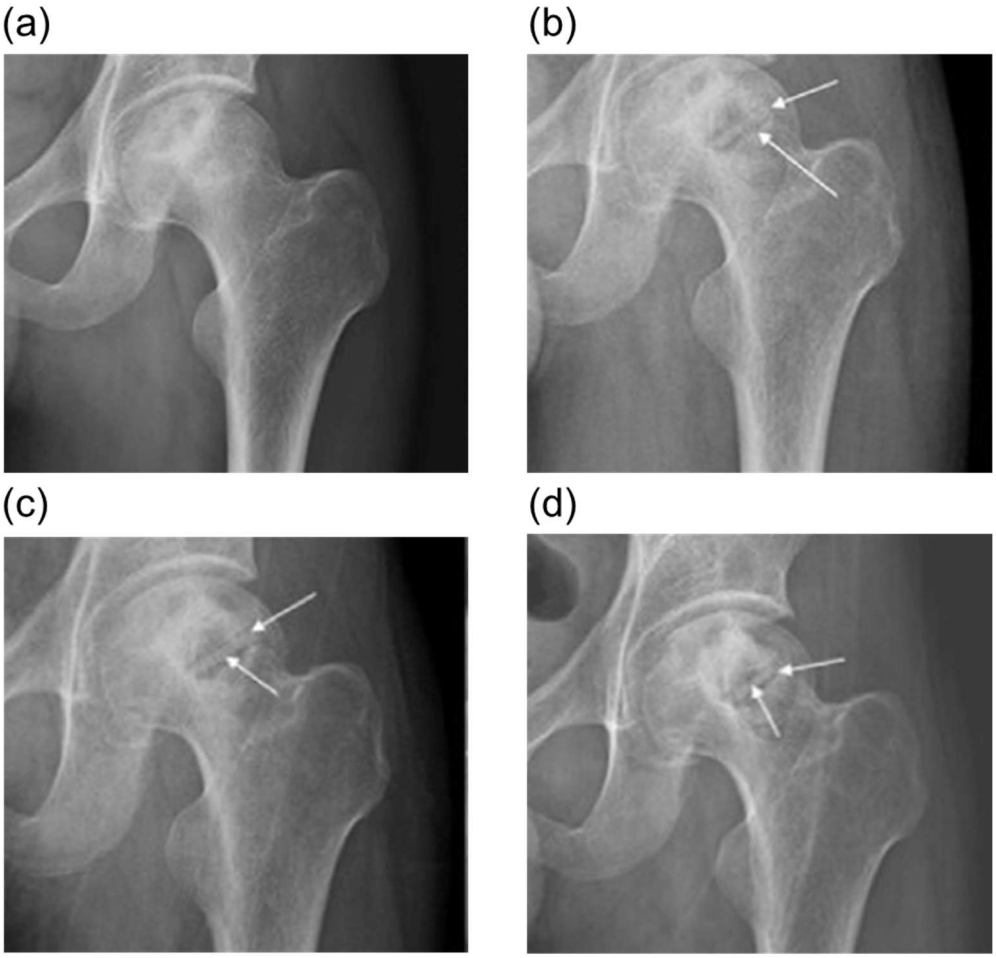


Figure 2.8. X-ray image of patient that received implantation of pure Mg screws at (a) preoperation, (b) 3 months, (c) 6 months, and (d) 12 months. (Zhao, Huang et al. 2016)

2.4.2 MgYREZr Alloy (Magnezix)

Germany reported the first use of MgYREZr alloy system as an implantable fixture in a clinical setting to treat patients with mild hallux valgus (Windhagen, Radtke et al. 2013). This prospective and randomized controlled study performed chevron osteotomy for a comparative assessment of clinical performance between a titanium

screw and MgYREZr alloy screw. The study randomly organized a total of 26 patients into two groups that received treatment with either the titanium or MgYREZr alloy screws. During the 6-month follow-up period, none of the 26 cases reported any complications, however, for personal reasons, one patient from each group dropped out of the study after surgery. Both groups, largely demonstrated excellent results for the following parameters: (i) range of motion (ROM); (ii) first metatarsophalangeal joint (MTPJ); (iii) visual analog scale for pain assessment; and (iv) postoperative American orthopaedic foot and ankle society (AOFAS) score for hallux. After 16 months, the screw was almost completely degraded without significant immunological responses as shown in Figure 2.8. These results were indicative of the comparable clinical performance of MgYREZr alloy screws to conventional titanium screws (Windhagen, Radtke et al. 2013).



Figure 2.9. 16-month postoperation X-ray image of 29-year-old female patient that received MgYREZr alloy screw after distal metatarsal osteotomy. (Plaass, Ettinger et al. 2016)

The MgYREZr alloy system, correspondingly, in 2013 received the CE mark. Subsequently, a modified chevron osteotomy study was conducted by Plaass, Ettinger et al. (2016) that included 44 patients in total, and similar results were inferred. Several recent case studies focusing on clinical application of MgYREZr alloy have reported possible utilization in fixation of distal fibular fractures and intra-articular fractures (Biber, Pauser et al. 2016, Biber, Pauser et al. 2017).

2.4.3 MgCaZn Alloy (Resomet)

The Mg-Ca-Zn alloy system was granted approval for clinical trial by the Korea Food and Drug Administration (KFDA Clinical Trial Approval for Medical Device no. 362), subsequent to which, Lee, Han et al. (2016) tested the Mg-Ca-Zn alloy system in a prospective, single center, single group, open clinical trial with the aim to evaluate its performance in the treatment of hand fractures. The trial considered 53 cases in total, which after implantation revealed a normal healing rate with continuity of the cortical bone and a reduced diameter of the Mg-Ca-Zn alloy screws and not a single failure was reported throughout the entire study. In addition, no pain indication was presented by any of the patients, and all the participants reported a recovery of normal grip power. The ROM did not show any decrease and their arm, shoulder, and hand disability score ranging from 0 to 100, indicating no disability to extreme disability, respectively, was reported to be 29.82 ± 4.4 after 6 months of surgery. Furthermore, new bone had completely replaced the Mg-Ca-Zn screws after 1 year of implantation, confirming the

genuine clinical benefits of Resomet system in orthopaedic applications (Figure 2.9). In 2015, KFDA approved Mg-Ca-Zn screws for clinical use and CE marking followed in 2018. Currently, various programs of research are under way to develop diverse prototypes utilizing this newly approved system.

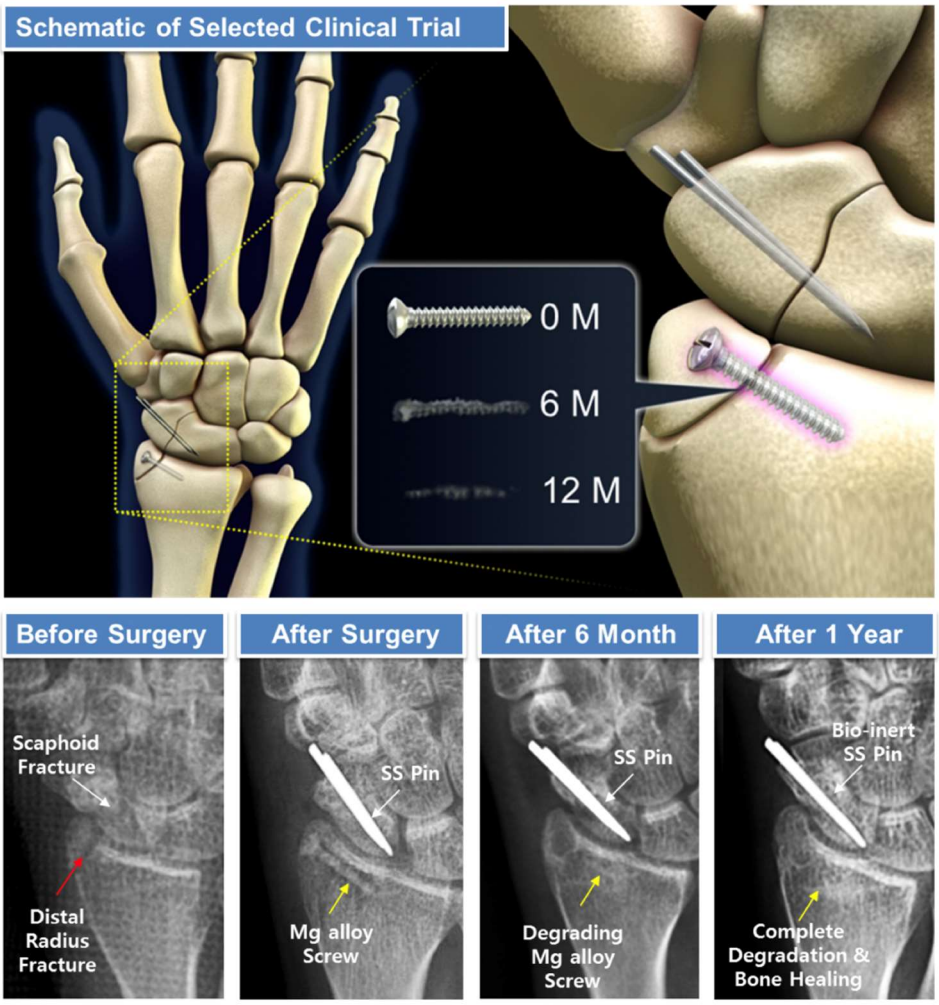


Figure 2.10. Representative clinical trial result of the Resomet implant. Scaphoid fracture was treated with conventional stainless-steel pin whereas distal radius fracture was treated with Mg alloy screw. After 1 year, fracture site shows complete degradation of Mg alloy screw and bone healing. (Lee, Han et al. 2016)

2.5 Development and optimization of Mg5Ca1Zn alloy



Figure 2.11. Development of in-house melting furnace and extrusion machine for optimization of material development process

The experiments in the following chapters were performed to evaluate the newly developed Mg5Ca1Zn alloy system. As mentioned briefly, this alloy system consists of intrinsically biocompatible elements Ca and Zn, thus rendering it as one of the most attractive biodegradable metallic materials. As an essential mineral in the human body, approximately 1% of Mg is found in blood, 49% in cells of tissue and organs and 50% exists in bones. Mg plays various roles in strengthening of bone, nervous

system and muscle function including regulation of contraction and relaxation of muscles, production of proteins and energy transportation (Zheng 2015). Zinc is an essential element found in cells throughout the human body that plays a role in cellular interactions, the immune system, and the catabolism of carbohydrates. Calcium is stored mostly stored in bone and teeth, and plays a critical role in cell signalling and maintaining the structure and function of skeletal tissues. The release of Ca ions into local cellular environments has been reported to have a positive effect in bone healing. Initially, the in-house purpose-built melting furnace and mechanical extrusion machine were used to develop this alloy system within the Korean Institute of Science of Technology as shown in Figure 2.10.

As mentioned before, the inclusion of more than 1.34 wt.%. Ca in the Mg-based alloy, results in the formation of a secondary phase Mg_2Ca with a different corrosion potential. Such differences in corrosion potential result in accelerated corrosion rates due to galvanic corrosion. In order to overcome this phenomenon, the state-of-the-art method was developed to coordinate the corrosion potentials of two existing phases (Mg + Mg_2Ca) by selectively doping Zn into the Mg_2Ca phase. In addition, the connectivity of the Mg_2Ca phases was disrupted with mechanical extrusion and thus continuous corrosion was prevented as well as the galvanic circuit formation (Cha, Han et al. 2013) (Figure 2.11).

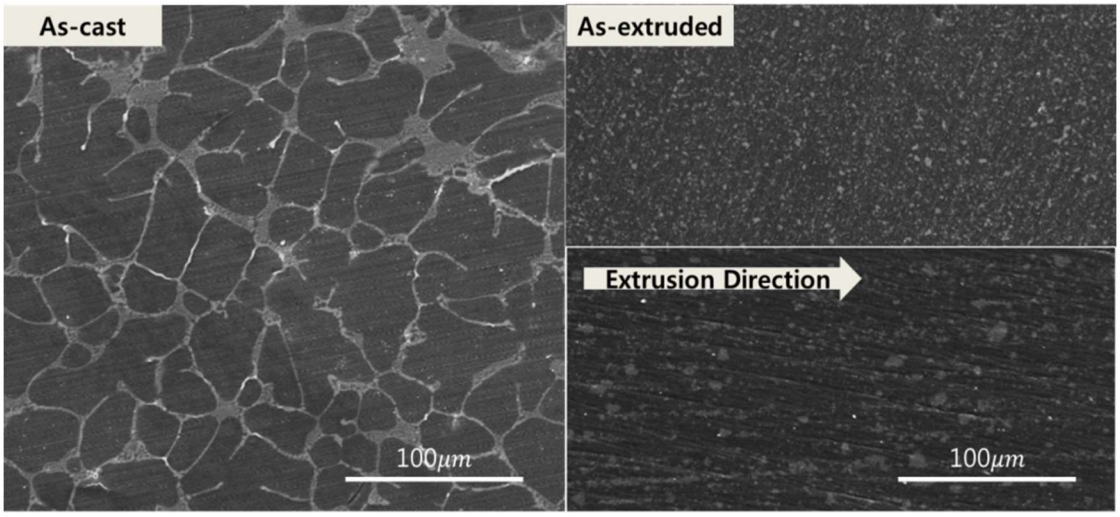


Figure 2.12. Microstructure of optimized Mg5Ca1Zn alloy after extrusion.

The alloy optimization resulted in improved mechanical properties and the yield strength (YS) and UTS both increased with increasing Ca concentration, whereas the elongation decreased. Optimized Mg5Ca1Zn alloy system showed high UCS (~380 MPa), UTS (~ 250 MPa), YS (~190 MPa) and good ductility (~10%) which is deemed sufficient for orthopaedic implant application. The animal studies have confirmed a significant reduction in hydrogen evolution as well as good tissue compatibility, in addition to increased surrounding bone deposition for this newly developed Mg-Ca-Zn alloy system (Figure 2.12).

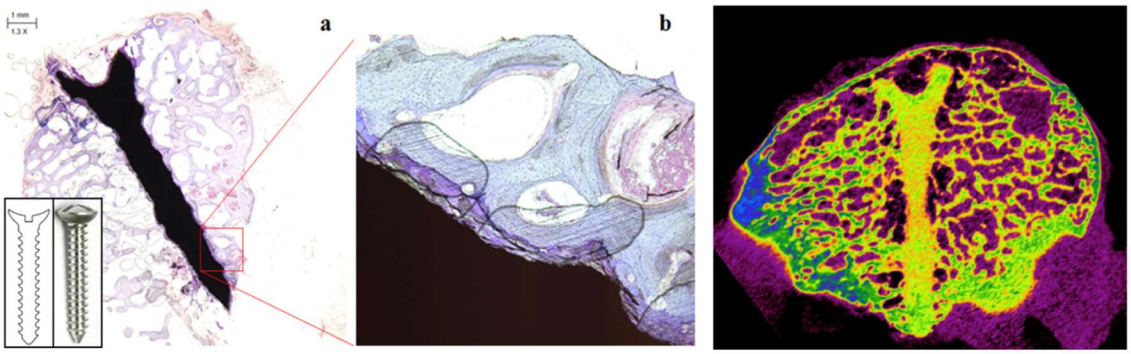


Figure 2.13. Toludine blue stain and micro CT image of mg alloy screw implanted on femoral condyle of New Zealand white rabbits for 12 weeks. (Cha, Han et al. 2013)

These studies (Cho, Chae et al. 2012, Han, Kim et al. 2012, Jung, Kwon et al. 2012, Cha, Han et al. 2013) have shown that this alloy system is well-tolerated in pre-clinical and clinical settings and provides adequate mechanical support during the initial phase of healing, before it is replaced by new bone. However, the lack of fundamental understanding in bone formation and remodelling mechanism of the degrading particles is limiting the clinical application of the developed material.

Chapter 3

Comprehensive *in vitro* evaluation of Magnesium alloy ions and extracts

3.1 Introduction

Modern medical science demonstrates extensively intriguing advances which have benefitted humanity with increased life expectancy, and this, in turn, has resulted in increased incidences of chronic diseases. Amongst these, the use of total joint replacement implants and other analogous artificial orthopaedic prostheses to repair and replace defective bone and joints are one of the more predominant chronic disorders with increased clinical burden worldwide (Christenson, Anseth et al. 2007). For a diverse range of orthopaedic applications, inert biomaterials such as titanium, cobalt chrome and stainless steel are frequently utilized based on their high corrosion resistance and good mechanical properties (Sims and Gooi 2008, Stevens 2008, Geetha, Singh et al. 2009, Bohner 2010). These permanent metallic implants however present several drawbacks such as the stress shielding effect that impedes the growth of new bone and the stability of prosthesis due to big difference in modulus of elasticity. Additional surgical procedures to remove the implant are performed after

healing to prevent discomfort, pain, and soft tissue compression. Such secondary procedures burden the patient and the healthcare system (Weinans, Huiskes et al. 1992, Vos and Verhofstad 2013). Furthermore, severe inflammatory responses due to wear particles released from the permanent implants have been demonstrated (Gu, Shi et al. 2012, Nich, Takakubo et al. 2013). In combination with subsequent osteolysis in the periprosthetic micro-environment, this release of foreign body metallic ions leads to risk of prosthesis failure and revision surgery (Goodman, Gibon et al. 2013). Recently, the factors of good biocompatibility, unique biodegradability, and natural bone aligned mechanical properties have brought research focus on magnesium and its alloys as ideal alternative orthopaedic materials. In the human body, magnesium is one of the most abundant minerals involved in several physiological processes such as bone regeneration. It is known to stimulate bone formation by interacting with alpha5beta1- and beta1-integrin proteins on osteoblast cells to facilitate cell adhesion and stability (Saris, Mervaala et al. 2000, Zreiqat, Howlett et al. 2002, Vormann 2003, Liu 2011).

Since the early 1900's, continual research efforts to instate Mg based biodegradable metals as new orthopaedic implants have been made. According to several studies (Witte 2010, Cheng, Huang et al. 2014), rapid corrosion led to the failure of initial trials using pure Mg, however, later experimental work using Mg-based alloys produced successful results showing stimulation of bone repair at fracture sites with an absence of adverse symptoms such as hypermagnesemia. Congruently, alloying Mg with various elements has significantly improved its mechanical strength and degradation rate to allow a wide range of possible applications in orthopaedics.

Several *in vivo* studies have been performed so far to display successful bone tissue regeneration (Staiger, Pietak et al. 2006, Zeng, Dietzel et al. 2008, Kirkland, Lespagnol et al. 2010). In order to assess the exact biological mechanism of Mg alloy degradation and associated impact on bone repair process, several *in vitro* studies are being conducted (Huan, Leeflang et al. 2010, Mostaed, Sikora-Jasinska et al. 2016). However, the majority of *in vitro* researches who have studied bone repair using biodegradable Mg alloy have concentrated solely on the osteoblastic activities responsible for bone formation. However, this omits crucial elements of the bone repair process offering only limited information on the exact function of Mg alloy biodegradation within the skeletal system and the bone regeneration process which involves both resorption and formation (Pietak, Mahoney et al. 2008, Yun, Dong et al. 2009, Yang, Yuan et al. 2010).

As mentioned before, the three phases of bone repair typically include: inflammatory response, renewal and remodelling phases, which are established in a sequential and overlapping manner during the repair process. During the early bone repair phase, various soluble factors and cytokines are secreted by the infiltrated active immune cells within an evolving fracture hematoma and this triggers complex pro-inflammatory signals which in turn initiate angiogenesis and maturation of putative regenerative progenitor cells (Mountziaris and Mikos 2008, Kolar, Schmidt-Bleek et al. 2010). The bone formation associated osteoblastic activities are conducted intensively in a sequential manner during the renewal phase with the development of a cartilaginous callus at the injured site. The cartilage is then mineralized which affords it greater mechanical integrity as it is subsequently replaced by woven bone.

Various signalling and regulatory molecules are common to the immune cells and skeletal cells and as such, a subsequent bone repair and remodelling process is significantly impacted by host immune system activation in response to the implanted biomaterial and its biodegradation (Xia and Triffitt 2006, Toben, Schroeder et al. 2011, Kelava, Sucur et al. 2014). The bone mass and structural integrity is maintained by continuous cycling of bone resorption, reversal and formation phases which forms a complex yet harmonious process for the constant regulation of adequate bone remodelling. Each of the bone remodelling phases necessitates the synchronized activities of various bone cells which are significantly impacted by altering local and systemic conditions (Hadjidakis and Androulakis 2006, Robling, Castillo et al. 2006). Thus the bone remodelling process can suffer abnormalities due to the slightest alteration within the bone microenvironment and yield severe skeletal disorders (Raisz 1999). Hence, it is essential to assess the impact of Mg alloy biodegradation on both bone resorption and formation. As mentioned in the earlier chapter, the Mg-5Ca1Zn alloy system was developed and optimized for application in orthopaedic procedures due to the demonstration of sufficient mechanical strength and medically acceptable degradation rates (Cha, Han et al. 2013). In this chapter, a series of conventional *in vitro* evaluations were conducted to assess the impact of micro-environmental changes from the degradation of Mg alloy on skeletal cells involved in the overall bone regeneration process using titanium, pure Mg and Mg5Ca1Zn alloy. Furthermore, released metallic ions from the Mg5Ca1Zn alloy will also be evaluated to determine their role in the bone formation process.

3.2 Materials and Methods

3.2.1 Pure Mg and Mg alloy extracts preparation

Commercially available high-purity Mg (99.98%) ingots, Ca (99.6%), and Zn (99.99%) granules were casted with melted Pure magnesium and Mg-5Ca-1Zn alloys (wt.%) using a stainless-steel crucible under an Ar atmosphere at 790℃ for 120 minutes. The as-cast Mg alloy billets were preheated to 350℃ and subsequently extruded at a ram speed of 0.2 mm/s. Plasma-atomic emission spectrometry (ICP, VARIAN710-ES) was inductively coupled to assess the samples' chemical compositions. Following which disk samples with 10 mm diameter and 1 mm height were machined and polished with 2000 grit SiC paper and then cleaned ultrasonically in ethanol. For extraction the dimensions were: surface area per extraction medium ratio 1 cm^2/ml. Six specimens were used for pure Mg and Mg alloys, which were soaked in cell culture media (10 ml) and immersed at 37℃, 5% CO_2 incubator for 1, 2 and 3 days, respectively. After extraction, a pH meter was used promptly to measure the pH change (Mettler Toledo, USA) and Quantichrom metal ion assay kit was used to measure release of magnesium, calcium and zinc ion concentrations in the extracts (Bioassay systems, USA). Quantichrom metal assay kit is designed to measure the ions directly in biological samples without any pretreatment. A calmagite dye (magnesium), chromogen (zinc), phenolsulphonephthalein dye (calcium) in the kit forms a coloured complex specifically with magnesium, zinc and calcium. The

intensity of the colour measured at 500 nm, 425 nm, and 612 nm is directly proportional to the magnesium, zinc, and calcium concentration in the sample, respectively. CCK-8 cytotoxicity assay kit was used to assess the cytotoxicity of extracts (Dojindo, Japan). Control group constituted of Ti64 alloys extracts derived using the same conditions in addition to cell culture media.

3.2.2 Cell culture

The human fetal osteoblastic cell line hFOB1.19 was purchased from American Type Culture Collection (ATCC) and cultured using a phenol red free 1:1 mixture of DMEM/Ham's F-12 medium containing 10% of heat-inactivated Fetal Bovine Serum (FBS) supplemented with 0.3mg/ml of Geneticin. The cell culture was maintained in a humidified chamber with 5% CO_2 at 33.5℃. Also, the mouse leukemic monocyte macrophage cell line RAW264.7 (ATCC) was cultured in DMEM supplemented with 10 % of FBS, 100 U/ml penicillin/streptomycin and 4 mM of L-glutamine. The culture was subsequently grown and maintained in a humidified chamber with 5% CO_2 at 37℃.

3.2.3 Assessment of osteoblast proliferation

The determination of osteoblast cell proliferation necessitated following: (i) hFOB1.19 cells seeded into 96-well culture plates; (ii) density of 1×10^3 cells, (iii)

incubated for 12 hours for allowing adherence of the cells to the plates. Cell culture media was replaced by test media, which was further incubated at 33.5℃, for a 3 days duration. Cell proliferation was assayed by cell proliferation ELISA, BrdU colorimetric kit (Roche applied science, Germany). During DNA synthesis in proliferating cells, the cells were incubated for 2 hours with the purpose to allow the DNA strand to incorporate the pyrimidine analogue BrdU instead of thymidine. Spectrophotometry was used for conducting a quantitative measurement of the substrate reaction of peroxidase conjugated anti-BrdU antibody which was specifically combined with newly incorporated BrdU (Molecular Devices, USA)

3.2.4 Measurement of cytosolic alkaline phosphatase (ALP) activity

For allowing adherence of the cells to the plates, at a density of 2×10^5 cells per well, the hFOB1.19 cells were plated into 24-well plates and incubated for 12 hours. The test sample media was supplemented with 10 mM of β-glycerophosphate, 50 μg/ml of ascorbic acid, and 100 nM of dexamethasone and incubated for 7 days at 39.5℃ after replacing the cell culture media. Every 3 days the test sample media were replaced. The cells were lysed for 1 hour with the buffer containing 50 mM Tris-HCl pH 7.4 and 0.1% Triton X-100 at 4℃. LabAssay ALP kit was used to measure the cytosolic ALP activity in the cell lysates (Wako, Japan) and subsequently BCA protein assay measured normalized relative to total cellular protein content (Pierce, USA).

3.2.5 Assessment of mineralized matrix formation

The test media was supplemented with 10 mM of β-glycerophosphate, 50 μg/ml of ascorbic acid, and 100 nM of dexamethasone; in which the hFOB1.19 cells were incubated at 39.5℃ for 30 days. Every 3 days the medium was replaced. The cultures in the plates after stimulation, were rinsed twice for which the experiment used phosphate-buffered saline and fixed in ice-cold 70% ethyl alcohol. 40 mM Alizarin red-S (pH 4.2) was used to stain the culture, for 1 hour, followed by an extensive rinsing three times with distilled water. In order to quantify calcium deposition, post photography, the bound staining was eluted with 10% (w/v) cetylpyridinium chloride. Yang, Lin et al. (2005) demonstrate that one mol of Alizarin red-S selectively binds about two mol of calcium. Correspondingly, by measuring absorbance at 550 nm and through standard curve calculation the Alizarin red-S in samples were quantified

3.2.6 Measurement of Tartrate Resistant Acid Phosphatase (TRAP) activity

Cell adhesion was obtained using plating of RAW264.7 cells into 96-well plates at a density of 1×10^3 cells per well and 12 hrs incubation.

The test medium was supplemented with 10 ng/ml of M-CSF (R&D systems, USA) and 50ng/ml of RANKL (Santa Cruz Biotechnology, USA) and incubated for 5 days at 37℃after replacing the cell culture media. Bone resorption assay kit (Cosmo bio, Japan) was used to assess the AP activity assay and TRAP staining. Chromogenic

substrate solution was added to the cell culture supernatant and incubated at 37℃ for 3 hours. BCA protein assay (Pierce, USA) was used to measure AP activity in culture supernatant and normalized relative to total cellular protein content. To achieve TRAP staining; phosphate-buffered saline and fixed with 10% formaldehyde solution was used to wash the cells at room temperature for 5 minutes. Subsequently, a distilled water wash was given to the cells, followed by a chromogenic substrate staining at 37℃ for 1 hour. The stained cells after a distilled water rinse were observed at a magnification of X40 and photographed using Olympus microscope IX70.

3.2.7 Resorption pit assay

Cell adhesion was derived using a cell plating of RAW264.7 cells at a density of 1×10^3 cells per well in 96-well osteoplate, which was coated with synthetic inorganic bone mimetics (Cosmo bio, Japan). Subsequently, post incubation, test media replaced the cell culture medium. The test media was supplemented with 50 ng/ml of RANKL (Santa Cruz Biotechnology, USA) and 10 ng/ml of M-CSF (R&D systems, USA) and incubated at 37℃ for 5 days. Followed by a 5 minutes incubation in 10% bleach solution at room temperature the cells were given a distilled water wash. The plates were completely air dried and then stained with 1% toluidine blue solution. Olympus microscope IX70 was used to concurrently photograph and observe the plates at a magnification of X100.

3.2.8 Statistics

All experiments during the research were performed at a minimum of three times, unless otherwise specified; and Graph Pad Prism (Graph Pad Prism 4.0, San Diego, CA, USA) was used to conduct the statistical analysis. In concurrence with the Tukey and Bonferroni multiple comparison tests, variance analysis (ANOVA) was utilized in the current study to analyse the statistical significance of difference between each experimental values and control values. Results are presented as mean values ± standard deviation (SD). The differences among means were considered significant if the p value is $*p<0.05$, $**p<0.01$, $***p<0.001$.

3.3 Results

3.3.1 Chemical composition and degradation profile of pure Mg and Mg alloy extracts

The ICP was used to determine the chemical compositions of the Mg alloys used in this study, and Table 3.1 summarizes the same. As presented in Table 3.2 and Figure 3.1, pH changes, released quantity of Mg and Zn ions, cytotoxicity of Mg alloy extracts' and metal ion were measured; following which the results were compared with control media and Ti64 alloy extract. The results showed an increase in the pH level and accumulated concentration of metallic ion contents in Mg alloy extracts which was proportionate to their corrosion rate and extraction time.

Table 3.1. Chemical composition (wt.%) of Mg alloys.

	Chemical composition (Wt%)							
Alloys	**Ca**	**Zn**	**Fe**	**Ni**	**Mn**	**Si**	**B**	**Mg**
Pure Mg	-	-	<0.002	<0.002	<0.001	<0.001	<0.002	99.98
Mg5Ca1Zn	4.98	1.28	0.0052	<0.002	<0.001	<0.001	<0.005	Bal.

Table 3.2. Change of pH over time and accumulation of released ions from the alloy extracts. Values are expressed as the mean ± standard deviation from the mean.

Extraction time	pH value			Mg^{2+} (mM)			Zn^{2+} (uM)		
	1day	2days	3days	1day	2days	3days	1day	2days	3days
Ti64	7.44±0.02	7.32±0.03	7.29±0.01	-	-	-	-	-	-
P.Mg	7.95±0.07	8.01±0.04	8.12±0.11	1.78±0.39	4.12±0.12	7.00±0.07	-	-	-
Mg5Ca1Zn	7.86±0.15	7.89±0.16	7.95±0.07	1.53±0.23	3.33±0.20	4.65±0.22	0.60±0.14	1.47±0.56	1.61±0.31

After 3 days, the Mg ions concentrations in pure Mg extracts were increased by 7 mM approximately and by 4.65 mM in Mg alloy extracts. Additionally, approximately 1.61 μM of Zn ions in Mg alloy extracts were measured however, despite the presence of 5% of calcium within the alloy system no significant increase was evident for Ca ions. Prior to the cytotoxicity analysis of alloy extracts, the cytotoxicity of constituent metallic ions of the alloy system was evaluated using hFOB1.19 and RAW264.7 cell lines. For concentrations below 10 mM of Mg, Ca and 100 μM of Zn, the analysis revealed no significant cytotoxic effect. In prepared pure Mg and Mg alloy extracts the level of released metal ions, as described above, was found to be lower than the toxic level, and no significant cytotoxicity was observed in both extracts. At the beginning of the corrosion period, the pH of pure Mg extracts was promptly raised to 7.95 and then after 2 days gradually stabilized near 8.12. In contrast, for the same duration, the pH change from 7.86 to 7.95 was observed in Mg5Ca1Zn alloy extracts. Also, a physiological pH range of 7.2–7.4 was sustained for the Ti64 alloy extracts.

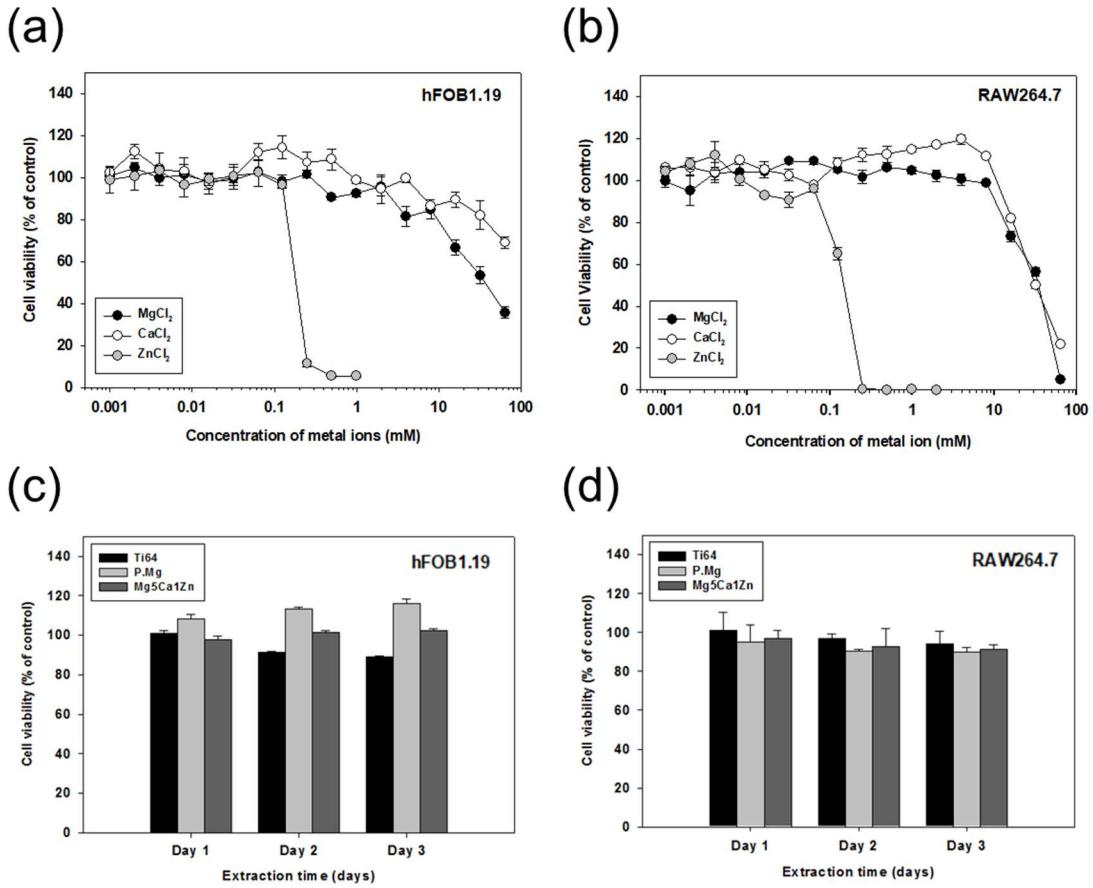


Figure 3.1. Cell viability of metal ions and alloy extract samples. The cytotoxicity of Mg,Ca, Zn ions and extracts from control Titanium alloy (Ti64), pure Mg and Mg5Ca1Zn alloy samples were determined respectively. hFOB1.19 cells and RAW264.7 cells were cultured with test ions/extracts for 24 hours and the cytotoxicity was measured by using Cell Counting Kit-8 (CCK-8). The cytotoxicity of (a) hFOB1.19 and (b) RAW264.7 in presence of 1~64mM of $MgCl_2$, 1~64mM of $CaCl_2$ and 1~1000uM of $ZnCl_2$. The cytotoxicity of (c) hFOB1.19 and (d) RAW264.7 in prepared alloy extracts.

*$p<0.05$, **$p<0.01$, ***$p<0.001$

3.3.2 Effect of Mg alloy extracts on osteoblasts cells and bone formation in presence of released metallic ions.

In order to assess the Mg alloy biodegradation impact on bone formation related osteoblastic activities, hFOB1.19 cells were cultured with alloy extracts or metal ion supplemented cell culture media. This facilitated the identification of their effects on (i) osteoblast proliferation, (ii) differentiation and (iii) extracellular matrix mineralization. In both pure Mg and Mg alloy extracts an approximate 10~20% increase in osteoblast proliferation was observed in comparison to control media. The proliferation was observed to be significantly higher in both pure Mg and Mg alloy when compared to Ti64 alloy extracts (Figure 3.2A). In addition, pH-uncontrolled and pH-controlled (pH 7.3) pure Mg and Mg alloy extracts were used to assess the pH effect on osteoblast proliferation, which, in fact, did not demonstrate any statistically significant differences. The culture media constituted of metal ions displayed similar results. Figure 3.2B illustrates the approximate 20% increase in proliferation in 20 mM of Mg ions with the dose-dependent osteoblast proliferation increase in the presence of Mg ions. The osteoblast proliferation also impacted a 10% increase due to Zn ions which was observed in the range of 1~20 μM.

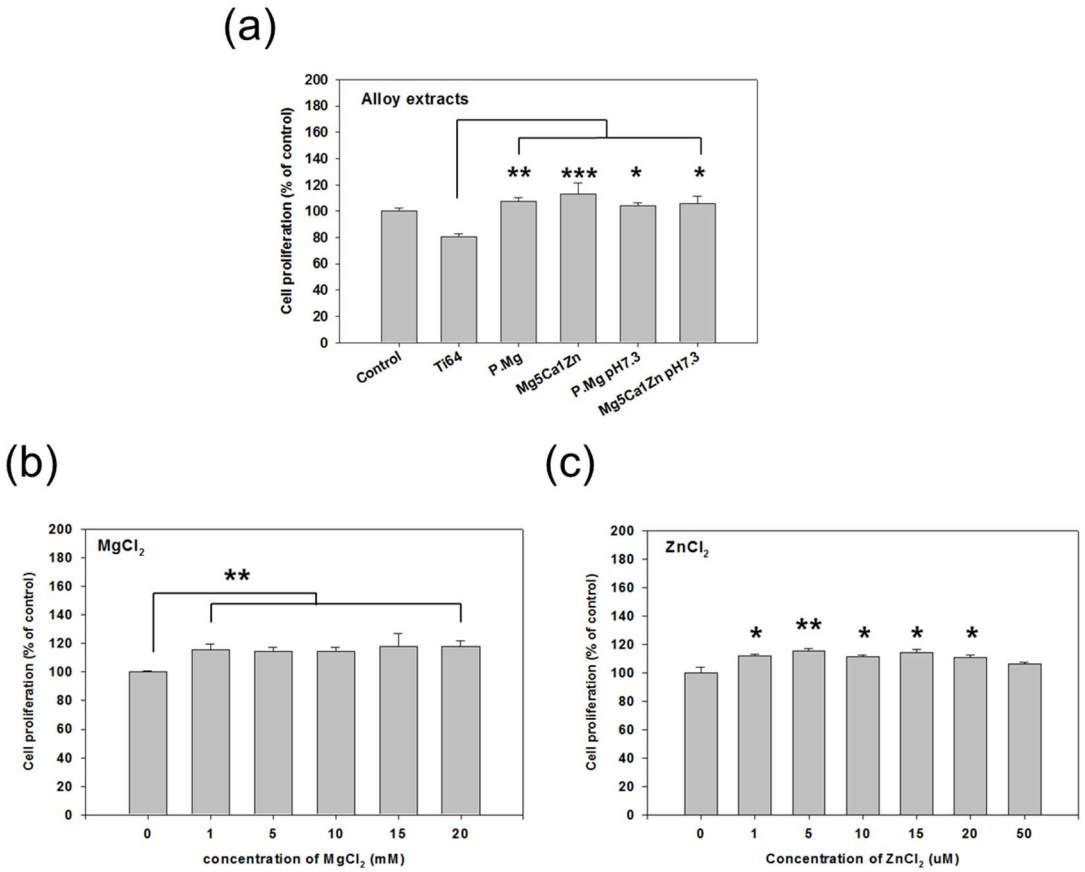


Figure 3.2. hFOB1.19 proliferation in presence of alloy extracts and metal ions. Cells were cultured for 3 continuous days in test samples and cell proliferation ELISA BrdU kit was used to measure the proliferation. The colorimetric changes were read at 370 nm. (a) hFOB1.19 proliferation in extracts from Ti64 and Mg alloy. (b) hFOB1.19 proliferation in presence of 1~20mM of $MgCl_2$ and (c) 1~50uM of $ZnCl_2$. *p<0.05, **p<0.01, ***p<0.001

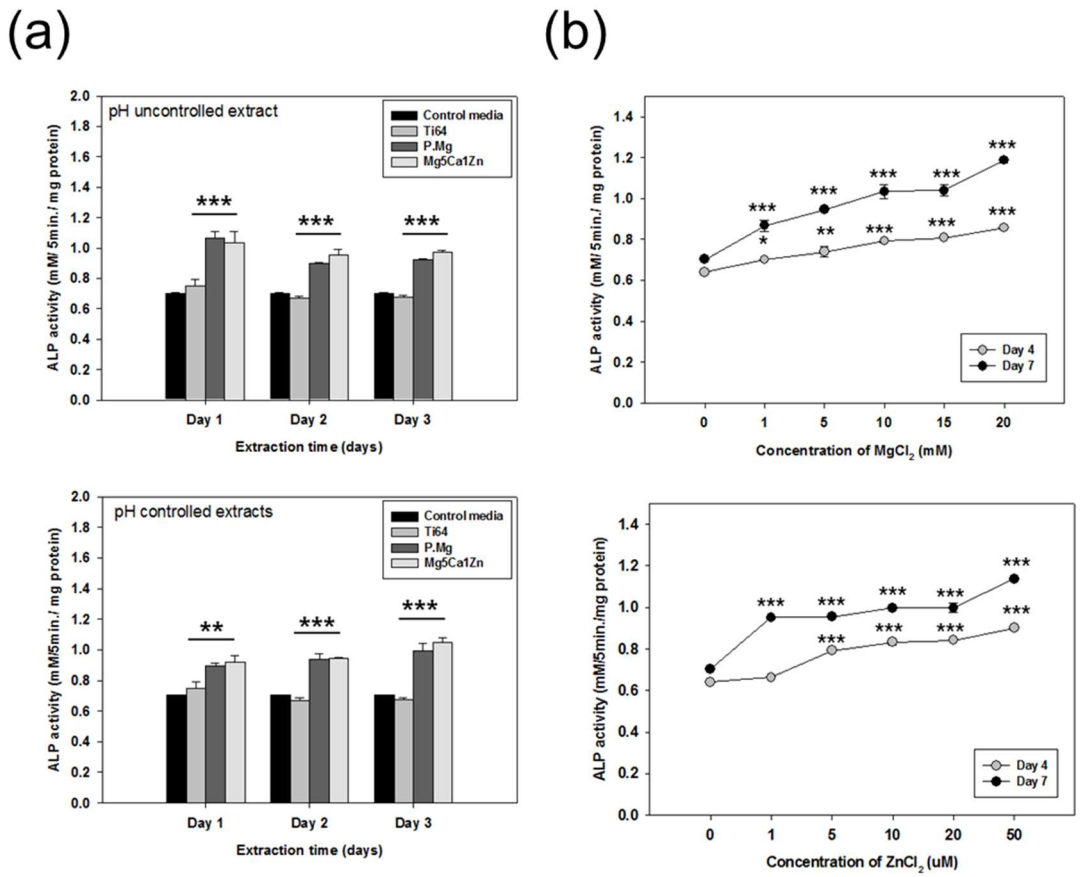


Figure 3.3. The ALP activity evaluation of hFOB1.19 cells cultured with metallic ions and alloy extracts. The cells were cultured for 7 continuous days in media containing test samples supplemented with differentiation factors. The ALP activity of cell lysates was measured and normalized to total cellular protein content. (a) The ALP activity from differentiated hFOB1.19 cells in pH-uncontrolled and pH-controlled test sample extracts. (b) The ALP activity from differentiated hFOB1.19 cells in the presence of 1~20mM of $MgCl_2$ and 1~50uM of $ZnCl_2$.

*p<0.05, **p<0.01, ***p<0.001

The hFOB1.19 cells were subsequently cultured with alloy extracts or metal ion containing culture media, supplemented with differentiation reagents. After culture for 7 days, alkaline phosphatase activity was analysed and osteoblast differentiation and extracellular matrix mineralization was assessed at day 30 to explore the subsequent impact on mineralized matrix formation. Figure 3.3A illustrates the 30~40% enhanced cytosolic ALP activity in pure Mg and Mg alloy extracts in comparison with Ti64 alloy extracts or control media. In both pH-uncontrolled and pH-controlled Mg alloy extracts, there was an increase in the ALP activity, and the extracts, however, did not present any significant differences from the pH. The ALP activity was observed to increase amongst the Mg and Zn ions in culture media on basis of concentrations with the activity depicting a 2-fold increase in 20 mM of Mg and 50 μM of Zn ions (Figure 3.3B).

Figure 3.4 illustrates the stimulation of extracellular matrix mineralization in response to pure Mg and Mg alloy extracts. Alizarin red-S staining is widely used to evaluate the calcium deposits and mineralization in cell culture. Mineralization is assessed by bright red stain which is formed in a chelation process of Alizarin red-S-calcium complex. The Alizarin red-S staining clearly illustrates the higher production of mineralized bone nodules by the osteoblasts cultured in pure Mg and Mg alloy extracts in comparison to Ti64 alloy extracts or control media.

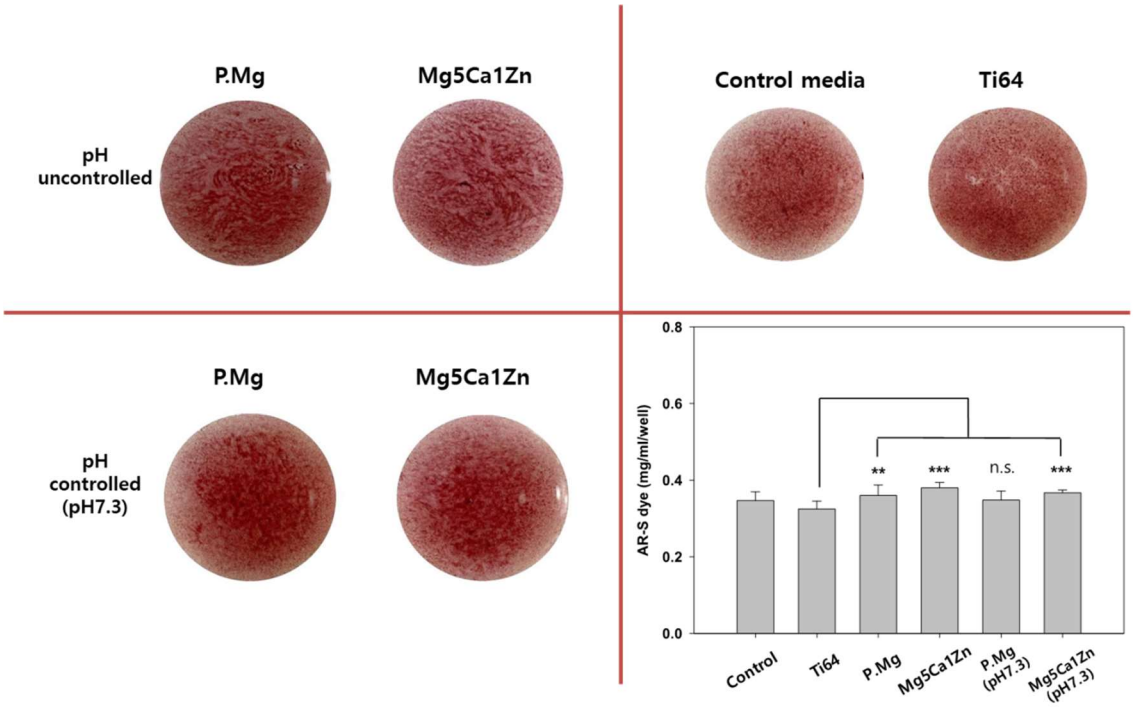


Figure 3.4. Evaluation of extracellular matrix mineralization of hFOB1.19 cells in the presence of test sample extracts by alizarin red-S staining. The cells were cultured for 30 continuous days with test sample extracts supplemented with differentiation factors and mineralized matrix was detected with alizarin red-S staining. $*p<0.05$, $**p<0.01$, $***p<0.001$

Figure 3.5 illustrates the significant increase in the bone matrix mineralization from treatment of Mg ions. Increasing concentrations to 20 mM of Mg ions resulted in quantification of more than 20% increase of deposited minerals. The mineral deposition was also increased with more than 20 μM concentration of Zn ions, however, compared to Mg ions, the results were relatively less effective. It was observed that the bone formation process was up-regulated by the Mg alloy extracts with inclusion of proliferation, differentiation and mineral depositions. The critical

roles of Mg and Zn ions in the stimulation of matrix mineralization were emphasized in subsequent results.

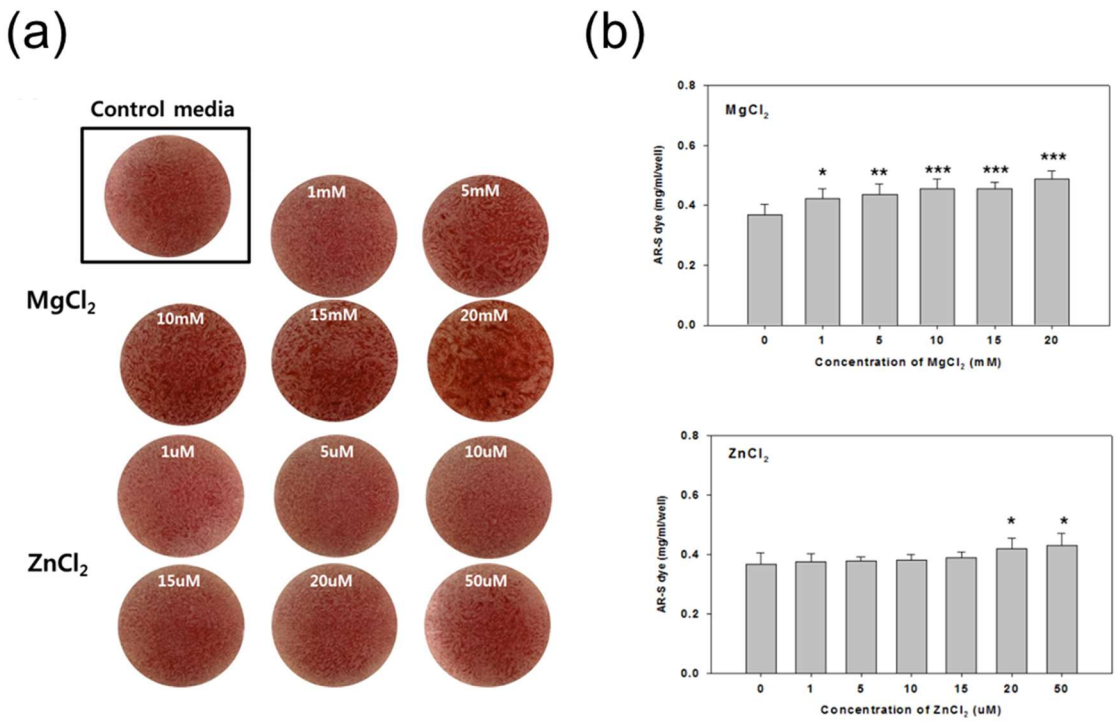


Figure 3.5. Evaluation of extracellular matrix mineralization of hFOB1.19 cells in presence of Mg and Zn ions. The cells were cultured for 30 continuous days with differentiation culture media containing 1~20mM of $MgCl_2$ and 1~50uM of $ZnCl_2$ for and mineralized matrix was detected with alizarin red-S staining. (a) AR-S staining of hFOB1.19 in presence of Mg and Zn ions. (b) Quantitative results summarized in graph. **p*<0.05, ***p*<0.01, ****p*<0.001

3.3.3 Effect on osteoclast activities by the Mg alloy extracts and in presence of released metallic ions.

In order to assess the impact of Mg alloy biodegradation on bone resorption, osteoclast differentiation media containing alloy extracts or metallic ions was used to culture the osteoclast precursor cell line RAW264.7 for 5 days after which acid phosphatase activity assay, TRAP staining, and resorption pit assay was performed. Figure 3.6 (a) illustrates the significant decrease in AP activity of osteoclasts on day 2 and 3 for pH-uncontrolled pure Mg and Mg alloy extracts. Figure 3.6 (b) shows the presence of numerous stained and multinucleated osteoclasts for control and Ti64 group, whereas both pure Mg and Mg alloy extracts groups only presented few differentiated osteoclasts. It also shows the complete inhibition of resorption pit formation in both pure Mg and Mg alloy extracts. There was a decrease in the osteoclast differentiation in pH-uncontrolled Mg alloy extracts, and the effect was relatively less for the pH-controlled Mg extracts.

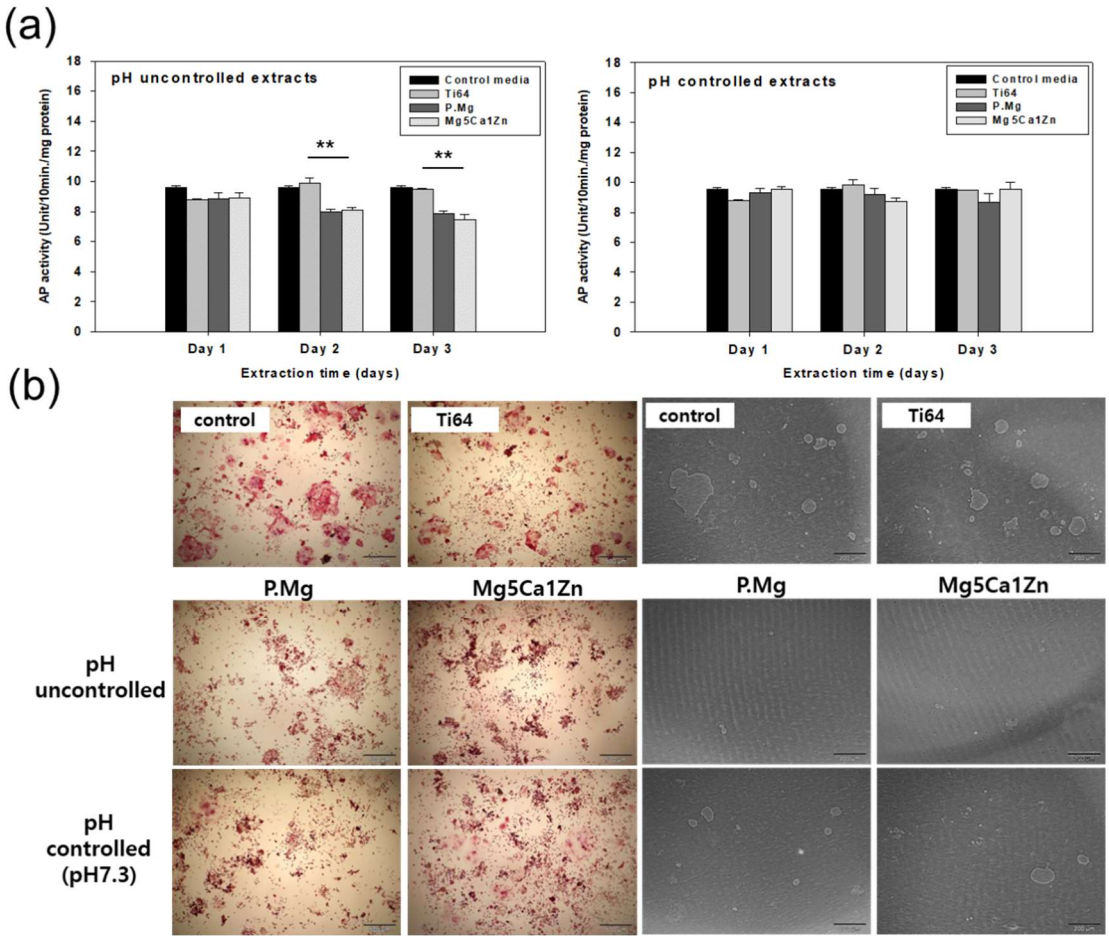


Figure 3.6. Evaluation of RAW264.7 cell activity in pH uncontrolled and controlled alloy extracts. The cells were cultured for 5 continuous days with test sample extracts supplemented with differentiation factors. (a) The AP activity of differentiated RAW264.7 in test alloy extracts at 5 days normalized to total cellular protein content. (b) TRAP staining and resorption pit assay of differentiated RAW264.7 cells. Scale bar represents 50 μm.

*p<0.05, **p<0.01, ***p<0.001

The presence of Mg ions, in fact, significantly inhibited the osteoclast differentiation. As seen in Figure 3.7 (a), the presence of Mg ions significantly decreased AP activity of osteoclasts by approximately 20%, at 15 mM of Mg ions. Figure 3.7 (b) shows the rapid decrease in differentiated osteoclasts numbers from 5 mM of Mg ions, in AP staining with a complete inhibition of the osteoclast differentiation in presence of 20 mM of Mg ions. The resorption pit assay also evidenced the inhibitory effect of Mg ions as regards the osteoclast differentiation (Figure 3.7C). In contrast, the analysis did not reveal any significant impact of Zn on osteoclast activity. The results revealed an inhibition of osteoclast differentiation by both pure Mg and Mg alloy extracts, and the inhibition effect was more effective in pH-uncontrolled alkaline pH having pure Mg and Mg alloy extracts. Furthermore, in the presence of Mg ions osteoclast differentiation and activation were found to be significantly inhibited in a dose dependent manner. Thus, the significance of alkaline pH and Mg ion for controlling osteoclast differentiation and activation was highlighted by these results.

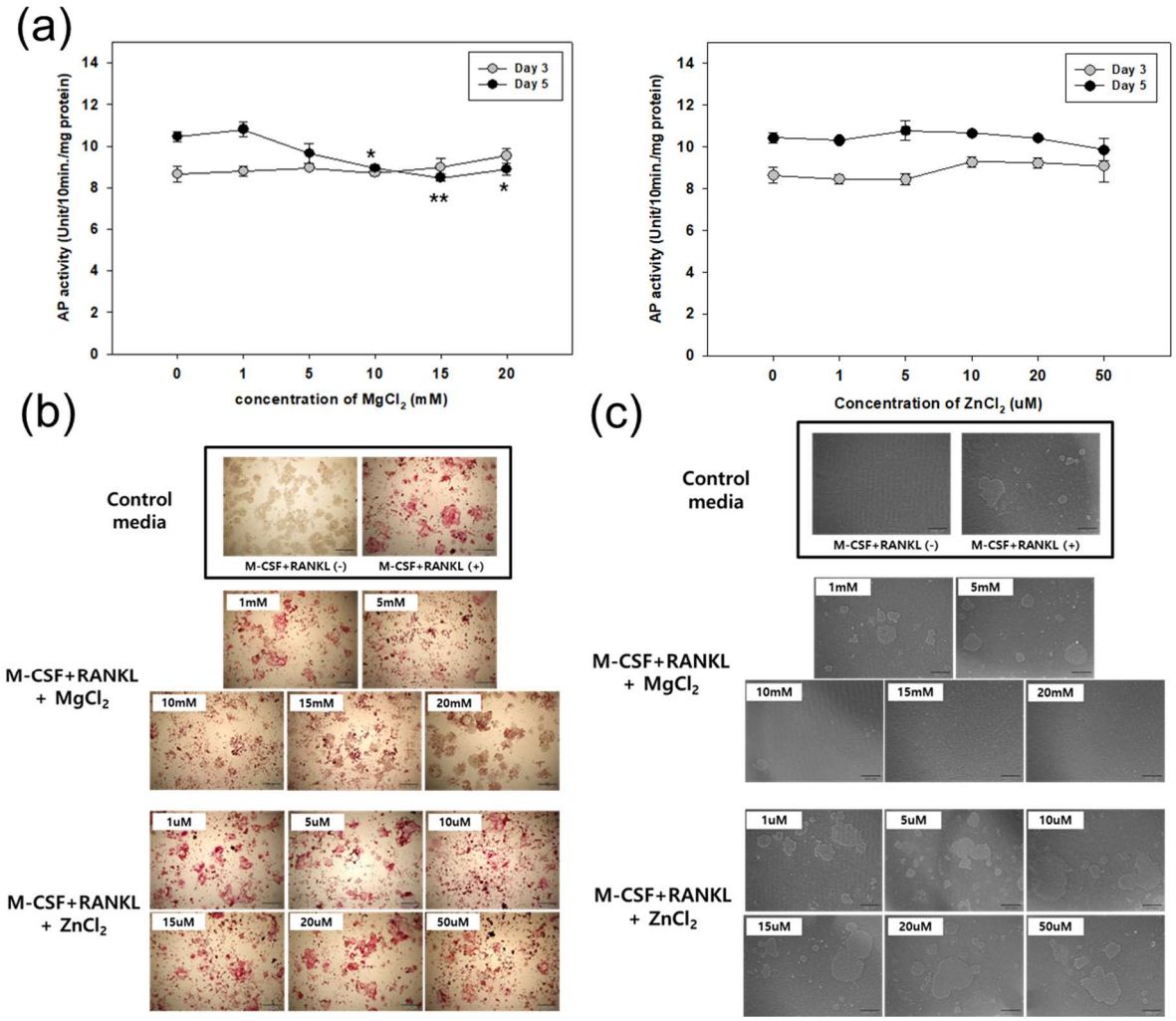


Figure 3.7. Evaluation of RAW264.7 cell activity in presence of Mg and Zn ions. The cells were cultured for 5 continuous days with differentiation culture media containing 1~20mM of $MgCl_2$ and 1~50uM of $ZnCl_2$. (a) Quantified AP activity of differentiated RAW264.7 cells in presence of 1~20mM of $MgCl_2$ and 1~50uM of $ZnCl_2$ normalized to total cellular protein content. (b) TRAP staining and resorption pit assay of differentiated RAW264.7 cells. Scale bar represents 50 μm.

*$p<0.05$, **$p<0.01$, ***$p<0.001$

3.4 Discussion

Lately the research on biomedical Mg alloys has concentrated on advanced Mg alloy system development with good mechanical and biological performance as well as slower degradation rate (Song 2007, Seal, Vince et al. 2009, Hornberger, Virtanen et al. 2012). As such, Mg5Ca1Zn alloy have demonstrated several characteristic features like, uniform degradation rate, non-toxic biocompatible alloying elements, and sufficient mechanical property, which qualify it as one of the most ideal alloy systems. The biodegradable Mg alloy, in contrast to the permanent metals, demonstrates robust micro-environmental changes during the corrosion process, until its complete degradation. Correspondingly, for potential utilization in human patients, it is imperative to attain a comprehensive understanding of the bioactivities impacted by Mg alloy biodegradation and associated physiological effect of micro-environmental changes in conjunction with biocompatibility (Witte, Hort et al. 2008, Virtanen 2011). In addition to Mg, Ca and Zn have been classified as essential minerals that play an important role in the bone metabolism process for growth, development and maintenance. Ca is known as an essential mineral that maintains bone mass and structure. Several studies, have highlighted a stimulation of osteoblast differentiation and improvement in osteoblast survival, cell adhesion, and proliferation due to an increase in extracellular Ca ion concentration (Maeno, Niki et al. 2005, Liu, Lu et al. 2009, Nakamura, Matsumoto et al. 2010). Also, the most abundant intracellular trace element Zn, has been observed to be primarily involved in functions of a structural, catalytic and regulatory nature in nearly 300 enzymes for

metabolizing macromolecules. Zn is also known to improve the bone formation by stimulation of (i) cell proliferation; (ii) bone matrix protein synthesis as well as (iii) gene expression involved in osteoblast differentiation (Wang, Zhang et al. 2007, Seo, Cho et al. 2010). The Mg alloy extracts used in this study contained released metallic ions in significant amount and demonstrated an increased pH value. Also, the variations range of such ions and pH value showed a close relationship between the corrosion rate and extraction time. In the pure Mg extracts, higher pH and Mg ion concentrations were observed when compared to Mg alloy due to a relatively faster corrosion rate. While the Mg alloy extracts did not show any significant Ca ion release, additional Zn ions were identified with increased concentrations as time progressed. Lazic (1995) attributes this differential results to specific characteristics of Ca ions which readily form calcium phosphate precipitates in culture media of alkaline pH.

In order to assess the impact of the micro-environmental changes related to Mg alloy biodegradation on bone formation, the osteoblast cells were cultured with pure Mg and Mg alloy extracts or metal ion supplemented culture media. Both pure Mg and Mg alloy extracts showed an improvement in the overall osteogenesis process with approximately 20~30% increase in osteoblast proliferation. Irrespective of pH adjustment, both pure Mg and Mg alloy extracts demonstrated an increase in ALP activity, a marker of osteoblast differentiation and osteoblastic activity. In addition, the osteoblasts cultured with pure Mg and Mg alloy extracts produced densely deposited mineral bone nodules in much higher quantity. Subsequent test results using metal ions well validated the effects demonstrated in pure Mg and Mg alloy

extracts. Particularly, greater bone formation was yielded due to the increased proliferation and differentiation of osteoblasts with the addition of Mg ions in culture media. Zn ions also demonstrated a stimulating effect on bone formation, however, Mg ions results showed higher efficiency. Notably, even at extremely low concentration, in comparison to Mg ions, Zn ions demonstrated both osteoblast proliferation and differentiation (i.e., at 1uM). Furthermore, the osteoblast proliferation, ALP activity and matrix mineralization demonstrated a similar increase in both the Mg5Ca1Zn alloy extracts containing 4.65 mM of Mg ions and the Pure Mg extracts containing much higher Mg ion concentration, 7 mM, which can be attributed to Zn ions present in Mg5Ca1Zn extracts. Thus, the findings indicate that despite the reduced quantity of Mg ion due to slower biodegradation rate, the bone formation process is stimulated sufficiently with Mg alloys release of metal ions Ca and Zn.

The impact of Mg alloy biodegradation on the bone resorption phase was assessed through culturing monocyte-macrophage cells as osteoclast precursors with pure Mg and Mg alloy extracts. Also, their impact on inflammatory conditions closely associated with osteolysis was investigated in the presence or absence of inflammatory stimuli. After injury, the local and strictly controlled inflammatory reactions during the initial stages are imperative for adequate bone repair as they stimulate osteogenesis and angiogenesis. However, prolonged hyper-inflammation within the bone micro-environment and the strong systemic inflammatory response interferes with osteoblast differentiation while concurrently triggering osteoclast maturation and inflammatory osteolysis that eventually lead to bone repair

impairment (Boyle, Simonet et al. 2003, Goldring 2003, Mountziaris and Mikos 2008, Rucci 2008, Bastian, Pillay et al. 2011, Ajai Singh 2012). In both Mg and Mg alloy extracts, osteoclast-mediated resorption pit formation as well as levels of the osteoclast marker tartrate-resistant acid phosphatase was found to be considerably decreased. However, in pH-controlled Mg alloy extracts such inhibitory effect was reduced. This differentiation is due to the decrease of TRAP activity by Mg ions at concentration higher than 10 mM, which is higher in comparison to the released Mg ions (7 mM) in the Mg alloy extracts. pH-controlled Mg alloy extracts demonstrated reduced osteoclastic activity and showed a significant inhibitory effect of alkaline pH (in addition to Mg ions) on osteoclastic activity. The high dependence of bone turnover on changes in local pH level has been studied in numerous publications. In general, bone fracture when accompanied with vasculature disruption leads to fracture hematoma with tissue hypoxia and causes low pH and high lactate concentration. This is consequent to insufficient local oxygen supply and nutrient deficiency at the fractured site. During the fracture healing process, local acidosis affects the bone cells development. Several *in vitro* studies have demonstrated that the reduction of extracellular pH to 7.0 or below hinders the progress of bone formation and stimulates osteoclastic activity to result in bone mineral dissolution and matrix protein degradation by upregulating cathepsin K. Furthermore, studies using biodegradable polyesters have reported local acidosis adversely impacting the bone formation due to the generation of acidic degradation products during hydrolysis. Conversely, bone formation is apparently promoted by alkaline pH through osteoblast

proliferation and osteogenic activities augmentation (Brandao-Burch, Utting et al. 2005, Arnett 2008, Arnett 2010, Kolar, Schmidt-Bleek et al. 2010).

The inflammation related periprosthetic osteolysis is an imperative issue in development of both bioinert permanent metallic implants and biodegradable materials. Over time, biomedical materials could release residual wear particles, produce metal ions and corrosion by-products that stimulate an inflammatory cascade. This cascade can yield bone loss and result in subsequent aseptic loosening which is one of the significant causes for revision surgery (Haynes, Crotti et al. 2004, Purdue, Koulouvaris et al. 2006, Gu, Shi et al. 2012, Nich, Takakubo et al. 2013). Biodegradation of implanted Mg entails various micro-environmental changes which have a multifaceted impact on several regeneration cellular activities relevant to injured bone and surrounding tissue. Attributed to bone formation stimulatory effects and their robust mechanical properties, Mg based biodegradable metals are popularly considered as one of the most promising orthopaedic biomaterials. The results from this chapter suggest that transitional changes of bone micro-environment such as released metallic ions and local alkaline pH can contribute towards the bone formation process by facilitating the osteoblastic cell activity and promote a reduction in osteoclastic activity at the implant site in a direct and indirect manner. In fact, such inhibitory effects may provide further potential evidence to support the highly desirable bone formation results from reported *in vivo* tests. Thus, the optimized Mg alloy show features that indicate high probability of periprosthetic osteolysis prevention and subsequent aseptic loosening.

3.5 Conclusion

In this chapter, the impact of Mg alloy biodegradation, specifically on the skeletal cells associated with the bone regeneration progress was evidenced through conducting a series of comprehensive *in vitro* evaluations of released ions from pure Mg and Mg5Ca1Zn alloy. It was observed that an overall improvement was achieved in osteogenesis through release of metal ions at similar rates from both pure Mg and Mg alloy extracts. This indicates an optimal stimulation of bone formation process due to the release of metal ions from Mg alloys, irrespective of reduced biodegradation rate and quantity of released Mg ion. The findings from this study also indicate that bone tissue regeneration can be facilitated by released metal ions from Mg alloy through reduced osteoclastic activity at the implant site.

Chapter 4

Evaluation of bone formation using hydroxyapatite scaffold in a perfusion bioreactor

4.1 Introduction

In Chapter 3, a series of conventional *in vitro* evaluations of the Mg alloy confirmed the positive effect of releasing metallic ions (Mg, Ca, and Zn) on skeletal cells related to the bone regeneration.

Although such a conventional approach allows the observation of bone cell growth and proliferation, it does not accurately portray the 3D *in vivo* environment into which biodegradable metals will be applied. The corrosion profile of biodegradable metals depends heavily on the local environments and the experimentation must simulate the key aspects of *in vivo* condition such as blood flow-induced magnesium corrosion, hydrogen evolution, and local pH change for the accurate evaluation of newly developed biodegradable materials. Since the surface of the metal is immediately in contact with the blood and surrounding tissues, the blood flow plays a vital role during the initial stage of implantation (Wang, Jang et al. 2016), and several studies have shown that the rate of the corrosion is increased for the samples

immersed in dynamic flow condition (Chen, Zhang et al. 2010, Wang, Giridharan et al. 2014). A conventional static culture system is designed for the testing of materials that are corrosion resistant and does not take the key aspects of biodegradable materials into consideration. Furthermore, the transport of nutrients occurs only by diffusion in static culture conditions and the absence of cell culture medium circulation often results in increased nutrient and metabolite concentrations on the surface of the material which might inhibit cell migration and tissue formation (Gaspar, Gomide et al. 2012). The lack of oxygen transport and removal of waste from a 3D scaffold in static culture also lead to a non-uniform distribution of cells and decreased proliferation and differentiation (Sailon, Allori et al. 2009). Consequently, more advanced bioreactor systems were developed by researchers to simulate the circulation of blood and facilitate transportation of oxygen and nutrients to the cells in 3D scaffolds. The bioreactors have several advantages over conventional 2D culture system and allow seeding of cells on materials under dynamic flow condition while allowing increased transport of media in 3D structure. Also, it reduces the potential of contamination by reducing the handling steps and enables control of local environmental conditions like pH, oxygen, and CO_2 concentration (Yeatts and Fisher 2011). For the accurate evaluation of orthopaedic implant devices, it is crucial to consider the flow-induced stress and resulting mechanical stimulation on cells from the perfusion of culture media. Studies have shown the increase of various bone formation markers and increased proliferation and mineralization of osteoblast under mechanical loading (Kim, Kim et al. 2007). It is believed that mechanical loading is responsible for interstitial fluid flow through

canalicular and lacunar spaces in bone and such mechano-stimulation from fluid flow influence the proliferation and differentiation of cells occupying these spaces (Sikavitsas, Temenoff et al. 2001, Sikavitsas, Bancroft et al. 2003).

One of the most commonly used bioreactor types in bone tissue engineering is perfusion systems (Janssen, Oostra et al. 2006, Alvarez-Barreto, Linehan et al. 2007). The perfusion bioreactors are often classified as direct or indirect systems that consist of several key parts including a perfusion chamber where scaffold and cells are placed, a reservoir where culture medium is stored, and a pump to enable transport of media through the perfusion chamber. For direct perfusion bioreactors, cells are seeded on press-fitted scaffolds in the perfusion chamber to allow culture media to pass through the scaffold. Several studies have demonstrated the potential of direct perfusion bioreactor system as suitable culture system for evaluation of new materials for future application in clinical settings. However, relevant bioreactor studies using the Mg alloys have focused on the stent application and controlling of mechanical loading, fluid composition and CO_2 concentration (Wang, Giridharan et al. 2014). Studies to observe the change in corrosion within a bioreactor, effect of released metallic ions from Mg alloy, change of pH level, and release of hydrogen gas upon bone cells seeded in perfusion bioreactor is still lacking.

In this chapter, Mg5Ca1Zn samples were implanted on porous hydroxyapatite scaffold and press-fitted to a perfusion chamber to investigate the direct effect of magnesium degradation on osteoblast cells in an *in vivo* simulated environment. It aims to provide a systematic understanding of bone cell-magnesium alloy interaction under a flow-induced loading condition including corrosion profile, corrosion rate,

observation of bone formation markers, osteoblast proliferation and differentiation. Results are then compared to corrosion resistant titanium and fast corroding Mg5Ca alloy to show the benefit of newly developed Mg5Ca1Zn alloy.

4.2 Materials and Methods

4.2.1 Perfusion bioreactor for 3D cell culture

The hydroxyapatite (HA, Engiopore, Finceramica-Faenza) in the form of porous cylinders of 4 mm height and 8 mm diameter were used as scaffold material. The porosity of HA scaffolds were 83 ± 3% and the pore size distribution was 22% for <100 µm; 32% for 100–200 µm; 40% for 200–500 µm; and 6% for >500 µm. HAs were implanted with test specimen (titanium, Mg5Ca, or Mg5Ca1Zn) and placed in the bioreactor chamber (U-CUP, Cellec Biotek AG), allowing controlled flow of a culture medium directly through the HA using a syringe pump. The size of the test specimens were 1 mm in diameter and 2 mm in length. The perfusion-based bioreactor was placed inside an incubator, and the perfused systems were prolonged up to 4 weeks.



Figure 4.1 U-Cup direct perfusion bioreactor installed in incubator (adapted from Cellec Biotek AG).

4.2.2 Micro-computed tomographic analysis

Hydroxyapatite scaffolds implanted with Mg5Ca1Zn alloys were perfused with for four weeks at a speed of 0.3 ml/min with Ham's F12 Medium and Dulbecco's Modified Eagle's Medium, supplemented with 10% fetal bovine serum and 1% penicillin streptomycin. Perfused samples were then scanned using Skyscan Micro CT 1172 (Bruker, USA) equipment. The long axis of the sample was aligned perpendicularly to the axis of the X-ray beam and the scanned images were used to evaluate the degradation profile of Mg alloy in perfusion bioreactor.

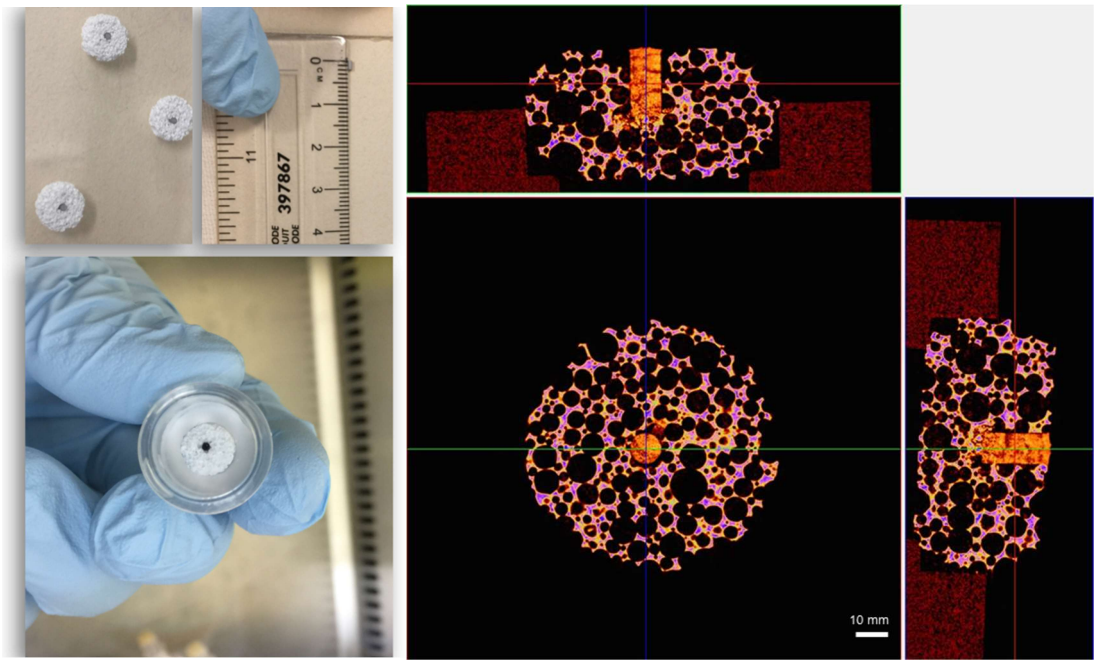


Figure 4.2 HA scaffolds implanted with Mg5Ca1Zn sample (1 mm in diameter and 2 mm in length) and μCT image of the implanted sample in the HA scaffold.

4.2.3 Molecular diffusivity experiment simulation

Hydroxyapatite scaffolds were scanned using Carl Zeiss Xradia 510 Versa (Zeiss, Germany) which allows sub-100 nm resolutions at X-ray source voltage of 60 kV and current set of 83 mA. Two scans were performed per sample and processed images were segmented and analysed using Avizo 3D analysis program. The molecular diffusivity experiment simulation (Demo module) was used to simulate the media flow throughout HA scaffold.

4.2.4 Cell culture

Human fetal osteoblast (hFOB 1.19) was purchased from American Type Culture Collection. The growth medium used for osteoblasts was a 1:1 mixture of Ham's F12 Medium and Dulbecco's Modified Eagle's Medium, supplemented with 10% fetal bovine serum and 1% penicillin streptomycin. Cells were cultured in incubator at temperature of 34 °C, 95% humidity and 5% CO_2. For osteogenic differentiation, osteoblasts were maintained at 37 °C in the osteogenic growth medium with 50 µg/ml Ascorbic acid, 10 mM β-glycerophosphate and 100 nM Dexamethasone. Cells (2 x 10^6) suspended in 1 ml of media were seeded on hydroxyapatite in the perfusion chamber and the final volume of media in reactor was 9 ml. Cells were cultured in the chamber at perfusion rate of 0.3 ml/min and the media was changed every 3 days

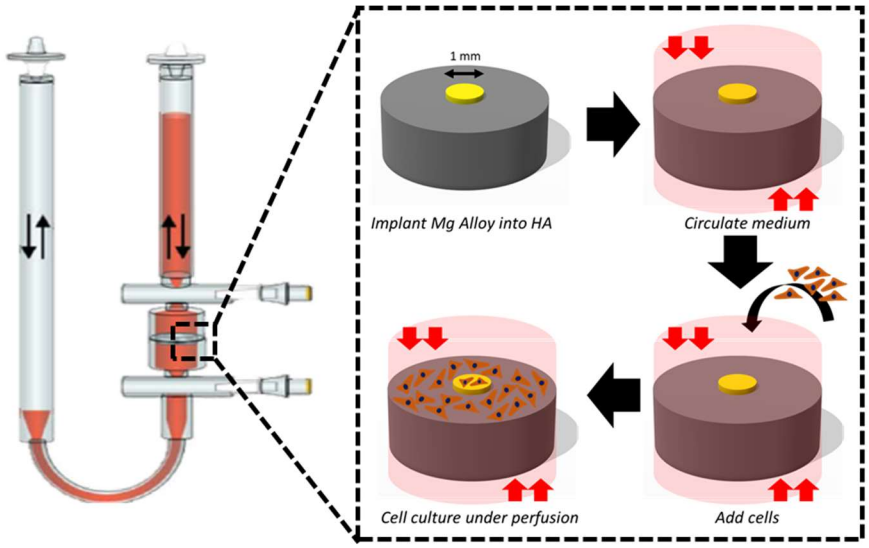


Figure 4.3 Schematic of 3D cell culture process. HA scaffold implanted with Mg alloy sample is placed in the chamber of perfusion bioreactor and medium is circulated through the chamber. hFOB 1.19 Cells (2x10^6) are seeded on top of the HA scaffold and then cultured under perfusion.

4.2.5 Adhesion of osteoblasts on Hydroxyapatite (HA)

For the cell adhesion study, cells (1 x 10^{6} cells/HA) were seeded and cultured throughout the HA at perfusion-based bioreactor system at a speed of 100 μm/sec. Cells on HA were fixed with 4% paraformaldehyde and permeabilized in cytoskeleton buffer (0.5% Triton X-100). Following permeabilization, the HAs were blocked by incubating with 2% fetal bovine serum and 0.1% Tween-20 in PBS and then sequentially incubated with rhodamine-phalloidin and 4′,6-diamidino-2-phenylindole (DAPI), respectively.

4.2.6 Immunofluorescence staining for Cleaved Caspase-3 as an apoptosis marker

To obtain quantitative level of apoptosis of cells on HA, cells were seeded with densities of 1 x 10^{6} cells on HA and cultured in growth medium for 24 h. Cells on the HAs were stained for Cleaved Caspase-3, which was visualized using confocal Microscopy (LSM700). Cells on HA were fixed with 4% paraformaldehyde blocked by incubating with 2% fetal bovine serum and 0.1% Tween-20 in PBS and then sequentially incubated with Anti-Cleaved Caspase-3 (1:100).

4.2.7 Fluorescence-activated cell sorting for cell proliferation

To evaluate proliferation at designated time point (24 h), osteoblasts were incubated with 10 μM 5-ethynyl-2-deoxyuridine (EdU) in growth medium for 2 h, then sequentially trypsinized and washed. Fixation (4% paraformaldehyde for 15 min), saponin-based permeabilization and the Click-It reaction for AlexaFluor488 labelling were performed using the Click-iT EdU Alexa Fluor 488 Flow Cytometry Assay Kit (Life Technologies). Cells were resuspended with saponin-based permeabilization solution and analysed on a BD Fortessa (BD Bioscience)

To measure the DNA content at designated time points (1,3 5 days under growth medium), osteoblasts cultured HA (n=3) were lysed in RIPA lysis buffer (Santa Cruz Biotechnology). The DNA contents were measured using Quant-iT PicoGreen dsDNA Assay Kit (Thermo Fisher Scientific) and a spectrofluorometer (FLUOstar Omega , BMG Labtech) at excitation and emission wavelengths of 480 nm and 520 nm, respectively.

4.2.8 Second harmonic generation (SHG)

SHG imaging was performed using a dedicated two-photon confocal microscope. Samples were imaged using a Zeiss Examiner Z1 two-photon excitation laser scanning confocal microscope (Carl Zeiss, Jena, Germany) coupled to a Coherent Chameleon titanium:sapphire laser (Coherent, Glasgow, UK). The images show the collagen visualized via SHG and multiphoton Microscopy (excitation wavelength 840 nm).

4.2.9 Assaying the levels of differentiated osteoblasts

Osteogenic differentiation of cells on HA was determined by Collagen type I (Col I), Alkaline phosphate (ALP), osteocalcin (OCN) and osteopontin (OPN) production by ELISA kits. Briefly, cells were seeded with densities of 1 x 10^6 cells on HA and cultured in growth medium for 24 h. After 24 h, medium was replaced by osteogenic differentiation medium. At each time point, cells were lysed using RIPA lysis buffer with protease inhibitor added. The buffer was then collected from the samples and centrifuged at 10,000 g for 10 min. The supernatant was collected and used for the ELISA tests. The level of collagen synthesis, ALP production, secretion of OCN and OPN were analysed using a Collagen Type I (NOVOS), ALP (Abcam), OCN (Invitrogen) and OPN (eBioscince) enzyme-linked immunosorbent assay (ELISA) kit, respectively, according to the manufacture's instruction. The protein concentration was measured using a microBCA assay. All osteogenic differentiation activities were normalized to protein concentration of the cell lysate.

4.2.10 Live computer tomography of rat femoral condyle

The progress of implant degradation in femoral condyle of SD rat was tracked with *in vivo* live μCT using Somatom sensation 16 (Siemens, Germany). Before scanning, the rats were anesthetized using injection of a mixture of zoletil (10 mg/kg; Virbac SA) and xylazine (5 mg/kg; Bayer Korea) at 2:1 ratio. Following anaesthesia, the SD

rat were placed within the scanner and the femoral condyles were scanned with a tube current of 0.45 mA and an x-ray tube potential of 80 kVp.

4.3 Results and Discussion

4.3.1 Flow-induced corrosion of Magnesium alloy implanted on hydroxyapatite scaffold inside the perfusion bioreactor

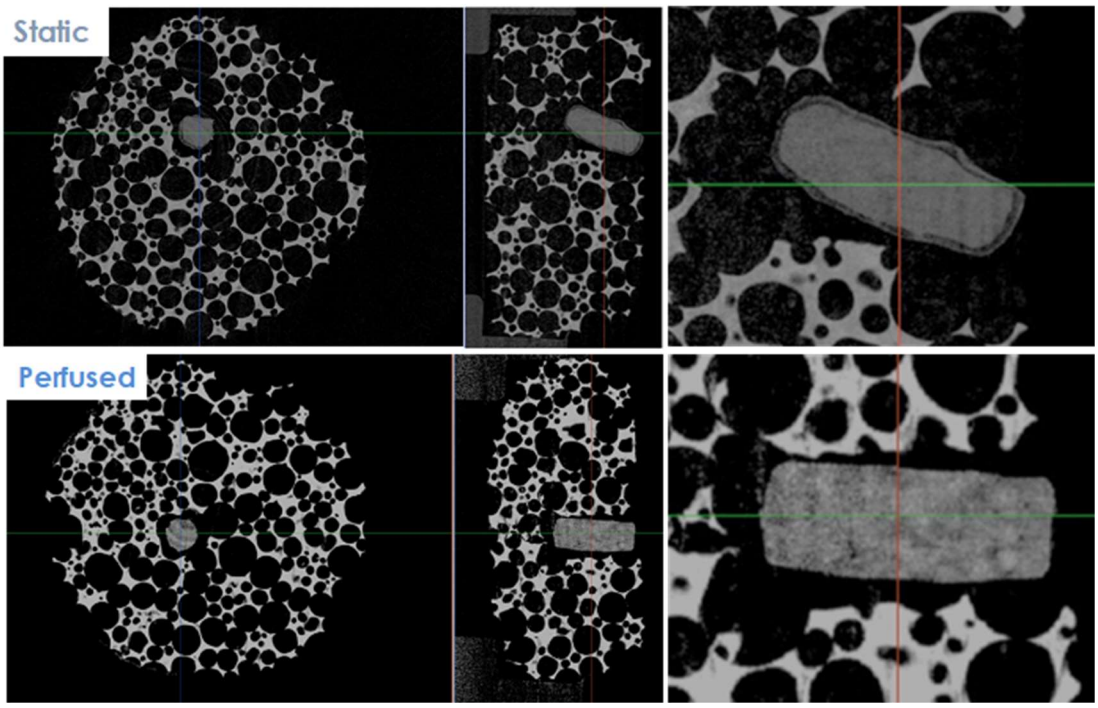


Figure 4.4 µCT comparison of Mg5Ca1Zn samples immersed in static conditions with a thick layer of corrosion by-product on the surface of Mg and perfusion condition without accumulation of corrosion by-product on the surface after 4 weeks.

Based on the corrosion profile comparison between static and perfused conditions (Fig. 4.4), the direct perfusion system had an immense effect on the overall corrosion mechanism of the Mg alloy implanted on HA scaffolds. A layer of deposited corrosion by-product on the surface of sample immersed in static conditions was

observed while uniform corrosion with relatively flat regions were shown for the samples in perfusion conditions. In general, the corrosion of Mg alloy results in the deposit of a corrosion product layer. Similar results have been demonstrated in other studies, which showed the faster removal of the corrosion product by the flow of medium.

As mentioned in Chapter 1, the inner layer of the Mg corrosion product mainly consists of magnesium oxide (Mg and O) whereas the outer layer composes of calcium phosphate (Ca and P). During the initial phase of corrosion, released Mg ions react with OH from cathode sites to form the magnesium oxide layer. The increase of local pH follows and causes the calcium phosphate precipitation on the surface of the corroding magnesium. The corrosion of Mg depends heavily on the pH level and the conventional static condition without the flow would create a high local pH level near the sample to provide a favourable environment for the magnesium oxide formation and calcium phosphate precipitation (Witte, Kaese et al. 2005). However, this does not reflect the *in vivo* environment of human and animal bones where active blood flow occurs constantly at rates ranging from 5 to 20 ml/min/100 g (Laroche 2002) and where blood flow in the fractured tibia was shown to be 3 to 6 times higher than a normal tibia after 24 hours of injury (Tomlinson and Silva 2013).

In Fig. 4.4, the samples from perfused conditions show a lack of such corrosion by-product layer which can be attributed to the flow-induced loading from the perfused media. In addition to the prevention of calcium phosphate precipitation by the mechanical loading, flowing medium leads to faster ion diffusion and prevents the increase of local pH level. Calcium phosphate is known to deposit faster in slow

diffusing alkaline environment and such precipitation was almost completely inhibited in perfused conditions (Dorozhkin and Epple 2002). This result is also consistent with findings from other studies (Li, Song et al. 2014, Wang, Jang et al. 2016).

As shown in Fig. 4.5, a similar corrosion profile was observed from the live μCT scan of SD rats implanted with the same Mg alloy at 4 weeks post-operation. These similarities in corrosion profile confirm the close simulation of an *in vivo*-like environment and support the reliability of the perfused 3D cell culture system.

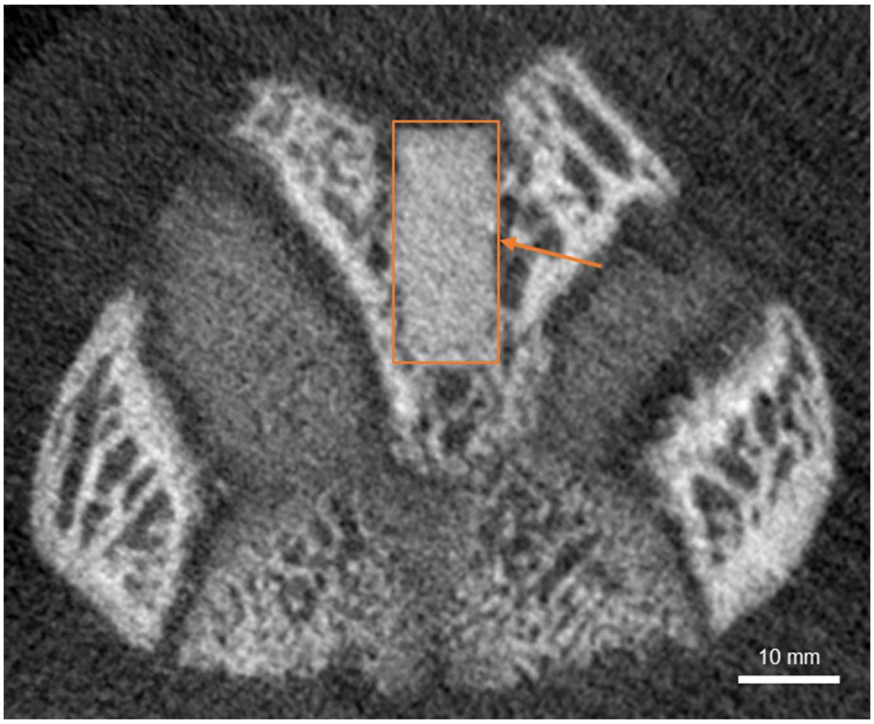


Figure 4.5 4 weeks post-operation in vivo CT of femoral condyle of SD rat implanted with Mg5Ca1Zn. Orange line indicate original shape of the implant sample.

Furthermore, the use of a perfusion bioreactor significantly increased the cell penetration through the HA scaffold as shown in Fig 4.6. The hFOB 1.19 cells did not migrate down to the empty defect site created in HA after 1 day of culture. In contrast, confocal Z stack images showed the migrated hFOB 1.19 cells penetrating the empty defect site of HA in the perfusion conditions after 1 day of culture.

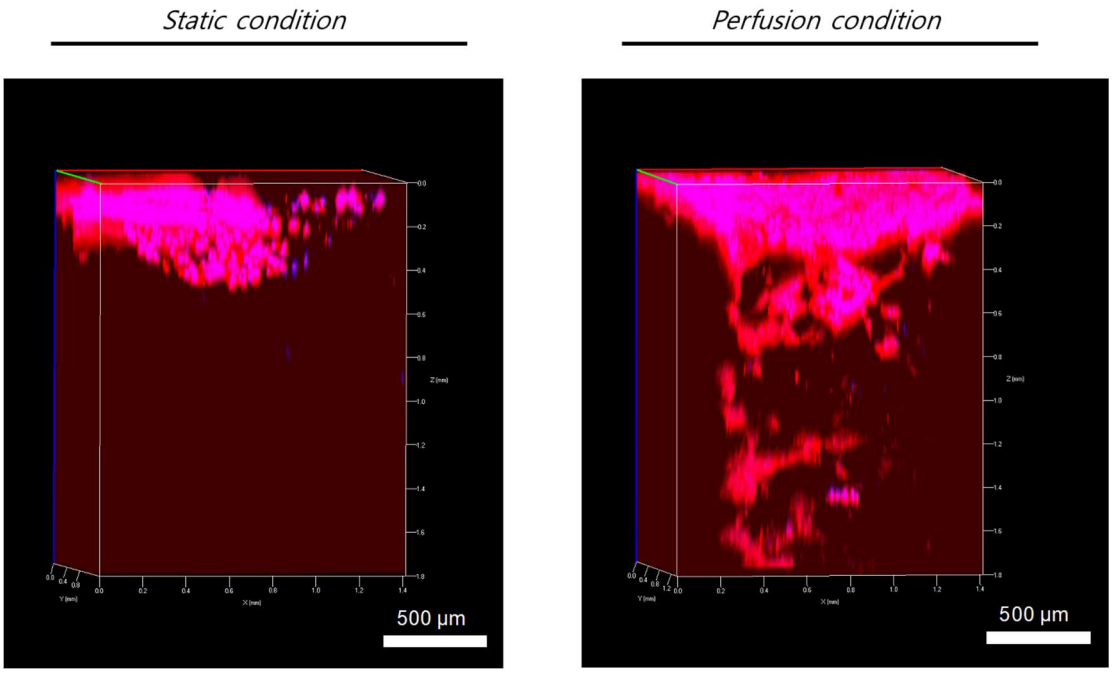


Figure 4.6 Confocal Z stack image showing human fetal osteoblastic cell proliferation and penetration through 1mm wide and 2 mm deep defect made on HA scaffold under static and perfusion condition after 1 day of culture.

Such 3D cell culture techniques facilitate cell penetration into the pores of the scaffold material and delivery of oxygen and nutrients throughout the scaffold, which is nearly impossible to model in static culture system. The exposure to fluid shear stress has been known to enhance the bone formation ability of osteoblastic cells *in*

vivo and previous studies have shown enhanced viability, proliferation and differentiation of osteoblast cells cultured in 3D perfusion conditions when compared to conventional 2D static culture conditions (Vandrovcova and Bacakova 2011). The simulation of media flow through the HA scaffold using Avizo software from Xradia 810 confirmed the pore connectivity and open porous structure of HA used in this study (Fig. 4.7).

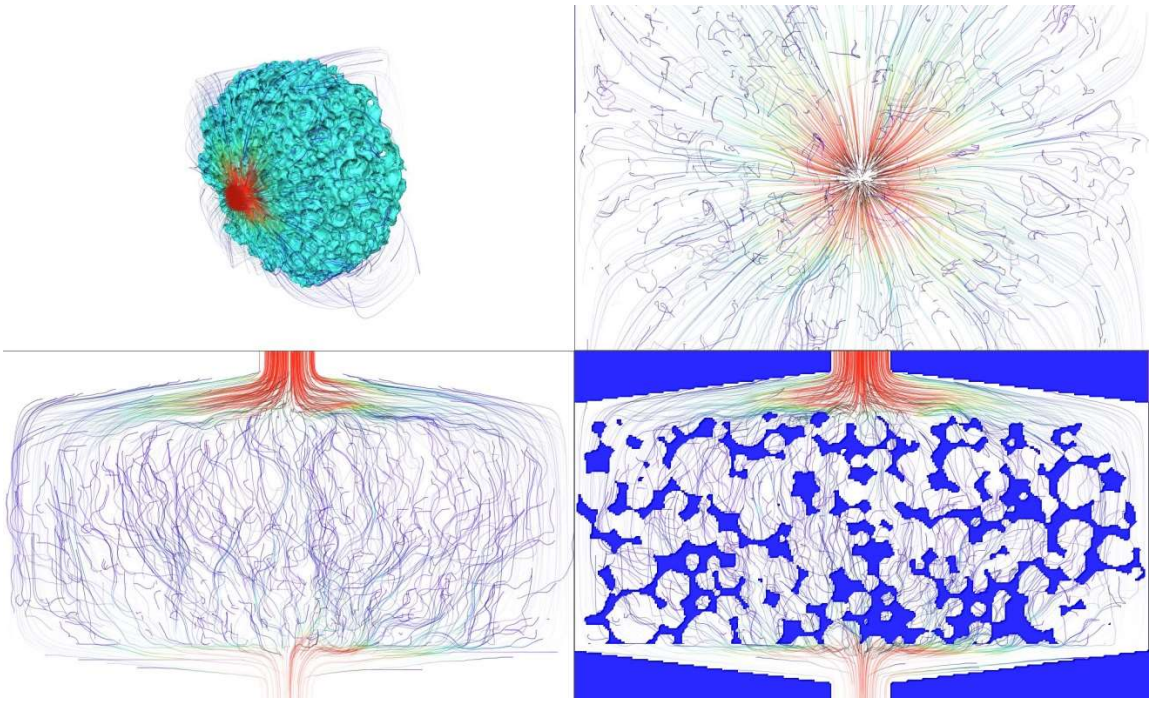


Figure 4.7 Water molecular diffusivity simulation showing the flow of media through the open porous structure of hydroxyapatite scaffold.

4.3.2 *In vitro* cellular response to flow induced loading and biodegradation of Mg alloy

To investigate the bioactivity of metal alloys, the attachment of hFOBs for both static and dynamic flow conditions were observed microscopically after 24 hours of culture. As shown Fig. 4.8, cells on Titanium and Mg5Ca1Zn were well attached to the surface when compared to that of Mg5Ca. The corrosion rate of the Mg5Ca alloy is roughly 20 times faster than the Mg5Ca1Zn alloy and such rapid corrosion rate seems to prevent the attachment of cells on the surface of Mg5Ca. It showed slightly higher number of attached cells for dynamic perfused conditions for Mg5Ca but the synergistic effect of a dynamic condition on cell adhesion was not observed for Titanium and Mg5Ca1Zn.

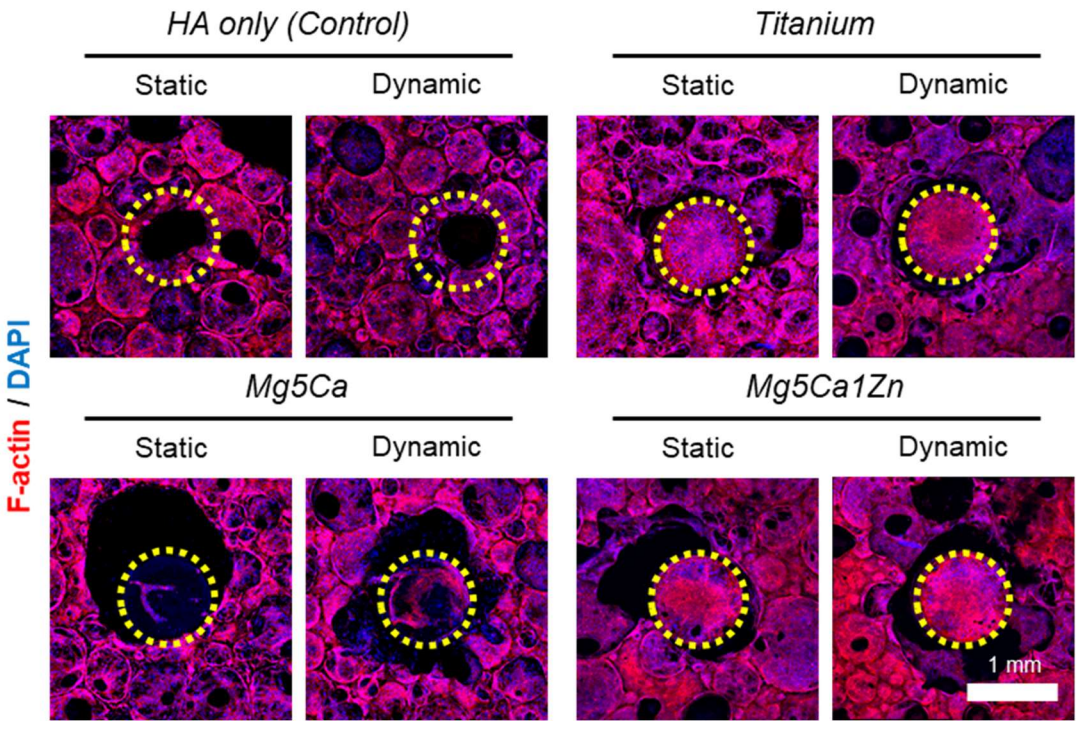


Figure 4.8 Cytoskeletal structures hFOBs after 24 h of culture on the HA, Mg-based alloy implanted HA and titanium implanted HA. The images were acquired by fluorescence staining for F-actin (red), and DAPI (nuclei)

As shown in Fig. 4.9, the results from FACS quantified using FCS Express 6 Flow Cytometry Software showed no significant difference in hFOBs proliferation between tested groups for 2D static conditions except in the Mg5Ca group after 24 hours of culture. As mentioned before, this is largely due to the fast corrosion rate of the Mg5Ca. There was a significant difference in proliferation for the materials cultured in 3D dynamic conditions when they were compared to the same material cultured in 2D static conditions. For example, BrdU intensity values of cells in 2D static condition were 34.54%, 35.55%, 29.31% and 36.28% for Control, Titanium, Mg5Ca and Mg5Ca1Zn, respectively. However, a drastic increase was observed in BrdU intensity values of cells in 3D dynamic conditions were 46.99%, 47.88%, 34.17% and 46.93% for Control, Titanium, Mg5Ca and Mg5Ca1Zn, respectively.

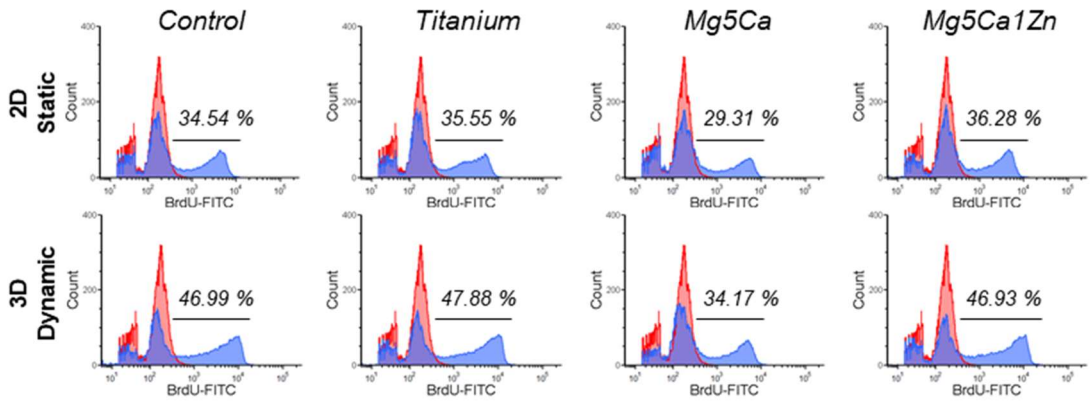


Figure 4.9 FACS results of hFOB proliferation after 24 h of culture under static and dynamic conditions using control HA, HA implanted Titanium and HA implanted with two different type of Mg-based alloys. The intensity value of BrdU from each sample was measured for comparison.

To determine the level of apoptosis occurring from the degradation of metal alloys, immunofluorescence staining was performed for the marker of mid-stage apoptosis cleaved caspase 3 (CC3). Representative images from each culture conditions are shown in Fig. 4.10. As expected, a significant increase in apoptosis was observed for the Mg5Ca group when compared to the other groups. For the static culture condition, the value of Cleaved Caspase-3 positive cells were 81.67 ± 7.58, 18.96 ± 3.28, 30.39 ± 4.91 and 33.43 ± 6.27 for Mg5Ca, Control, Titanium and Mg5Ca1Zn, respectively. Although there were no statistically significant differences between the culture conditions (static or dynamic culture condition), slightly lower non-significant value of Cleaved Caspase-3 positive cells were observed for materials in dynamic culture condition than the static condition.

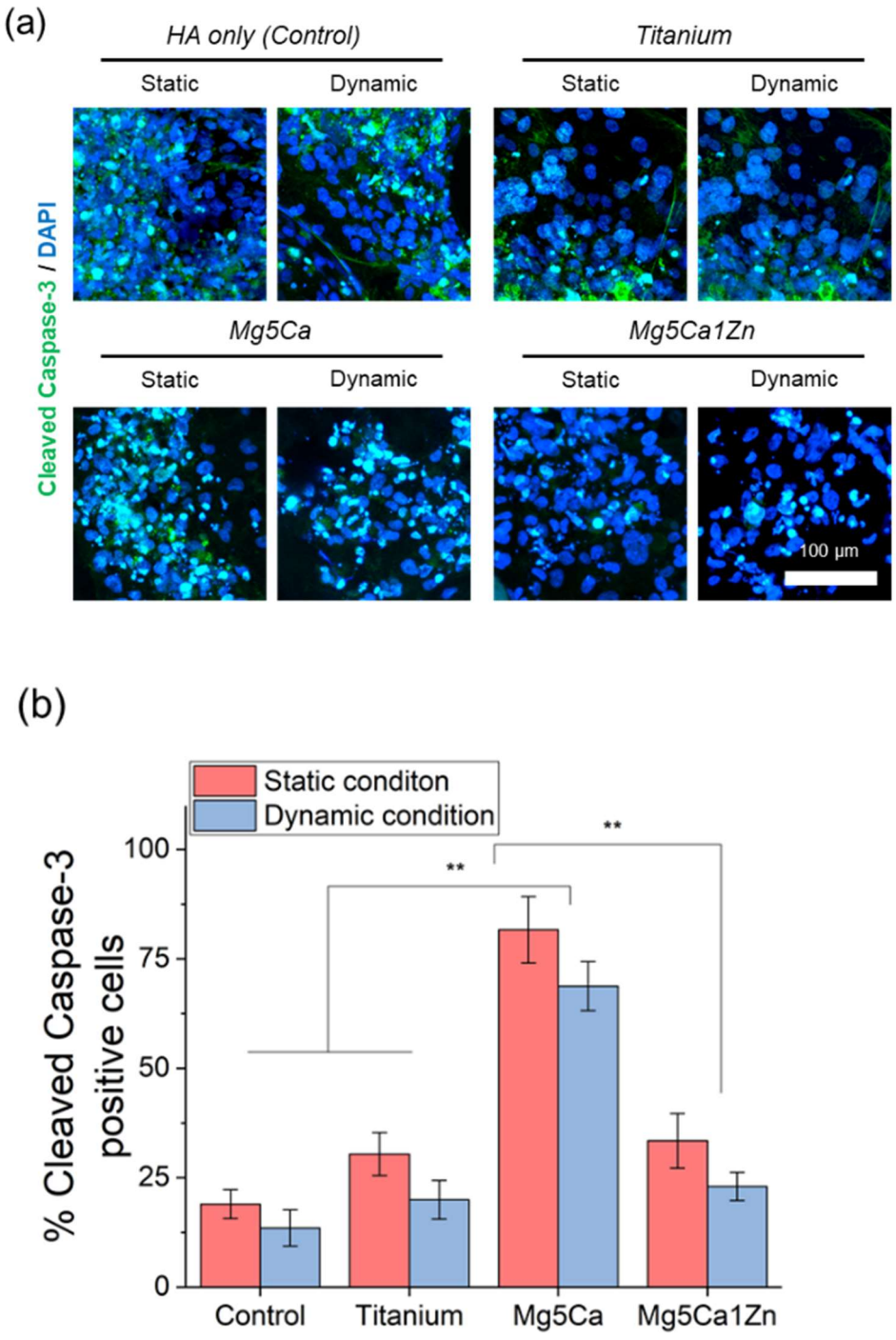


*Figure 4.10 Analysis of apoptosis by Cleaved Caspase-3 staining (a) representative images of hFOBs stained for Cleaved Caspase-3. (b) Quantification of Cleaved Caspase-3 positive cells. ** indicates significant difference ($p < 0.05$).*

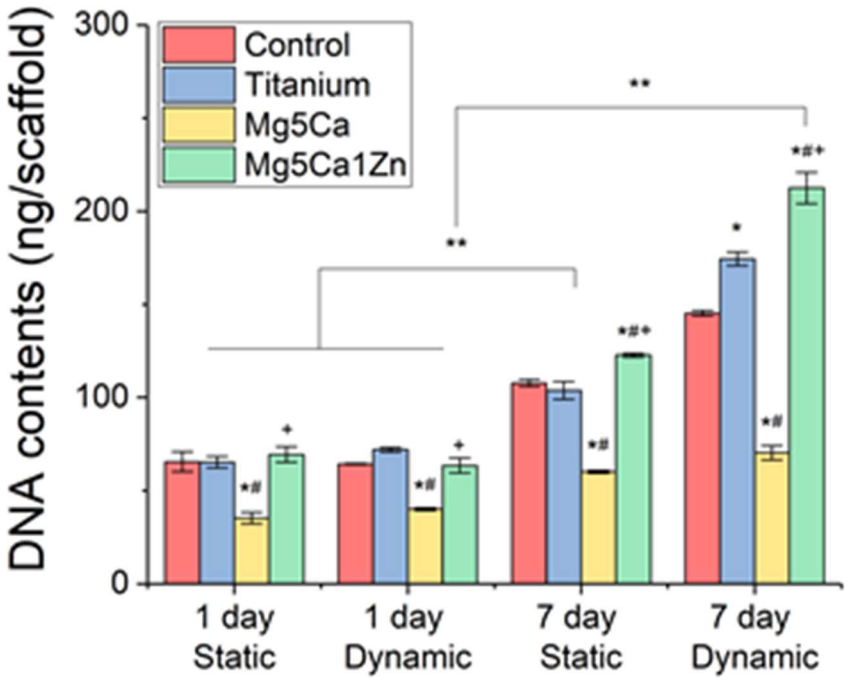


Figure 4.11 Quantification of DNA contents. "", "#", and "+" indicate significant differences compared to Control, Titanium and Mg5Ca, respectively ($p < 0.05$). ** indicates significant difference ($p < 0.05$).*

The proliferation of hFOBs were further analysed by culturing for 7 days and quantifying DNA contents (Fig. 4.11). The results showed no significant difference between total DNA content for tested materials in both culture conditions at the initial time point (1 day). The absorbance values at 1 day of culture were 65.50 ± 5.35, 65.24 ± 3.02 and 69.42 ± 4.17 for Control, Titanium and Mg5Ca1Zn in static culture condition and 64.30 ± 0.26, 71.99 ± 1.32 and 63.49 ± 4.04 for Control, Titanium and Mg5Ca1Zn in dynamic culture condition. However, cells cultured in dynamic conditions started to show a statistically higher quantity of DNA at 7 day of culture

for Control, Titanium and Mg5Ca1Zn, likely due to effects of 3D perfusion bioreactor mentioned earlier. Interestingly, cells cultured on Mg5Ca1Zn in dynamic condition for 7 days showed a significantly higher expression of DNA contents when compared with static culture conditions; 212.49 ± 8.34 and 122.73 ± 1.17 in dynamic culture condition and static culture condition, respectively. It was also statistically significant when compared to control HA and HA implanted with titanium. Such results indicate that the released metallic ions from the magnesium alloy have beneficial effects on proliferation of osteoblasts which is in agreement with the findings from Chapter 3. The cells seeded on Mg5Ca showed a dramatically decreased DNA content regardless of culture conditions. DNA contents of Mg5Ca were 35.29 ± 3.05 and 40.09 ± 0.75 in static culture condition and dynamic culture condition, respectively.

Second-harmonic generation (SHG) enables observation of collagen structure without requiring staining procedures. Immunohistological staining of tissue sections containing magnesium alloy often results in complications due to reactive magnesium. Hydrogen gas formation from the magnesium alloy immersed in dye solution damages the tissue and hinders accurate observation of the result. These limitations are avoided with the use of SHG allowing for the fibrillar collagen expression of the cells on the surface of the metal alloys to be observed. As shown Fig. 4.12, the results showed that the expression level of fibrillar collagen was higher in dynamic culture conditions for all of the tested materials. Among them, the expression level of collagen on Mg5Ca1Zn alloy was the highest. Consistent with SHG results, the level of Collagen I expressed by hFOBs were greater for Mg5Ca1Zn when compared to those on Titanium and Mg5Ca alloy; the expression of Collagen I

at 7 days in static culture conditions were 88.01 ± 4.69, 54.86 ± 5.01 and 1.91 ± 1.03 for Mg5Ca1Zn, Titanium and Mg5Ca, respectively. In addition, the amount of Collagen I expression was higher in the dynamic culture condition than in the static culture condition.

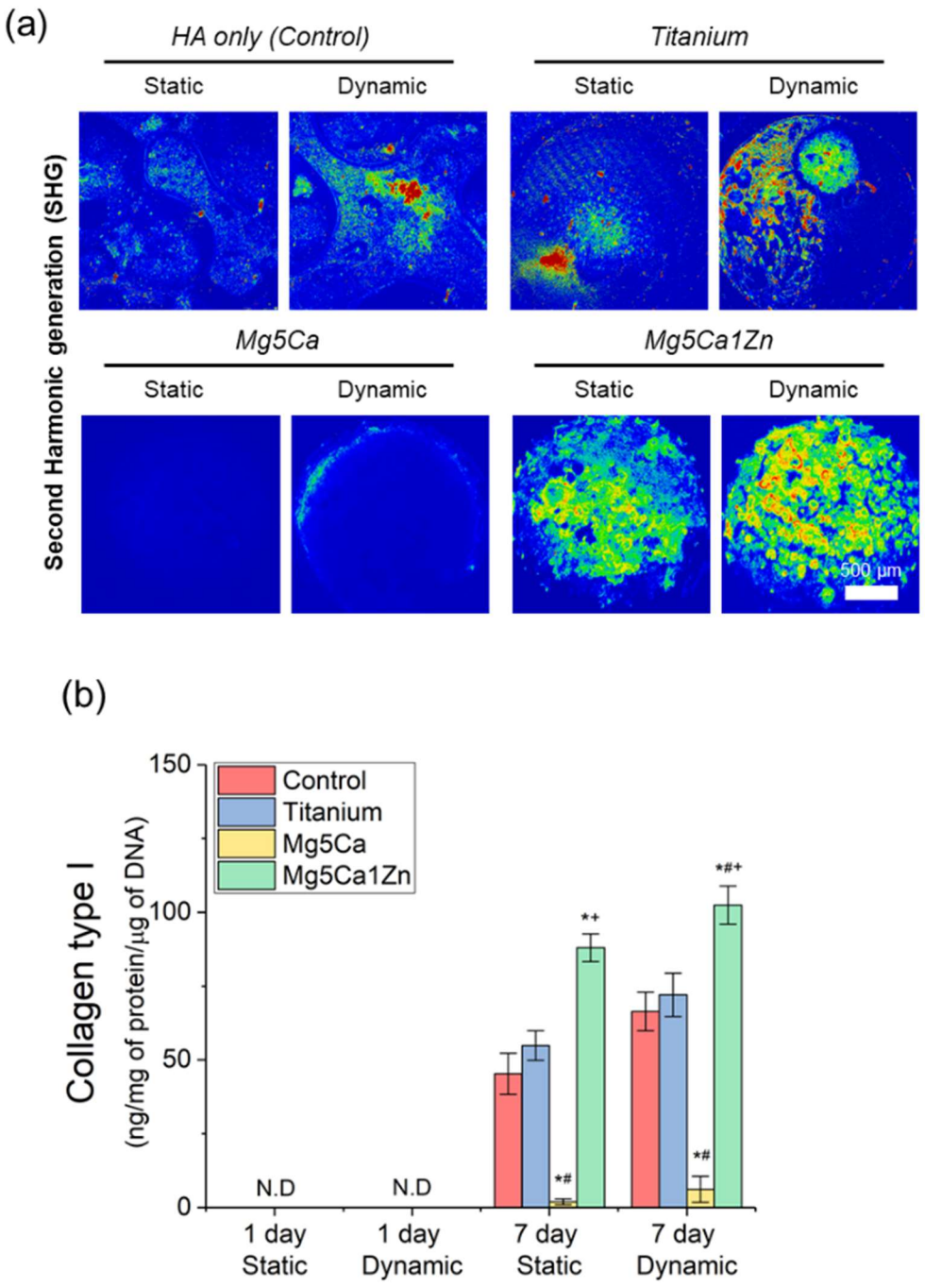


Figure 4.12 (a) Second harmonic generation (SHG) imaging of cells on metal alloy. (b) ELISA analysis of the Collagen I content of cells on metal alloy. "", "#", and "+" indicate significant differences compared to Control, Titanium and Mg5Ca, respectively ($p < 0.05$).*

Lastly, hFOBs on metal alloys were tested for osteogenic differentiation using ELISA. Active markers of osteogenesis were assessed to determine the effect of metal alloys cultured on different conditions during the bone formation process. These markers included ALP, which makes phosphate available for calcification, Osteocalcin (OCN), which is a noncollagenous protein hormone in bone, and Osteopontin (OPN), which anchors bone cells to the mineralized bone surface. The results showed that there was a significant difference in osteogenic differentiation level between the static and dynamic culture conditions. ALP activity on Mg5Ca1Zn at 14 days was 51.63 ± 1.24 and 63.73 ±0.32 μmol/min/ml/ug of protein/ng of DNA in static and dynamic culture condition, respectively. Analysis of OCN and OPN expression also showed a similar trend as ALP expression to validate the results from the previous chapter. Interestingly, cells on Mg5Ca showed a significantly lower expression of OPN (ng/mg of protein/mg of DNA) in static culture condition compare to that in dynamic culture condition at 14 days; 8.23 ± 3.41 and 54.45 ± 2.77 for static and dynamic culture condition, respectively. The higher expression of proteins observed from Mg5Ca after 14 days of culture in dynamic condition could be related to the higher amount of released metallic ions in the media. Due to the fast corrosion rate, the total number of DNA contents were significantly lower for Mg5Ca. However, when the expressions of proteins were divided by the total number of DNA, the normalized protein expression value was significantly higher at day 14 for Mg5Ca compared to control and titanium. This result indicates that fast corrosion of the Mg5Ca reduces the rate of hFOB cell attachment and proliferation, but the increased amount of release metallic ions from the Mg5Ca to result in relatively higher number of active markers of osteogenesis. In addition, there was no statistical difference between control (HA only) and the bioinert Titanium group; at day 14 in dynamic culture conditions, it was 2.41 ± 0.04 and 2.48 ± 0.15 of OCN expression (ng/mg of protein/ng of DNA) for Control and Titanium, respectively. The general trend of osteogenic bone marker expression confirmed the benefits of 3D dynamic culture system and showed the positive effect of released metallic ions from Mg5Ca1Zn alloy on osteoblast differentiation.

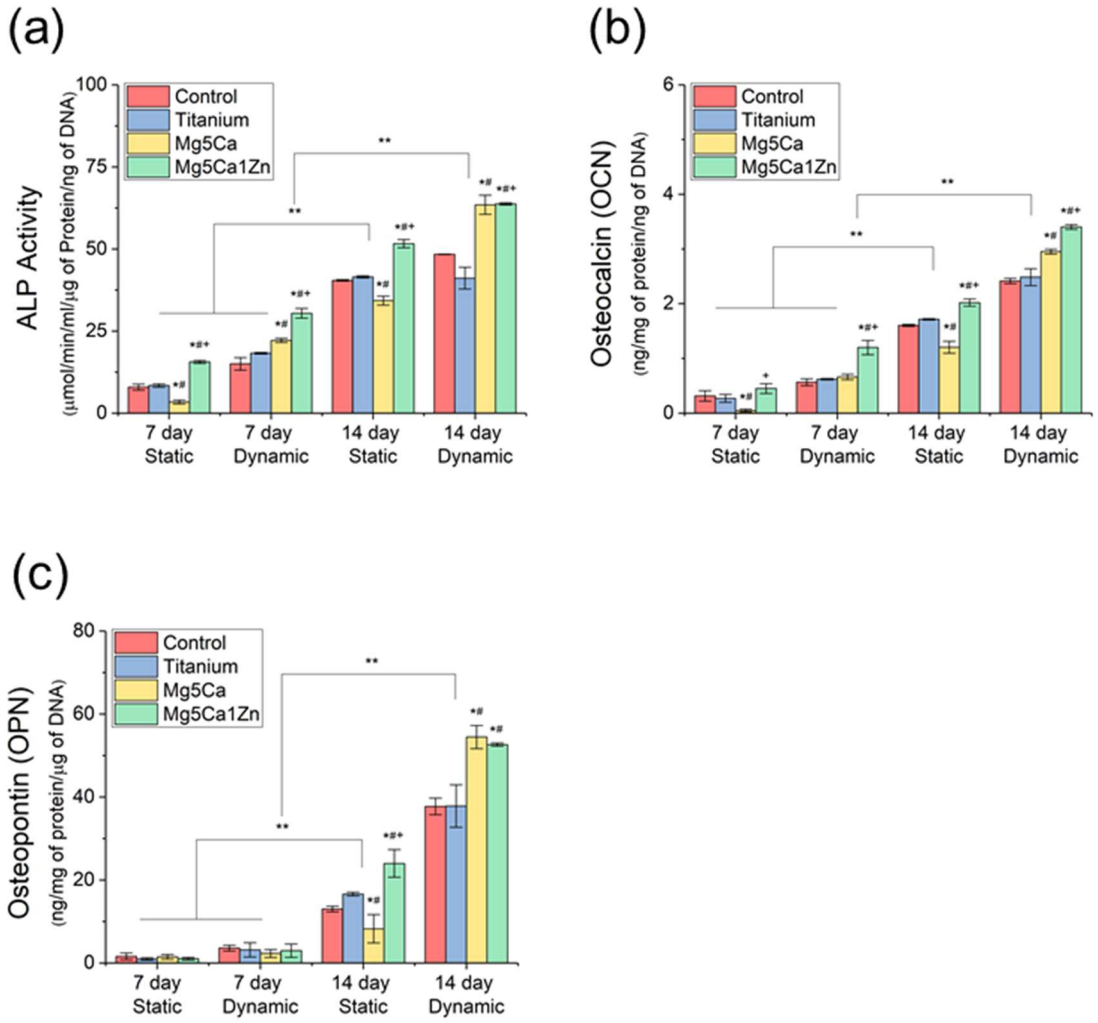


Figure 4.13 Quantification of production of (a) ALP, (b) OCN and (c) OPN bone protein. "", "#", and "+" indicate significant differences compared to Control, Titanium and Mg5Ca, respectively ($p < 0.05$). ** indicates significant difference ($p < 0.05$)*

4.4 Conclusion

In this chapter, the benefit of a 3D dynamic culture system was validated and the osteogenic effect of released metallic ions from Mg5Ca1Zn evaluated. The *in vivo*-like environment modelling flow-induced loading resulted in a statistically significant increase in proliferation and differentiation of osteoblasts in all of the tested materials. A series of comprehensive evaluations of released ions from Mg5Ca and Mg5Ca1Zn alloy showed the effect of Mg alloy biodegradation on the human fetal osteoblast cells. Fast corroding Mg5Ca showed detrimental effects on osteoblast cells whereas the overall process involved in osteoblast proliferation and differentiation was improved by the release of metal ions from the Mg5Ca1Zn alloy with slower corrosion rates. These findings suggest that the release of metal ions consisting of Mg, Ca and Zn also sufficiently stimulate the proliferation and differentiation of osteoblast cells to facilitate the bone formation/healing process. Bioinert titanium did not show any improvement in bone formation over the control.

Chapter 5

Evaluation of angiogenesis and coupled osteogenesis from magnesium alloys

5.1 Introduction

The skeletal system consists of connective tissues and bones that enables dynamic movement and provides structural support for our body. It undergoes a constant remodelling process of formation and resorption over the lifetime. Mammals have two distinct types of bones that form in different ways (Sivaraj and Adams 2016). Flat bones, found in the pelvis, skull, sternum, and rib cage, protect the inner organs and provide spaces for the attachment of muscles. They are formed through the intramembranous ossification process which involves the accumulation of mesenchymal stem cells (MSCs) that differentiate directly into osteoblastic cells. These cells promote bone formation by creating an ossification center and releasing extracellular matrix. In contrast, long bones like femur and tibia are formed by the endochondral ossification process where MSCs differentiate into various types of cells including osteoblasts, osteoprogenitors and chondrocytes that facilitate bone

formation. These cells act as a template for the formation of new bone and bone marrow (Erlebacher, Filvaroff et al. 1995).

Recently, studies have found that both of these bone formation process are coupled with the formation of blood vessels (Kusumbe, Ramasamy et al. 2014). Pro-angiogenic factors like vascular endothelial growth factor (VEGF) are secreted from bone cells to trigger a series of responses from the other cell population with VEGF receptors such as chondrocytes, endothelial cells, osteoblasts, and osteoclasts (Maes, Goossens et al. 2010). Furthermore, bone endothelial cells have been found to release factors that promote the formation of chondrocytes and osteoblastic cells, and control the differentiation and maintenance of hematopoietic stem cells in the bone marrow (Trueta and Morgan 1960). In particular, angiogenesis has been shown to play a major role in the bone fracture healing process (Glowacki 1998, Maes, Kobayashi et al. 2010).

Most of the current studies on orthopaedic Mg alloy implants have been heavily focused on the osteogenesis aspect and have failed to look at the implication of coupled angiogenesis. In this chapter, state of the art fetal mouse metatarsal assay, second harmonic generation, and high-resolution 3D confocal imaging of vasculature within skeletal tissue will be systemically utilized to study the bone healing process of rat femurs implanted with Mg alloy implants. The roles of released metallic ions on the growth of blood vessels will be studied and confirmed by observation of both angiogenesis and osteogenesis at the bone healing site.

5.2 Preliminary *in vitro* angiogenesis assay

To confirm the effect of released metal particles on angiogenesis, a set of preliminary tests have been performed using conventional *in vitro* assays. Preliminary *in vitro* data are necessary for comparison with *ex vivo* fetal metatarsal assay and *in vivo* confocal microscopy results in latter portion of the chapter. In vitro preliminary study allows for evaluation of metallic ions at broader range of concentrations in controlled environment. The result from in vitro study was used to design and optimize *the ex vivo* and *in vivo* experiment by reducing the number of tested ion concentrations. An endothelial cell line, Human Umbilical Vein Endothelial Cells (HUVEC) (LONZA, Slough, UK) was grown in Endothelial Cell Growth Medium (EGM) kit in a humidified chamber with 5% CO_2 at 37°C. The remaining materials and methods are as described (Chapter 3) unless stated otherwise).

5.2.1 Cell viability

The LIVE/DEAD Viability/Cytotoxicity Kit for mammalian cells (Invitrogen, ThermoFisher Scientific, U.S) was employed to visualize the live (green) and dead (red) cells. As shown in Fig. 5.1, No significant cytotoxic effect was found at concentrations less than 10 mM Mg, 5 mM Ca and 100 μM Zn. When more than 50 mM Mg, 10 mM Ca and 500 μM Zn ions were added, a considerable number of round, dead cells (stained in red) were found. Similar to the results in chapter 3, the level of released metal ions collected from the extracts of pure Mg and Mg alloy over time were lower than the observed toxic level.

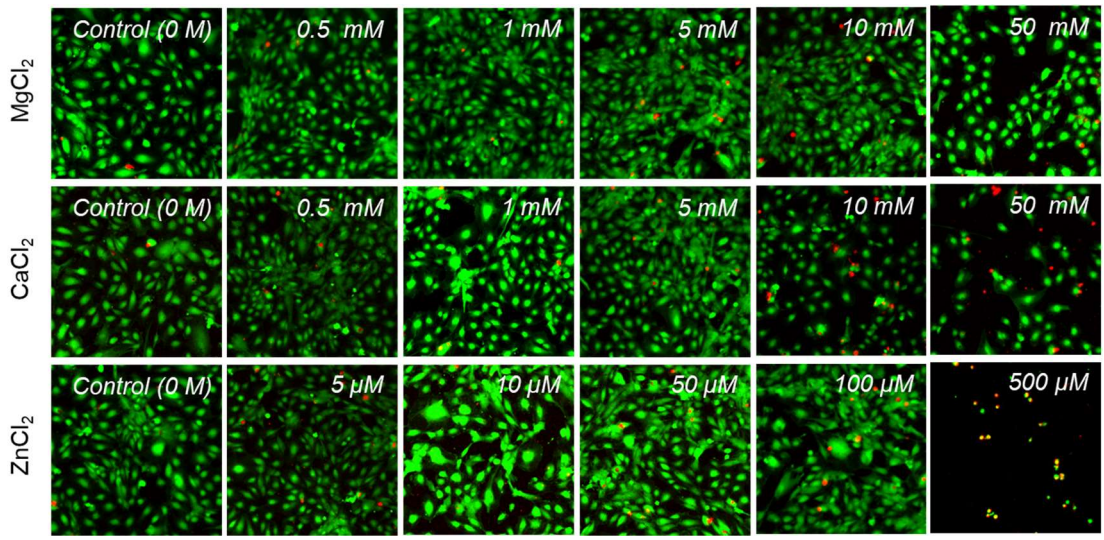


Figure 5.1 Live and dead staining of HUVEC depending on different concentration of Mg, Ca and Zn ions.

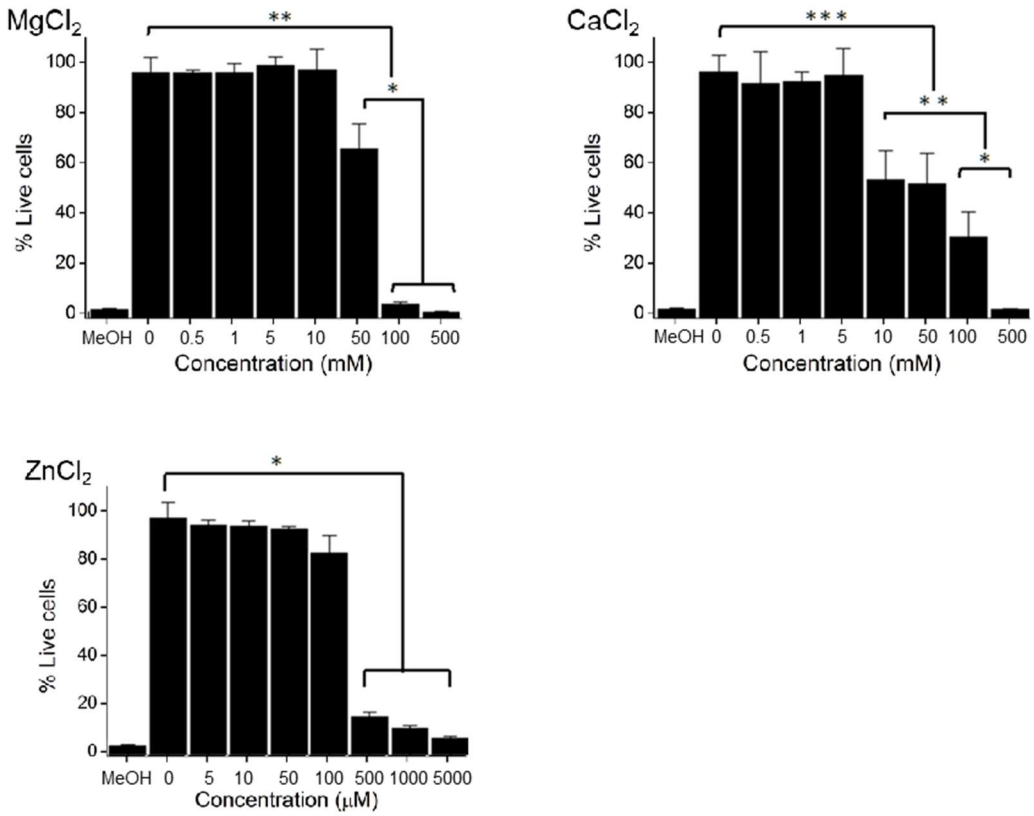


Figure 5.2 Cellular viability of HUVEC treated with increasing concentration of Mg, Ca and Zn ions. **p*<0.05, ***p*<0.01, ****p*<0.001

Decreased endothelial cell viability was observed for concentrations higher than 50 mM of Mg, 10 mM of Ca and 500 μM of Zn ions and there was no statistical differences between concentrations less than 10 mM of Mg, 5 mM of Ca and 100 μM of Zn when compared to the control groups with 0 mM of ions (Fig. 5.2). As mentioned before, the level of released metallic ions from the Mg5Ca1Zn alloy in culture media was around 1.5 mM of Mg ions and 0.6 μM of Zn per day which are both well under the toxicity level.

5.2.2 Endothelial cell proliferation

Cell proliferation was evaluated for 120 hr using a WST-1 based colorimetric assay (EZ-Cytotox Assay Kit, ITSBIO, Seoul, Korea).

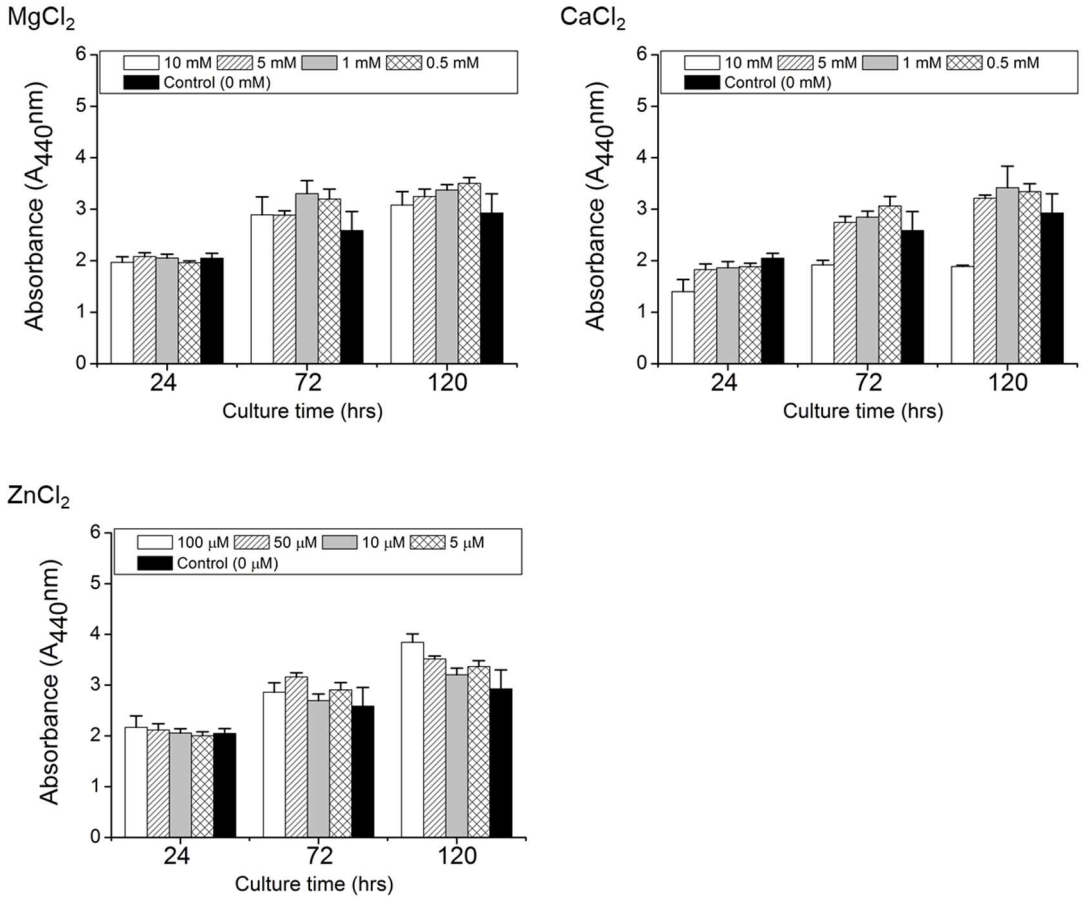


Figure 5.3 Proliferation of HUVEC treated with different concentration of Mg, Ca and Zn ions over time.

As shown in Fig. 5.3, there is a slight increase in proliferation of HUVEC after 120 hours when treated with increasing concentration of Mg ions, but it is not statistically significant. For example, at 120 hr, the absorbance values were 3.08 ± 0.25, 3.24 ± 0.14, 3.37 ±0 .10, 3.50 ± 0.11 and 2.92 ± 0.37 for the Mg ion treated at 10, 5, 1, 0.5 mM and control (0 mM), respectively. Cells treated with calcium ions showed decreased proliferation activity with increasing Ca ion concentration. Interestingly, HUVEC treated with increasing concentration of Zn ions showed increasing proliferation activity of HUVEC after 120 hours of culture.

5.2.3 Endothelial cell migration

The scratch assay is a well-established method to measure the migration of cells over time. Results of a scratch assay test on HUVEC at 0, 8, 16 hr post-injury time without treatment (control) and with Mg ion treatment is shown in Fig. 5.4.

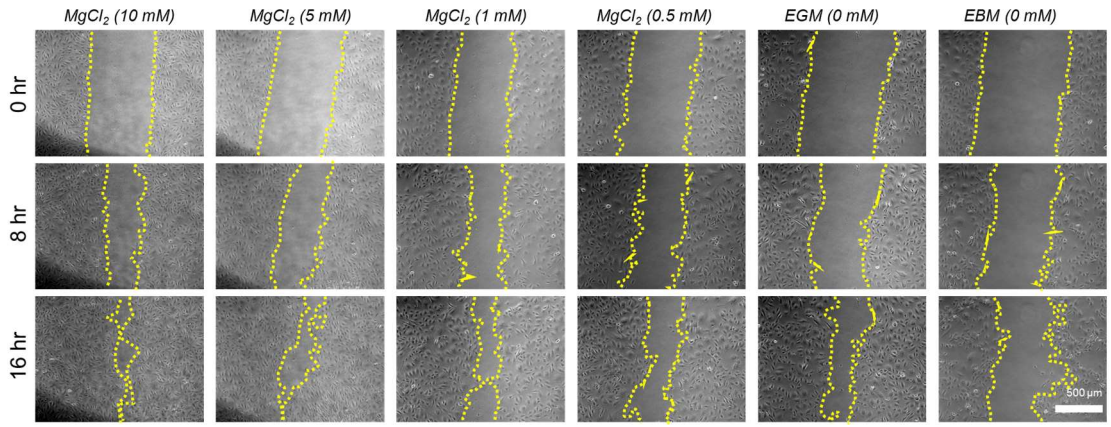


Figure 5.4 Scratch assay test on HUVEC treated with Mg ions at 0, 8, 16 hr post-injury.

Cell migration was observed over time as the wound from the scratch is closed by the migration and proliferation of HUVEC. As expected, enhanced migration and wound closure were observed for untreated endothelial growth medium (EGM) which was used as positive control. Endothelial basal medium (EBM) was used as negative control to show the slower rate of cell migration and cell proliferation. Faster cell migration and wound closure rate of Mg treated cells were observed for concentrations higher than 1 mM when compared to the positive control group. Similar to the results from proliferation assays, the HUVEC migration was decreased or inhibited in the presence of Ca ions when compared to the positive control after 16 hours (Fig. 5.5). The results from scratch assays of HUVEC treated with 10 mM resembled that of negative control.

.

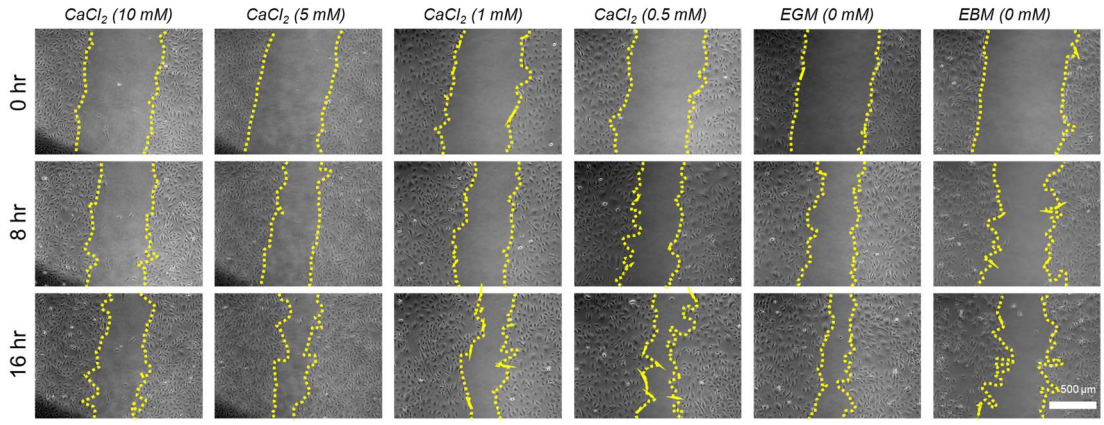


Figure 5.5 Scratch assays test on HUVEC treated with Ca ions at 0, 8, 16 hr post-injury.

As shown in Fig. 5.6, HUVEC exposed to Zn at a concentration of 50 μM showed a drastic increase in cell migration on the scratch-would healing assay after just 8 hrs. Consequently, wound closure was almost completed at 16 hr in the presence of 50 μM Zn. Interestingly, the higher concentration of 100 μM Zn treatment did not further accelerate the migration rate of the HUVEC.

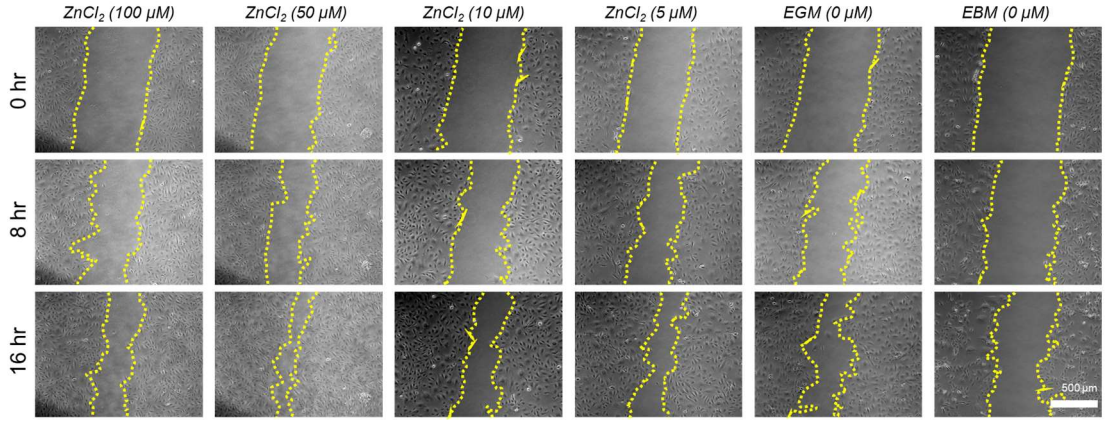


Figure 5.6 Scratch assays test on HUVEC treated with Zn ions at 0, 8, 16 hr post-injury.

5.2.4 Angiogenic gene expression

Total RNA of each metal ion treated cell culture was extracted after 72 hours. It was then concentrated, purified and used to synthesize cDNA using a Maxime RT premix kit. The real-time RT-PCR data were analysed using the comparative threshold cycle (Ct) method. The relative expression of each gene was calculated by comparison with the expression level of GAPDH and subsequently normalized by the value for cells cultured on the control surfaces.

Table 5.1 The oligonucleotide primer sequences

Primers	Forward	Reverse
GAPDH	AGGGGGCAGAGATGATGACC	CAAAGGCTGAGAACGGGAAGC
CD-31	ATTGCAGTGGTTATCATCGGAGTG	CTCGTTGTTGGAGTTCAGAAGTGG
VE-Cadherin	CCTTCCCTTCCCTTCCTCTT	TGGGAGCATACAGACTGGGA
vWF	AGCCGCATGACTGTTCTTTG	AGTTTGCAGGAAAAGGGGAA
Tie-2	AGGATGGAGTGAGGAATGGC	AGAGGGCATCAAAAGGCTGT

The HUVEC, treated Mg-ion exhibited similar or higher expression of proangiogenic genes (VE-cadherin, vWF, and Tie-2) compared to untreated (EGM only) or negative control (EBM only) at 72 hr. For example, 10 mM Mg ion treated HUVEC had a higher expression of endothelial marker genes compared with control groups; (3.90 ± 0.47)-fold for CD31, (1.82 ± 0.03)-fold for VE-Cadherin, (1.37 ± 0.22)-fold for Tie-2 and (2.10 ± 0.01)-fold for vWF compared to EGM. It is well established that the CD31 protein is expressed on all cells within the vascular compartment whereas VE-Cadherein is involved in the cohesion and organization of the intercellular junctions. Tie-2" is a functionally relative gene which maintains the vascular integrity of

mature vessels by enhancing endothelial barrier function and inhibiting apoptosis of endothelial cells. The vWF gene is known to control arterial thrombus formation. These endothelial genes not only participate in the construction and maintenance of a stable endothelial cell layer, but are also related to wound healing, neovascularization, and angiogenesis (Sivaraj and Adams 2016).

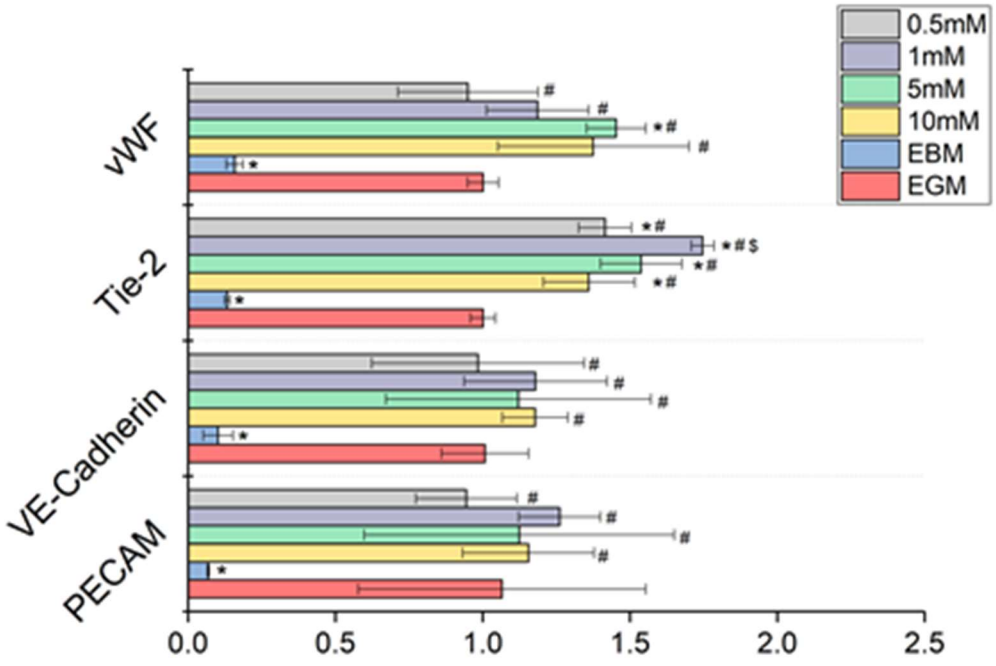


Figure 5.7 Expression of proangiogenic genes after 72 hours from HUVEC treated with increasing content of Mg ions. "", "#", "$" and "&" indicate significant differences compared to EGM, EBM, 10 mM, 0.5 mM, and 1mM of Mg ions, respectively ($p < 0.05$).*

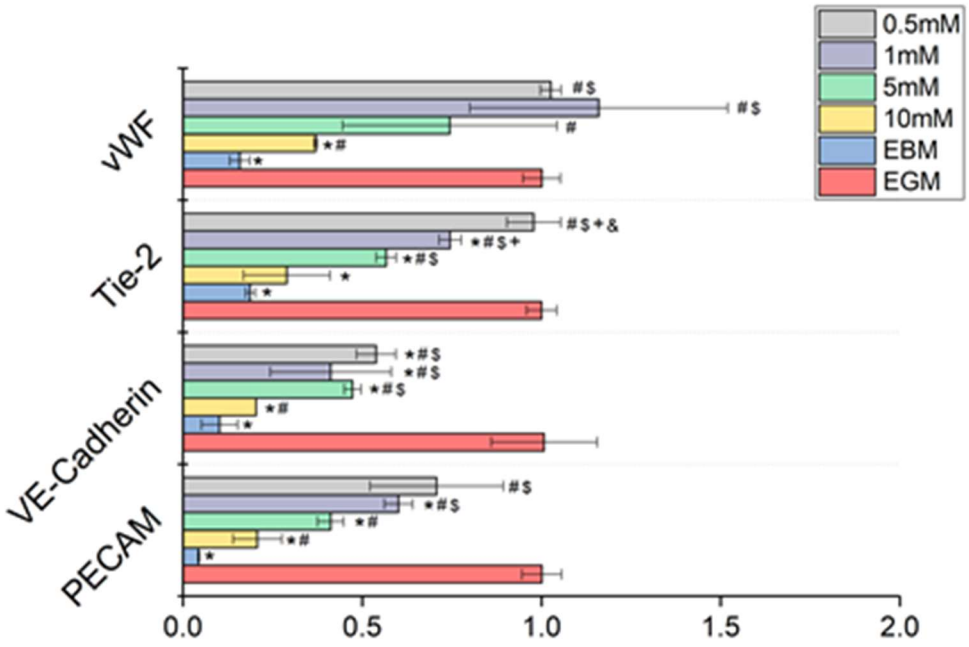


Figure 5.8 Expression of proangiogenic genes after 72 hours from HUVEC treated with increasing content of Mg ions. "", "#", "$" and "&" indicate significant differences compared to EGM, EBM, 10 mM, 0.5 mM, and 1mM of Ca ions, respectively ($p < 0.05$).*

The HUVEC treated with Ca-ions exhibited lower expression of proangiogenic genes (VE-cadherin, vWF, and Tie-2) compared to the positive control (EGM) 72 hr after treatment. In general, lower expression levels of VE-cadherin, vWF, and Tie-2 was observed in HUVEC in the presence of Ca ion when compared to the positive control. For example, 10 mM Ca ion treated HUVEC had a lower expression of endothelial

marker genes compared with those control groups; (0.21 ± 0.07)-fold for CD31, (0.20 ± 0.01)-fold for VE-Cadherin, (0.29 ± 0.12)-fold for Tie-2 and (0.37 ± 0.01)-fold for vWF compared to EGM. The HUVEC treated with Zn-ion exhibited similar or higher expression of proangiogenic genes (VE-cadherin, vWF, and Tie-2) when compared to the positive control or negative control at 72 hr. For example, 50 μM Zn ion treated HUVEC had a similar or higher expression of endothelial marker genes compared with those control groups; (1.19 ± 0.11)-fold for CD31, (4.18 ± 0.80)-fold for VE-Cadherin, (7.57 ± 0.46)-fold for Tie-2 and (4.46 ± 0.40)-fold for vWF compared than EGM. Following the trend indicated by migration studies (scratch assay), a Zn concentration of 50 μM showed the most expression of key proangiogenic markers. The result from this preliminary test shows that the metallic ions released from the Mg5Ca1Zn alloy could effect the proliferation and migration of endothelial cells. Mg ions seem to effect the migration of endothelial cells whereas certain concentration of Zn ions resulted in a drastic increase of both proliferation and migration. Significant increase of proangiogenic gene expression was also observed for the Zn treated HUVEC. The HUVEC treated with high concentration of Ca ions, however, showed an overall decreasing trend for all of the angiogenic assays.

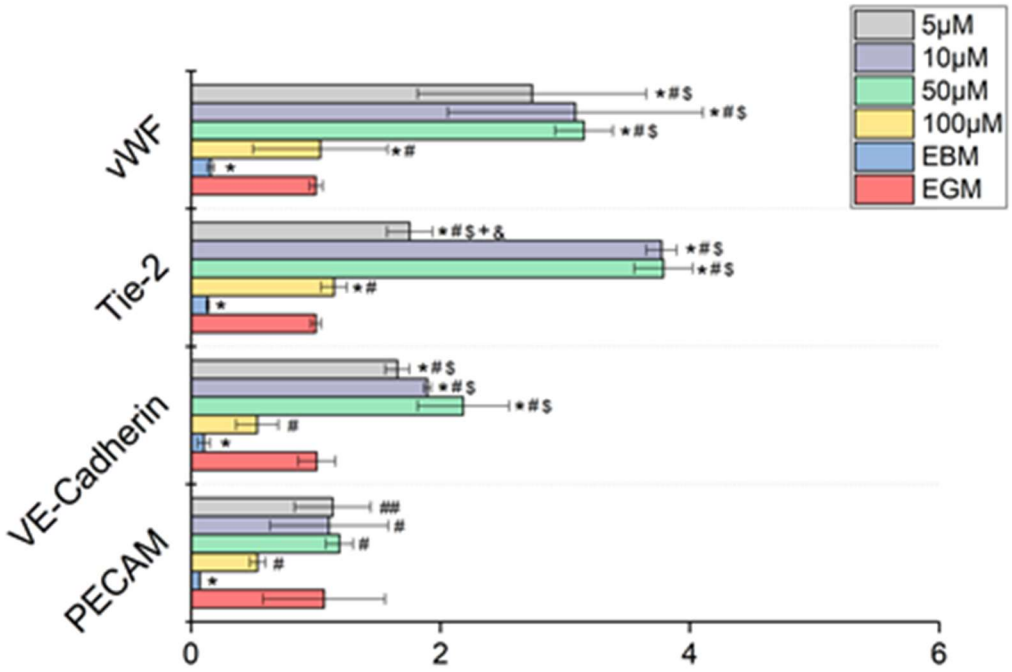


Figure 5.9 Expression of proangiogenic genes after 72 hours from HUVEC treated with increasing content of Zn ions. "", "#", "$" and "&" indicate significant differences compared to EGM, EBM, 100 mM, 50 mM, and 10mM of Zn ions, respectively ($p < 0.05$).*

5.3 Methods for *ex vivo* and *in vivo* study

5.3.1 Fetal Mouse metatarsal angiogenesis assay

Fetal mouse metatarsals were dissected from E17.5 embryos of CD1 mouse. The isolated metatarsals were cultured in 24-well plates with alpha-MEM. The explants were cultured with metal alloys for 5 days using the commercially available Transwell system. After 5 days, the explants were fixed and stained with FITC-conjugated CD31 antibody. Images were observed using confocal laser scanning microscopy (LSM 700, Carl Zeiss, Oberkochen, Germany) and quantified by the Wimasis angiogenesis analysis platform (WIMASIS, GmbH, Munich, Germany)

5.3.2 Angiogenic cytokine arrays

A mouse antibody angiogenesis array membrane was used following the manufacturer's instruction for the analysis of cytokine from angiogenesis of fetal mouse metatarsal bone. Briefly, the metatarsal bone was removed after 5 days of incubation and lysed using RIPA lysis buffer to obtain cell lysate proteins. 250 µg of cell lysate protein were incubated with blocked membrane overnight at 4C. Prepared membranes were detected after incubation with luminescence solution using Gel-Doc image station. The band intensity was scanned and analysed using the ImageJ plug-in "Protein array analyzer"

5.3.3 Surgical preparation of *in vivo* model

The cylinder shaped implant samples made out of Titanium, Mg5Ca and Mg5Ca1Zn were prepared for the *in vivo* experiment. The size of the samples were kept same as the *in vitro* experiments performed in Chapter 4 (1 mm in diameter and 2 mm in length). Following the approval from the Animal Care and Use Committee of Asan Medical Center in Seoul, samples were implanted into femoral condyle of Sprague Dawley (SD) rats for 2 and 4 weeks (n = 4 per implant sample). 6 weeks old SD rats were purchased (OrientBio) and given a week for habituation before the surgical procedure. For anaesthesia, zoletil (10 mg/kg; Virbac SA) and xylazine (5 mg/kg; Bayer Korea) were mixed at 2:1 ratio and injected. Minimally invasive incisions were made on the femoral condyle of SD rats, followed by defect creation of 1 mm in diameter and 2 mm in depth with an electric drill. 0.9% sterile saline was used to clean the defect and appropriate samples were implanted. Incision was sutured with 5-0 black silk and sterilized daily with antiseptic. For a week following the surgery, cefazolin (20 mg/kg) and ketorolac (1 mg/kg) were injected daily as antibiotic and anti-inflammatory therapy.

5.3.4 Sample preparation for second harmonic generation and immunohistochemistry

The preparation of samples for immunohistochemistry was performed following the protocols published by Kusumbe et al (2014). Breifly, freshly dissected femur of SD

rats were fixed immediately in ice-cold 4 % paraformaldehyde solution for 4 hours. Bones were then washed three times with PBS and decalcified in 0.5 M EDTA at 4 °C with constant shaking. For cryoprotection, fully decalcified bones were immersed into cryoprotectant solution made with 20% sucrose and 2% polyvinylpyrrolidone (PVP) solution for 24 hours before embedding. Embedding of tissues were done with 8% gelatin (porcine) solution mixed with 20% sucrose and 2% PVP. Cryosection of embedded tissue was perforemd for both second harmonic generation and immunohistolgy using low profile diamond coated blades on a Leica CM1850 cryostat.

5.3.5 Second harmonic generation

SHG imaging was performed using a dedicated two-photon confocal microscope. Cryosectioned samples were covered with 1.5 coverslip and imaged using a Zeiss Examiner Z1 two-photon excitation laser scanning confocal microscope (Carl Zeiss, Jena, Germany) coupled to a Coherent Chameleon titanium:sapphire laser (Coherent, Glasgow, UK). The excitation wavelength was 840 nm.

5.3.6 Immunohistochemistry

For immunostaining, cryosectioned tissues were air-dried for 20 min and permeabilised for 10 min in 0.3% Triton X-100. Sections were blocked for 30 min at room temperature in 5% donkey serum. The primary antibodies were mixed with 5%

donkey serum in PBS for overnight at 4 °C. The following antibodies were used for this study: Endomucin (sc-65495, Santa Cruz, diluted 1:100), Pecam1 conjugated to Alexa Fluor 488 (FAB3628G, R&D Systems, 1:100), Pecam1 (553370, BDPharmingen, 1:100), Osterix (sc-22536-R, Santa Cruz, 1:200). After incubation in primary antibody solution, sections were washed three times with PBS and stained with secondary antibodies coupled with Alexa Fluor (1:400, Molecular Probes) for 1 hour at room temperature. Sections were thoroughly washed with PBS before mounting with DAPI containing mounting medium and the coverslips were sealed with nail polish. The observation of immunofluorescent stainings were made at high resolution with a Zeiss laser scanning confocal microscope, LSM-710.

5.3.7 Cell sorting by flow cytometry

For flow cytometric analysis, collected femurs were thoroughly cleaned and only the femoral head regions were used. Femoral heads were crushed with mortar and pestle in PBS at 4 °C. Whole bone marrow from the crushed bone was processed with collagenase incubation for 20 min at 37 °C. Same number of cells were stained with appropriate antibody for 45 min and cells were acquired and analysed on a BD Fortessa after washing (BD Bioscience).

5.4 Results and discussion

5.4.1 Fetal mouse metatarsal assay for evaluation of angiogenetic effects of degrading particles

Angiogenesis, which involves new blood vessels sprouting from existing capillaries, has a crucial role in bone development and the healing process. The fetal mouse metatarsal assay allows the observation of sprouting blood vessels in an *ex vivo* microenvironment and closely mimics the *in vivo* formation of natural blood vessel than any other assays available (Song, Fhu et al. 2015). The growth of vessels from isolated embryonic metatarsals captures the key aspects of natural blood vessel formation such as endothelial cell lumen formation, tip cell development, and recruitment of adjacent support cells (Deckers, van der Pluijm et al. 2001). Since it does not require any exogenous factors to stimulate the growth of vessels from the metatarsal, the accurate evaluation of the angiogenic effect of various components can be assessed. Furthermore, development of a complex network of blood vessels in a 2D plane allows quantitative analysis of growth (Marino, Staines et al. 2016). Different concentrations of Mg, Ca and Zn ions were treated in alpha-MEM and metatarsals cultured for 5 days to study the effect of each metallic ion on the growth of blood vessels. As shown in Fig. 5.10, Mg ions facilitated the growth of new blood vessels when treated with 0.1 mM, 1 mM, and 5 mM of Mg ions compared to control which was cultured in alpha-MEM without any ion treatment. Interestingly, 10 mM of Mg ions hindered the *ex vivo* formation of new blood vessels, which did not reflect

the *in vitro* observation of HUVEC proliferation. In the preliminary study, HUVEC showed good proliferation when treated with 10 mM of Mg ions.

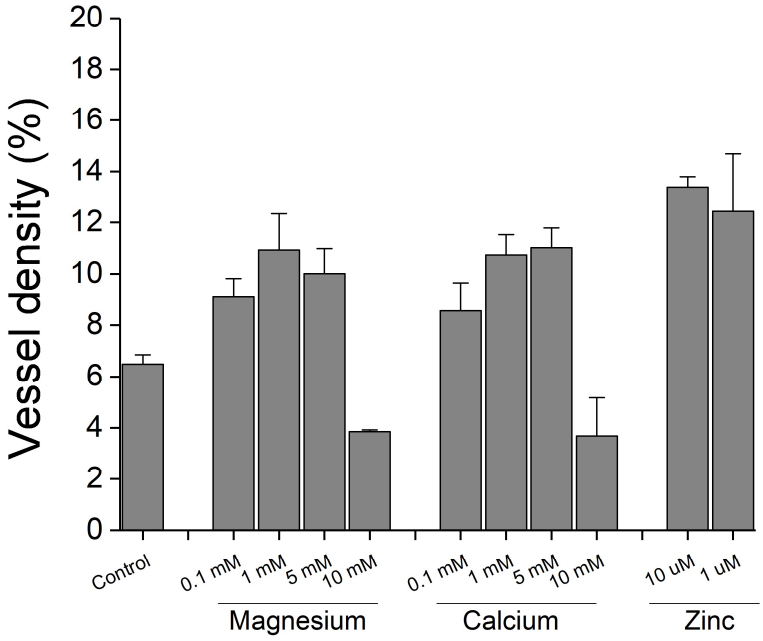


Figure 5.10 Quantified vessel density after 5 days of culture in alpha-MEM treated with different concentration of Mg, Ca and Zn ions.

The addition of Ca ions increased the vessel density after 5 days of culture up to 5 mM, which was in close agreement with the *in vitro* HUVEC proliferation results. As observed in *in vitro* assay, treatment of 10 mM of Ca ions greatly reduced the density of blood vessels. Treatment of 1 μM and 10 μM Zn ions resulted in the highest vessel density for both relatively smaller concentrations of Zn ions which was in agreement with the findings in preliminary study. 10 μM of Zn ions increased the density of vessels by two-fold when compared to the control. However, addition of higher concentration of Zn ions did not improve the vessel density.

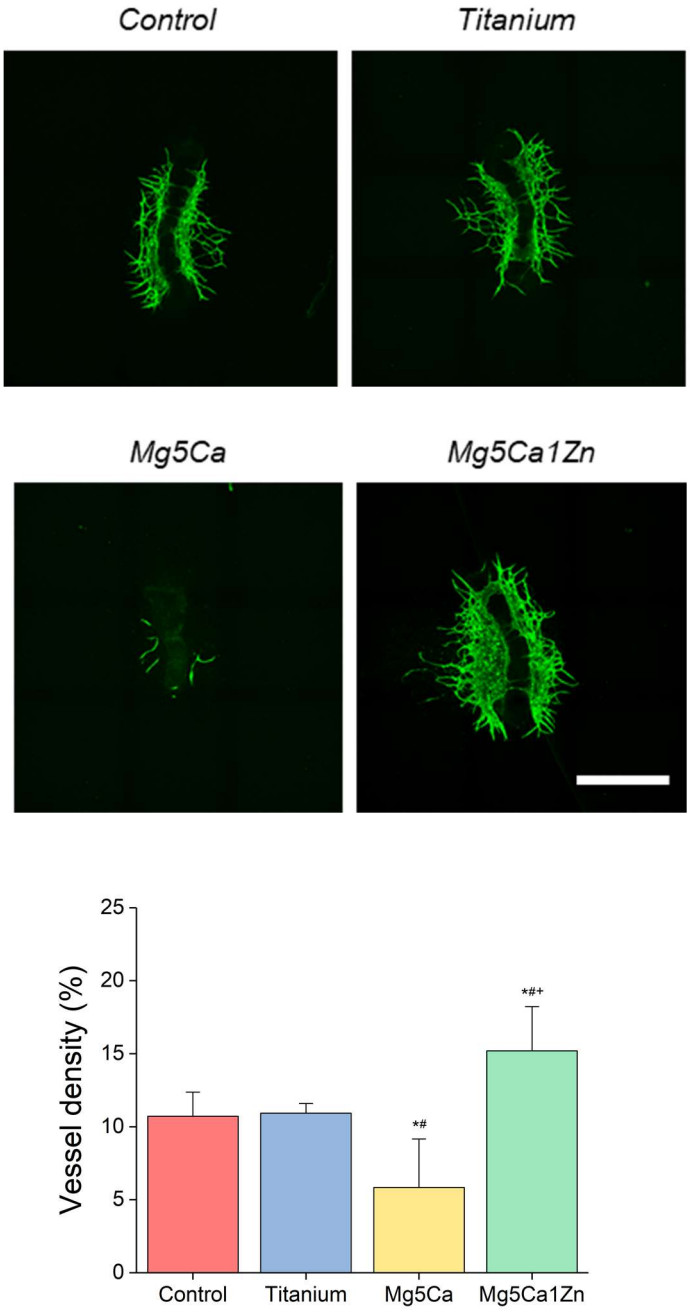


Figure 5.11 (a) Representative fluorescent images of CD31 positive vessel outgrowth from metatarsal growth under different types of metal alloys. (b) Quantification of vessel density. "", "#", and "+" indicate significant differences compared to Control, Titanium and Mg5Ca, respectively ($p < 0.05$). Scale bar, 500 µm.*

The biodegradable metal alloy samples and inert titanium samples were immersed in alpha-MEM using transwells to study the direct effect of biodegradation on angiogenesis through fetal mouse metatarsal assay. As shown in Figure. 5.11 a-b, biodegradation and released metallic ions from Mg5Ca1Zn samples significantly induced angiogenesis, demonstrating a web-like complex of blood vessel structures in the cultured metatarsal. This is due to the slow corrosion rate of Mg5Ca1Zn samples which leads to release of Mg,Ca, and Zn ions at the level that facilitates the better growth of new blood vessels. Media cultured with Titanium samples showed a similar trend to the control sample due to the corrosion resistant nature of the Titanium. Titanium remains intact during the entire period of metatarsal culture and does not release any metallic particles into the environment to effect angiogenesis. In contrast, angiogenesis was significantly inhibited for the metatarsals cultured in media containing the Mg5Ca samples. Rapid corrosion of the Mg5Ca in alpha-MEM results in an increase in pH level and release of higher concentrations of metallic ions into the sorroundings. The results from this experiment showed that slow degrading Mg5Ca1Zn promote growth of blood vessels in the *ex vivo* environment by releasing the optimized quantity of metallic ions.

The metatarsal assay allows extraction of RNA and proteins from the vessel outgrowth and the influence of degradation of biodegradable metal alloys on the proangiogenic secretory profile was investigated using cytokine arrays. These angiogenesis arrays consist of activators and inhibitors, that activate or inhibit the growth of new blood vessels. Following observations from the blood vessel density analysis using the staining methods, a normalized heat map of protein expression to

cell number showed an increase in expression of proangiogenic proteins for metatarsals cultured with Mg5Ca1Zn samples. As shown in Fig. 5.12, slighly lower expression of inhibitors was observed for Mg5Ca1Zn groups when compared to control and Titanium groups. However, metatarsals cultured with Mg5Ca samples showed a decreased expression of angiogenic activator levels and higher secretion of angiogenic inhibitors. In addition, there was no significant difference between control and Titanium groups. The quantified results closely reflected that of the blood vessel density analysis and was inagreement with the *in vitro* assays performed in the preliminary section of this chapter.

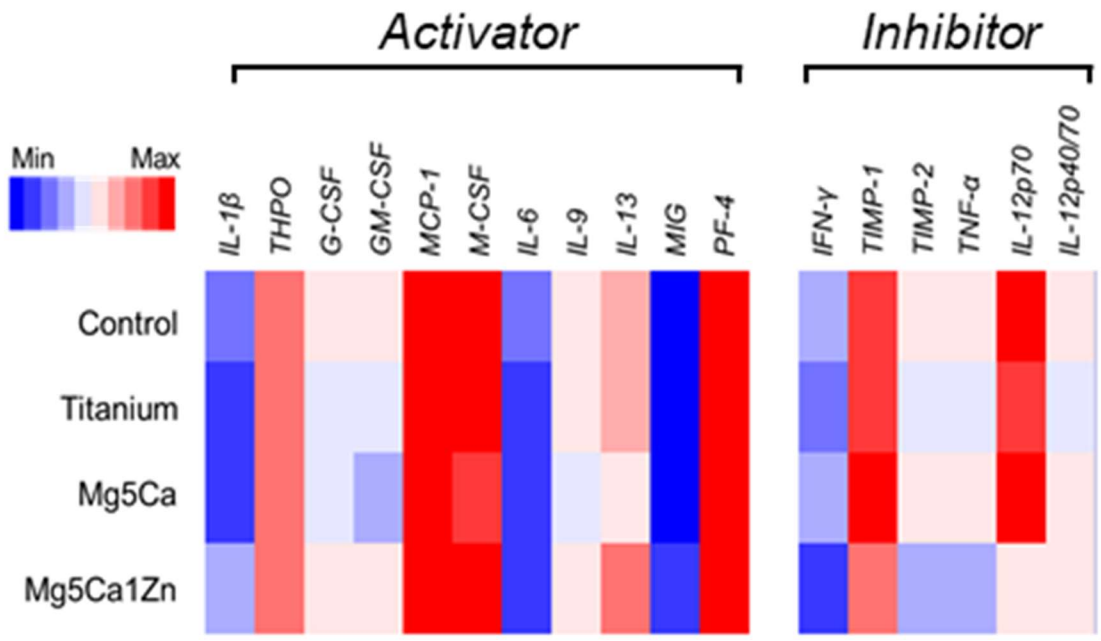


Figure 5.12 Heat map of angiogenic cytokine expression

5.4.2 Evaluation of collagen profile near implanted Magnesium implant through second harmonic generation

The bone fixation devices must be able to sustain the mechanical loading without causing severe immune response to facilitate the new bone growth at the fracture site. For biodegradable materials, a slow degradation rate is required to allow such integration of the implant to the surrounding tissue. Fast degrading magnesium alloy such as Mg5Ca in the physiological environment, leads to release of hydrogen gas and metallic ions at a rate that is impossible for normal fracture healing to occur.

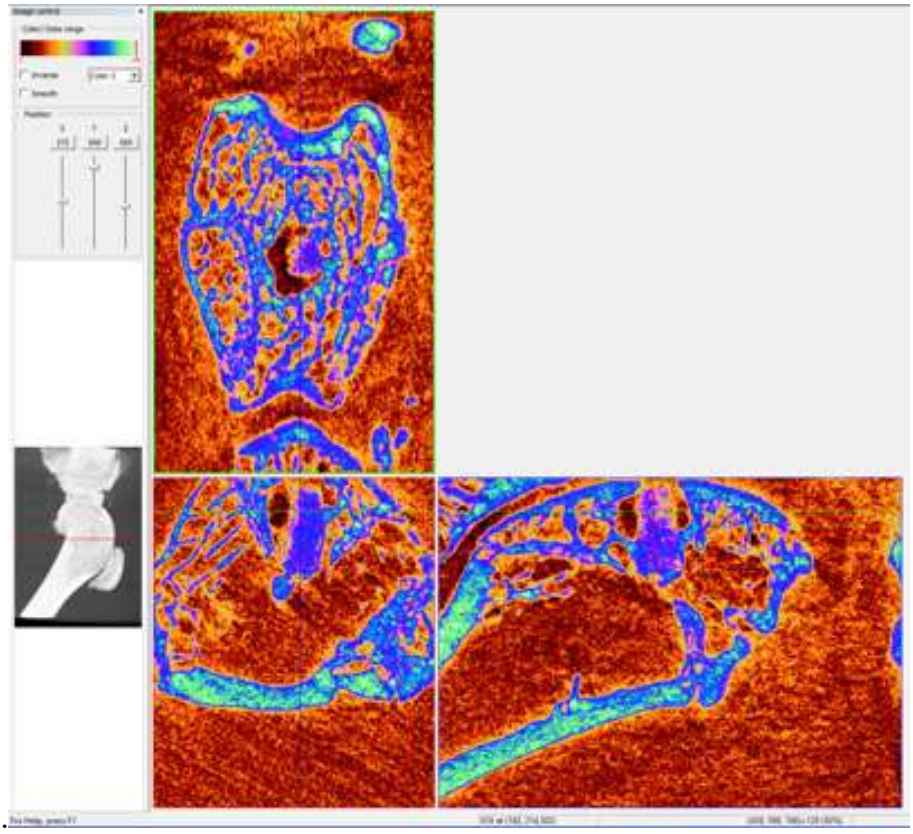


Figure 5.13 live µCT image of fast degrading Mg alloy in SD rats.

As shown in Fig. 5.13, implantation of fast degrading Mg alloy in the femoral condyle of SD rats resulted in insufficient healing of the bone defect site. It also showed a formation of low-density tissue next to the implant appearing as an empty space in bone created by the implant. However, it clearly shows darker colour when compared to the confirmed empty spaces, suggesting the possibility of diseased fibrotic tissue formation. Fibrotic disease at the implantation site normally occurs when the wound healing process fails to complete following the implantation of foreign materials. In general, an immune response immediately follows the implantation of foreign devices and sends the inflammatory cells to remove them. An inflammatory response continues until the foreign material is covered with a fibrotic connective tissue when the foreign body cannot be removed by the inflammatory cells (Wynn 2008). Collagen is the one of the main components of such fibrosis and accounts for roughly 30% of the total protein mass in the human body (Viguet-Carrin, Garnero et al. 2006). There are several techniques available to study the collagen structure of the implanted site and immunohistochemical staining of collagen is one of the most commonly used technique. However, staining of sections containing biodegradable metal results in active corrosion of the implanted metal by the staining solution, and leads to generation of hydrogen gas bubbles to hinder the accurate analysis of the collagen structure. Recently, a technique to obtain thick cryosection for high resolution 3D imaging of bone was introduced by the Kusumbe et al (2015). This method was adapted to obtain thick section of femoral condyle implanted with Mg samples for SHG imaging which allows staining free imaging of collagen (Ranjit, Dvornikov et al. 2015).

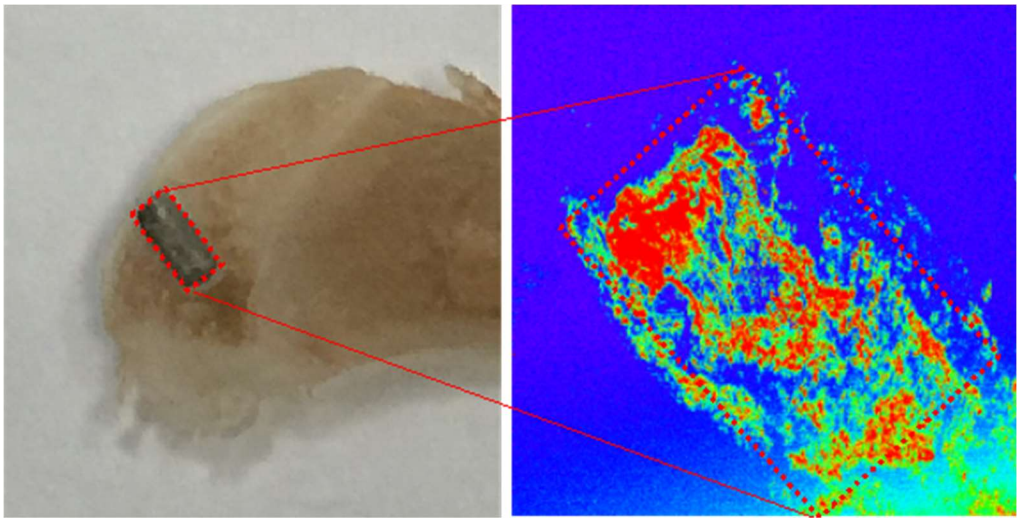


Figure 5.14 Thick cryosection of femoral condyle of SD rats implanted with Mg5Ca1Zn sample for 4 weeks and resulting SHG image of collagen deposits on the surface of implanted Mg5Ca1Zn sample. Green and Red colors represent the increasing concentration of collagens detected by the SHG.

Among different types of collagens, collagen type I comprises about 95% of the entire collagens in bone and approximately 80% of the all proteins that exits in bone (Niyibizi and Eyre 1994). Other types such as collagen type III and V are found at low levels in bone (Niyibizi and Eyre 1989, Niyibizi and Eyre 1994). For SHG, collagen type I and II gives off the strongest signals and collagen type III results in relatively weak signals (Chen, Nadiarynkh et al. 2012). Collagen type IV and V does not produce any SHG signals. 4-week post-operation SHG image of Mg5Ca1Zn implant in femoral condyle of SD rats show high amount of collagen deposits on top of the implant sample (Fig. 5.14). The even distribution and high intensity of the SHG signals confirms the abundance of collagens adjacent to the implant and confirmed the *in vivo* efficacy of Mg5Ca1Zn samples.

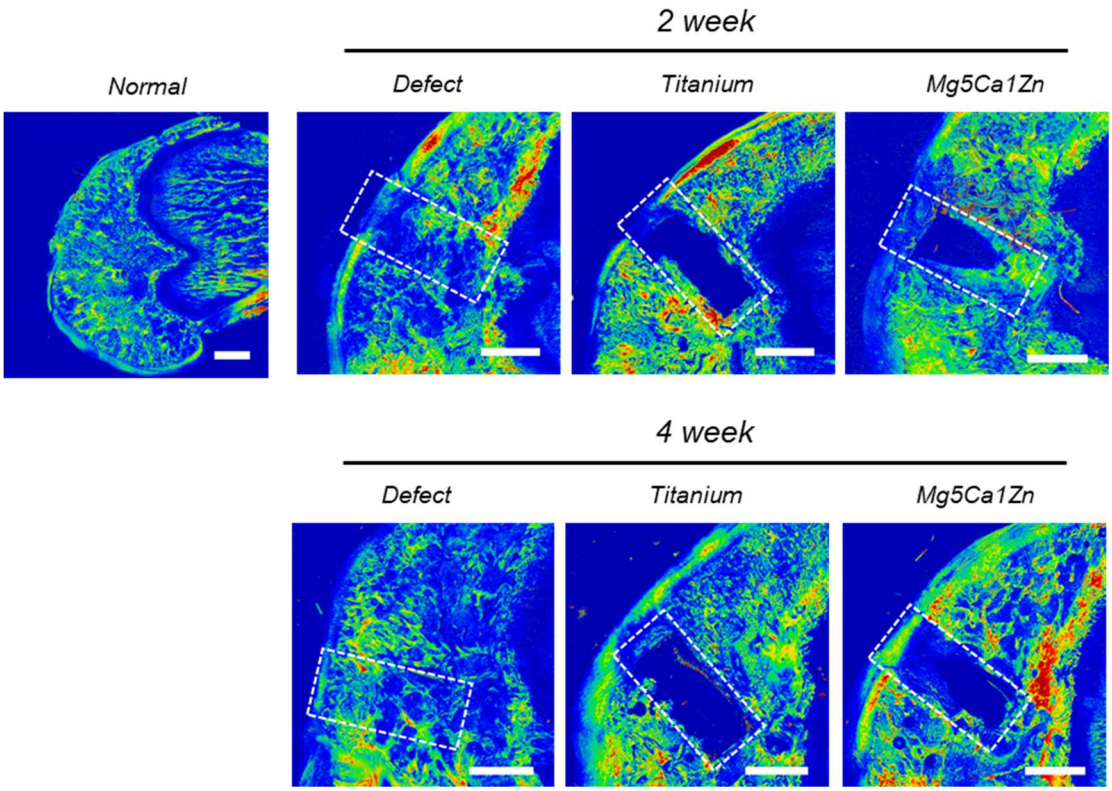


Figure 5.15 SHG images of normal SD rat femur, empty defect site, titanium, Mg5Ca1Zn samples after 2 and 4 weeks postoperation. Scale bar represents 10 mm in length and white dash lines represent the original defect created during surgery. Scale bars, 8 mm.

During the bone formation process, osteoblasts synthesize and initially deposit type I collagen in random directions. Such structure is called woven bone due to randomly woven nature of the collagen fibres. The strength of woven bone is significantly lower than the final bone structure which has aligned fibres. Over time, woven bone is converted into lamellar bone with aligned fibres and the osteoblasts deposit osteoid to calcify the lamella bone to produce primitive cancellous bone. For the sites that require cortical bones, increase of the density if obtained by further deposition of osteoid.

In order to study the efficacy of Mg5Ca1Zn samples further, implanted bone images were compared to the SHG image of titanium samples and empty defect sites created in the femoral condyle of SD rats after 2 and 4 weeks (Fig. 5.15). After 2 weeks of implantation, SHG images of biodegradable Mg5Ca1Zn samples showed good connection with the surrounding tissues without empty void spaces and abundance of collagen at the implantation site. Titanium implanted in bone is known to result in osteointegration which allows direct deposition of new bones on the surface of the Titanium and facilitate new bone growth without complications. The empty defect site was not yet healed completely and structure of the collagen near Mg5Ca1Zn resembled that of the empty defect site more closely than that of Titanium samples. This could be related to the active biodegradation of Mg5Ca1Zn. The cortical bone was not completely closed for all of the tested group after 2 weeks. After 4 weeks of implantation, the cortical bone was completely closed for all the tested groups and Mg5Ca1Zn alloy showed similar SHG signals to the ones from bioinert Titanium implants. Thicker cortical bone was created on top of the Mg5Ca1Zn without the

voids observed in fast corroding Mg samples. This result clearly shows the direct deposition of collagen matrix on the surface of degrading Mg5Ca1Zn and growth of new bone tissue around the degrading Mg5Ca1Zn samples which is equivalent with the clinically proven Titanium samples. There is no previously reported study on the application of SHG to observe the collagen structures near the biodegradable metals. Utilization of SHG allowed observation of collagen structures near the biodegradable alloy without the generation of hydrogen gas bubbles and showed that the newly developed Mg5Ca1Zn alloy facilitates good direct collagen deposition for new bone formation.

5.4.3 Immunohistological evaluation of degrading implant

The adjacent cryo-sectioned slide obtained after sectioning of the thick metal containing slide used for SHG was prepared for immunohistological evaluation. During the bone formation process, MSCs produce new osteoblast progenitors and osteoblasts required for bone fracture healing and to achieve homeostasis of bone. Recent studies have found that the growth of blood vessels is coupled with osteoprogenitor invasion in healing of fractures (Riddle, Khatri et al. 2009, Kusumbe, Ramasamy et al. 2014). This study reported that capillaries in the murine skeletal system can be divided into two types; H and L. Type H blood vessels are relatively small in quantity and shows high expression of CD31 and Endomucin. They are found mostly in actively remodelling sites within the bone and deemed to be the building block for new bones. Interestingly, Osterix-positive osteoprogenitors are

found to be positioned selectively around the type H blood vessels and not L blood vessels.

As shown in Fig. 5.16, immunostaining of the normal bone section shows the blood vessel structures within the bone stained by Endomucin and a few scattered Osterix-positive cells involved in bone remodelling. More Osterix-positive osteoprogenitors are found around the empty defect site and are more densely located near the defect site where active bone regeneration is occurring. Interestingly, femurs implanted with titanium showed almost cortical-like dense bone layers formed on the surface of the titanium. Significantly increased numbers of Osterix-positive cells were found in these dense new bone layers when compared to the regions distant from the implant site. Implanted Mg5Ca1Zn samples showed a similar tendency to the Titanium samples by revealing significantly increased numbers of Osterix-positive cells located near the implantation site. Creation of densely packed bone near the implant surface was not observed for the Mg5Ca1Zn samples and this could be related to the actively degrading surface of the Mg5Ca1Zn.

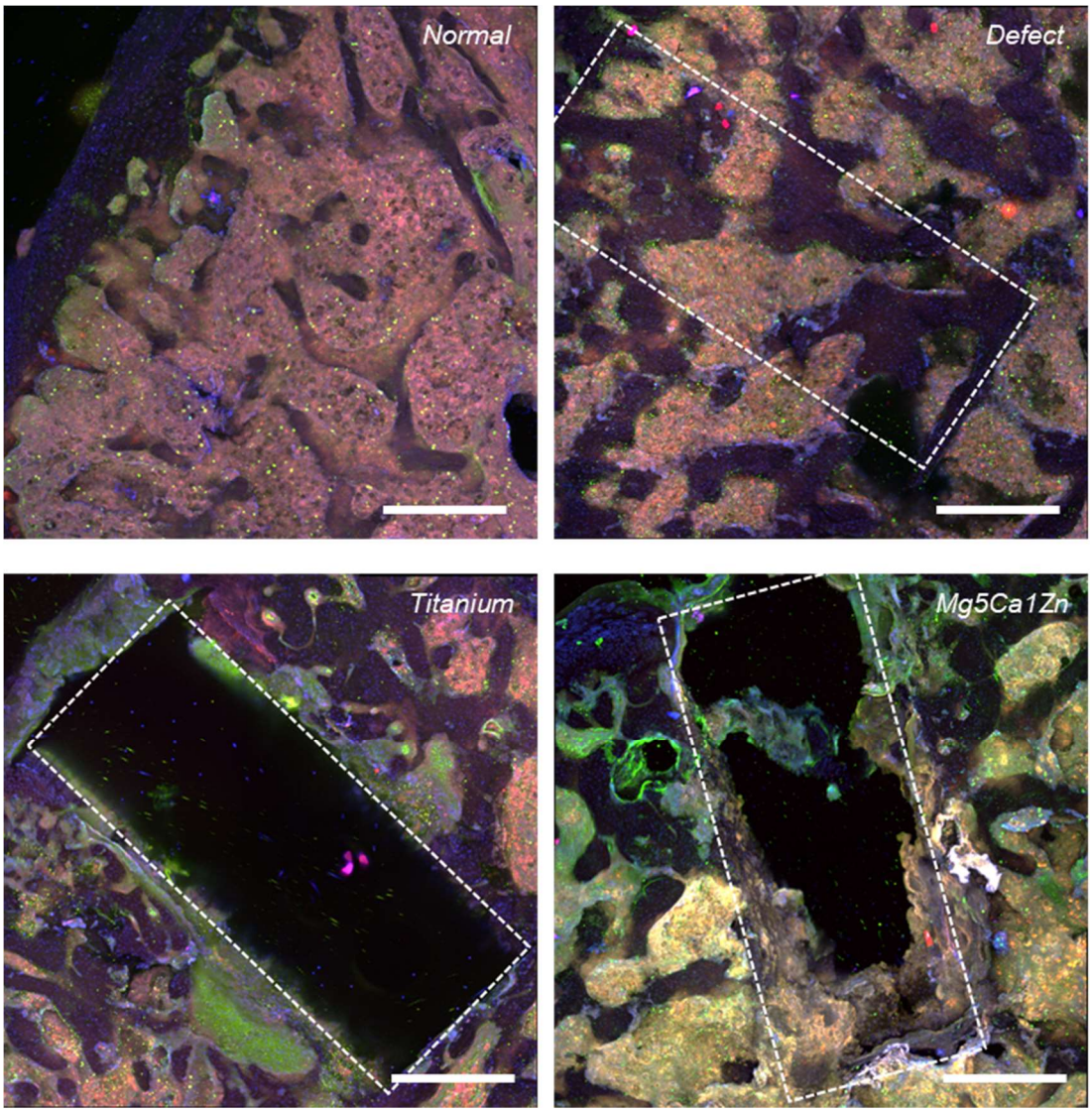


Figure 5.16 Confocal microscropy images of immunostained sections from normal bone, empty defect site, titanium, Mg5Ca1Zn samples after 4 weeks postoperation (Endomucin – Red, Osterix – Green, DAPI – Blue). Scale bars, 5 mm.

Newly generated bone tissue was observed in direct contact with the degrading surface of the Mg5Ca1Zn samples, showing good biocompatibility of the material. Confocal imaging of the whole femoral head implanted with Mg5Ca1Zn was performed at higher resolution to assess the overall distribution of Osterix-positive cells and observe the active bone remodelling near the implantation site. Fig. 5.17 shows the whole image of the immunostained femoral head section that contained the Mg5Ca1Zn sample. The Mg5Ca1Zn implant was carefully removed before staining to avoid the formation of hydrogen gas bubbles. The complete image of the femoral head allows for the observation of Osterix-positive cells distribution around the actively remodelling sites of the bone indicated by yellow arrows. A magnified high-resolution image of the implantation site revealed densely packed Osterix-positive cells located around the type H blood vessels formed near the implantation site. This result indicates that Mg5Ca1Zn samples facilitates optimal bone healing by releasing metallic ions and actively recruiting osteoprogenitors near the implant site at a degradation rate acceptable for the tissue.

The quantification of Endomucin, Osterix and CD31 (PECAM) using flow cytometry validated and reflected the outcomes of experiments performed in this chapter (Fig. 5.18). As mentioned before, high expression of CD31 and Endomucin represents the type H blood vessels in the femoral head. The portion of such blood vessels is reported to be 1.77% in younger mice (4 weeks old) with active bone growth (Kusumbe, Ramasamy et al. 2014). The result from this study showed approximately

1% of type H blood vessels in the normal adult femoral head which is supported by with the previously reported findings (Kusumbe, Ramasamy et al. 2014). As shown in Fig. 5.17, high expression of CD31 and Endomucin was about 1.43%, 0.75%, and 1.91% for empty defect, Titanium and Mg5Ca1Zn group, respectively.

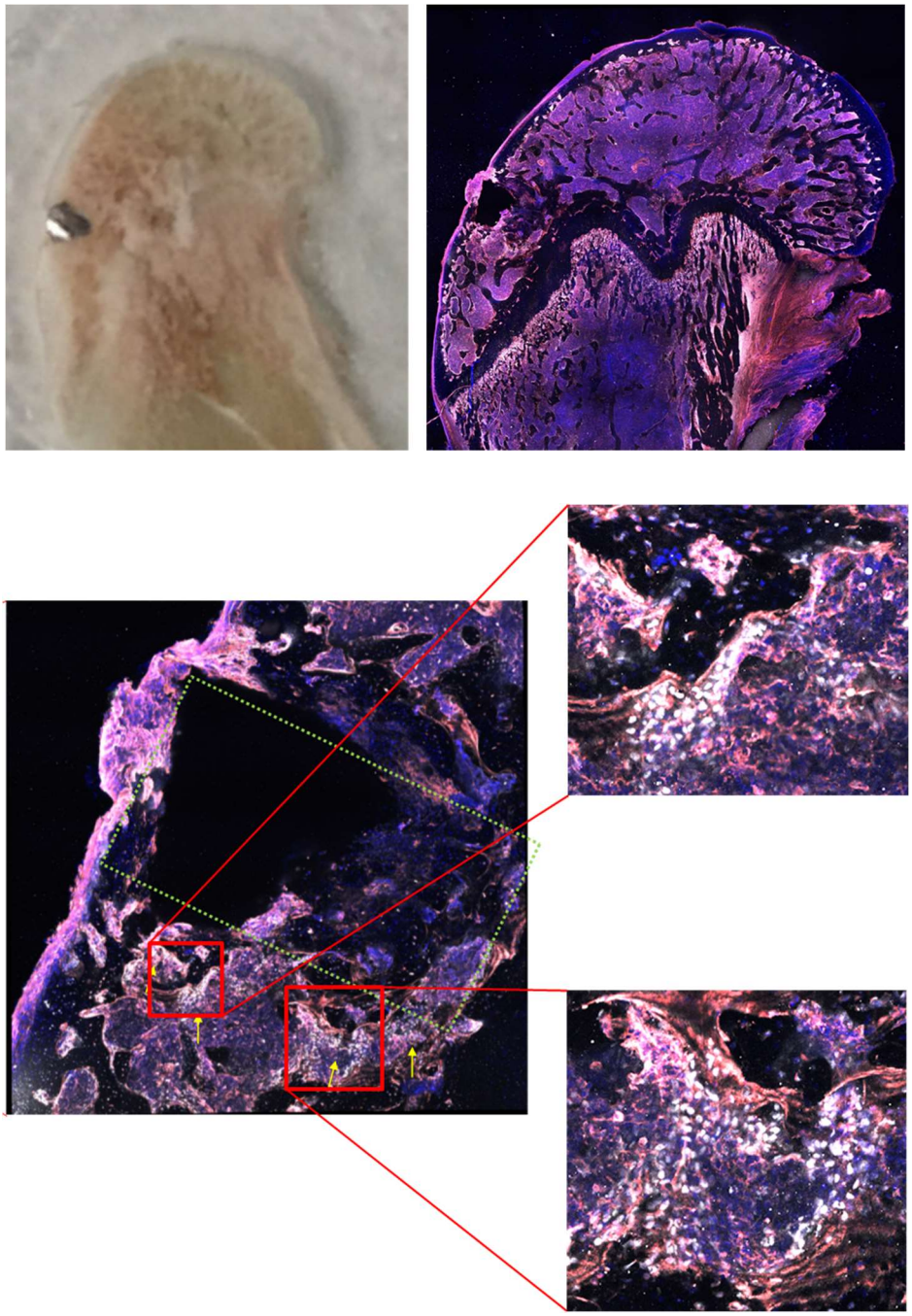


Figure 5.17 High resolution confocal microscropy images of immunostained sections Mg5Ca1Zn samples after 4 weeks postoperation (Endomucin – Red, Osterix – White, DAPI – Blue).

The SHG imaging showed an abundance of deposited collagen matrix near the Mg5Ca1Zn implantation site after 2 weeks when compared to the Titanium group. Interestingly, flow cytometry results showed that there are a higher number of H type blood vessels within the femoral head implanted with Mg5Ca1Zn samples when compared to the Titanium group. The empty defect group showed a higher number of H type blood vessels than the normal group that did not receive any surgical treatment and titanium group showed slightly fewer H type blood vessels. The difference between the number of type H blood vessels in Mg5Ca1Zn and Titanium was reduced, and the relative abundance of H type blood vessels were 0.77% and 0.67% respectively. This could be related to the slower degradation rate of Mg5Ca1Zn caused by the formation of a protective magnesium hydroxide layer. At the initial stages of corrosion, there are higher numbers of metallic ions released into the environment. However, as the magnesium degradation progresses, a corrosion protective layer is formed to slow and stabilize the degradation rate. As demonstrated *in vitro* and *ex vivo*, released Mg, Ca and Zn ions would increase the proliferation of endothelial cells and the growth of new blood vessels. This would result in a higher number of blood vessels generated near the implantation site which is ultimately coupled with osteogenesis. This is clearly demonstrated in the Fig. 5.19 which shows higher relative abundance of Osterix-positive cells in samples implanted with Mg5Ca1Zn after 4 weeks. The relative quantity of Osterix-positive cells is similar for the Titanium group and Mg5Ca1Zn group after 2 weeks (0.44% for Titanium and 0.42% for Mg5Ca1Zn) but the difference between the two groups is nearly doubled after 4 weeks (0.35% for Titanium and 0.60% for Mg5Ca1Zn). A decrease in the

relative number of Osterix-positive cells in the defect model over time is also in good agreement with the findings described in this chapter.

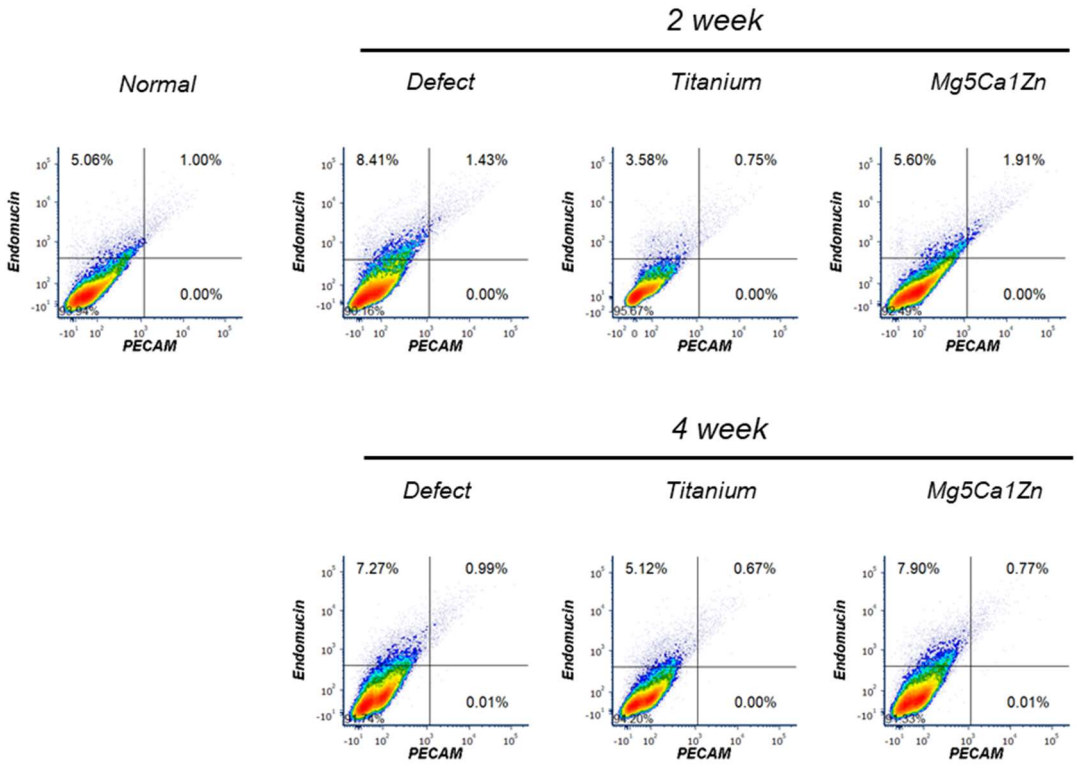


Figure 5.18 Flow cytometry dot plots showing expression of PECAM and Endomucin from the cells collected from femoral head of SD rats with empty defect site, Titanium or Mg5Ca1Zn after 2 and 4 weeks postoperation.

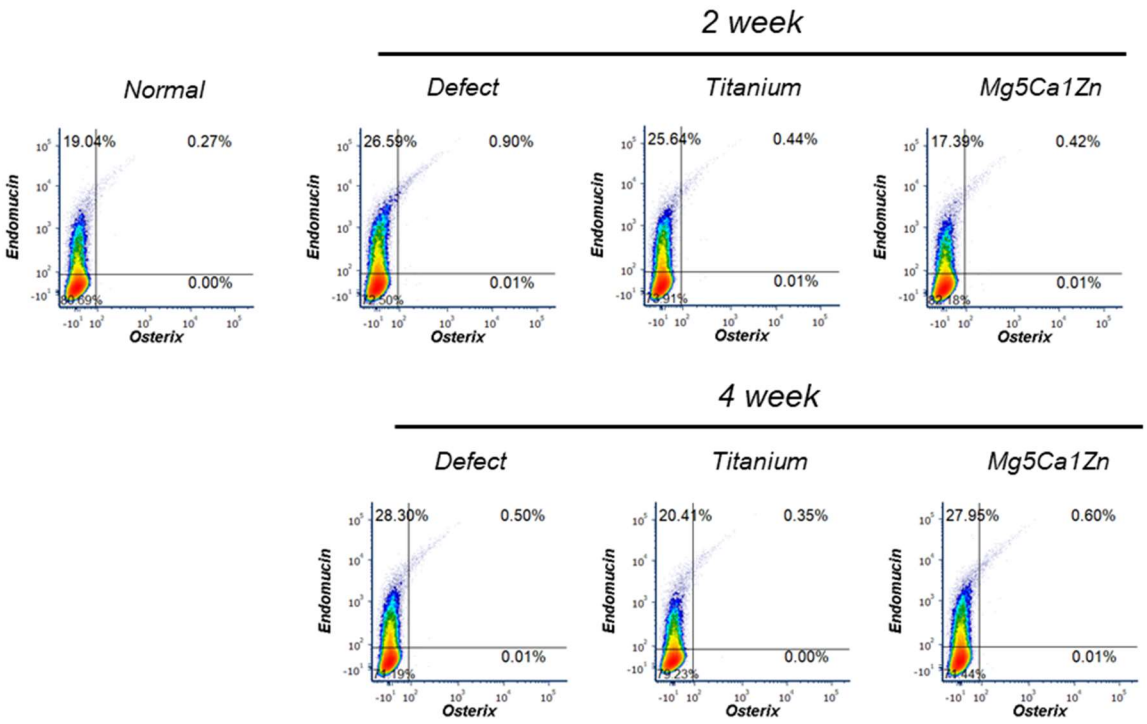


Figure 5.19 Flow cytometry dot plots showing expression of Osterix and Endomucin from the cells collected from femoral head of SD rats with empty defect site, Titanium or Mg5Ca1Zn after 2 and 4 weeks postoperation.

5.5 Conclusion

In this chapter, several state-of-the-art techniques were used to observe the bone formation around the biodegradable Mg5Ca1Zn alloy. The results from this series of experimental studies suggest that metal ions released by the degrading Mg alloy will confer a favourable effect within the bone microenvironment leading to increased numbers of blood vessel growth which in turn is followed by osteogenesis. The *in vitro* assays and fetal mouse metatarsal assay validated the positive effect of released metallic particles on angiogenesis, and SHG imaging showed an excellent deposit of collagen matrix on the implantation site of Mg5Ca1Zn. These results were validated with immunostained slides that showed good contact between new bone tissues and the degrading surface of the Mg5Ca1Zn sample. The findings from this chapter demonstrate that Mg5Ca1Zn samples facilitates optimal bone healing by releasing metallic ions into the surrounding tissues to enhance the growth of blood vessels and to actively recruit osteoprogenitors near the implant site at a degradation rate acceptable for the tissue.

Chapter 6

Zebrafish model for evaluation of *in vivo* toxicity for biodegradable metals

6.1 Introduction

As summarized in the previous chapters, magnesium alloy-based biomedical implants with biodegradable characteristics have been evidenced to facilitate tissue repair and regeneration, for instance in the treatment of cardiovascular disease and bone fracture healing (Li, Wong et al. 2012, Cha, Han et al. 2013, Cho, Chae et al. 2013, Lee, Han et al. 2016). These biodegradable metallic materials extend mechanical support to the damaged tissue/organ, thereby ensuring sufficient healing, and also degrade over time to facilitate complete replacement by the healthy host tissue (Seitz, Eifler et al. 2014, Pogorielov, Husak et al. 2017, Zhao, Wang et al. 2017).

The replacement of currently available bioinert implant materials with biodegradable metals may result in the elimination of second surgeries to remove the implant and reduce the economic burden on healthcare systems of an ageing society (Bachoura, Yoshida et al. 2012, Reith, Schmitz-Greven et al. 2015). In the biometal development process, identification of suitable alloying elements is a crucial step in the

formulation of new alloys. This is because the type and quantity of alloying element modification can improve the degradability and mechanical properties of the metal (Ding, Wen et al. 2014, Radha and Sreekanth 2017). Mg-based biodegradable metallic implants typically are alloyed with biocompatible elements such as calcium and zinc; aluminium, which is linked to Alzheimer's disease; and rare earth element yttrium, which is associated with hepatotoxicity. The combination of these materials also often augments the corrosion resistance and mechanical properties. During degradation, the ions released from the biodegradable metallic implant could cause toxicity to the host tissue and as such, it is essential to determine the toxicity of the alloying elements in the biodegradable metals (Zheng, Gu et al. 2014, Li, Liu et al. 2016, Cipriano, Lin et al. 2017, Nabiyouni, Bruckner et al. 2018).

In general, initial assessment of toxicity for biodegradable metal is performed through *in vitro* studies of different cell types. Cytotoxicity is measured through viability of cells exposed to medium treated with metal ion in chloride form or extracts from the degrading alloy (Murni, Dambatta et al. 2015, Grillo, Alvarez et al. 2016, Huang, Cheng et al. 2016, Liu, Wu et al. 2017). In terms of both time and cost such assays have been proved to be efficient. However, all the complex aspects of a physiological environment cannot be replicated in two-dimensional cell monolayers. In this regard, small mammalian models have been found to be more useful for the toxicity evaluation and biodegradation profile estimation of alloying elements in humans. Small animals such as mice, rats, rabbits, and dogs have served as subjects for toxicology experiments over past decades, but these types of *in vivo* experiments are often time consuming and significantly more expensive. Recently, researchers (Fako

and Furgeson 2009, Wang, Ma et al. 2013) proposed using zebrafish (*Danio rerio)* as an *in vivo* model for nanotoxicity assessment. This recommendation was based on the anatomical and physiological similarities of the cardiovascular, nervous, and digestive systems as well as the homology between fish and human genomes (Pyati, Look et al. 2007, McGrath and Li 2008, Flicek, Amode et al. 2014). Moreover, the evaluation time is reduced as zebrafish embryos generate the major organ structures in less than 1 week (Rubinstein 2006, Li, Miao et al. 2017), and a real-time observation is made possible with a transparent body structure throughout development (Benjamin and Hynes 2017, Lee, Jang et al. 2017). In comparison to larger animals, the significant cost and time reduction in toxicity testing is also apparent through the high fecundity rate of 200–300 eggs per day every 5–7 days (Berghmans, Jette et al. 2005, Chakraborty, Sharma et al. 2016). As such, it can be safely expected that the material development process to clinical application can be optimized and sufficiently accelerated with the zebrafish model application in *in vivo* toxicity evaluation of degrading ions from biodegradable metal implants that are newly developed (Figure 6.1). At the same time, the process allows for circumvention of the ethical considerations entailed in using mammals as research tools.

In this chapter, the zebrafish embryos are exposed to varying concentrations of alloying elements from biodegradable metals for *in vivo* toxicity assessment. The metal ions used in the experiments included Mg, Zn, Ca, Y, and Al ions, which represent the five most commonly used alloying elements. This investigation conducted parallel standard cellular toxicity tests on established heart, liver, and endothelial cell lines with the objective to compare toxicities for both *in vitro* and *in*

vivo settings. Transgenic zebrafish lines expressing enhanced green fluorescent protein (EGFP) or red fluorescent protein (RFP; DsRed) in blood vessels, heart and liver, and nervous system under the control of the promoters of fetal liver kinase (flk)1, cardiac myosin light chain (cmlc)2, liver-type fatty acid-binding protein (lfabp), glial fibrillary acidic protein (GFAP), and oligodendrocyte transcription factor (olig)2 were utilized in the study to ascertain the resulting developmental defects in these tissues due to exposure to various concentrations of the alloying elements.

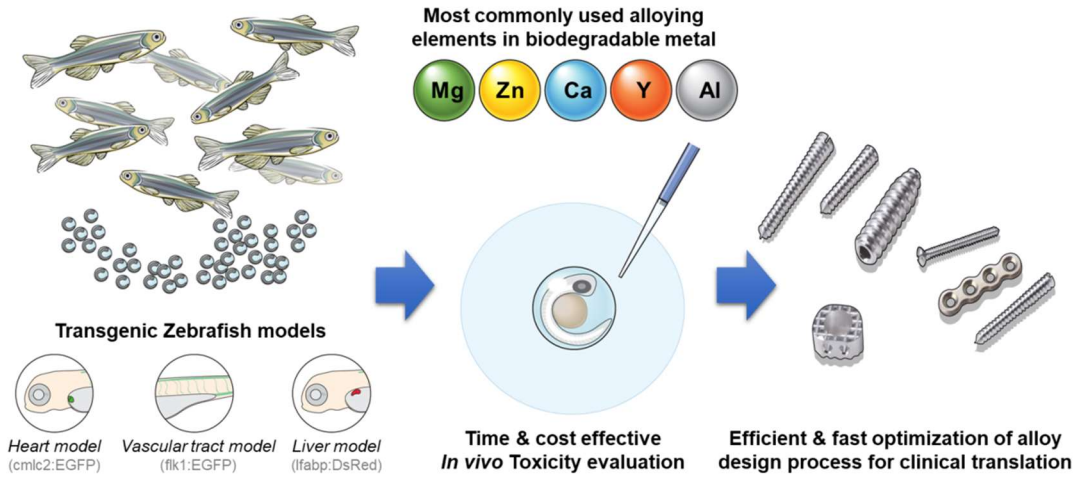


Figure 6.1. The in vivo toxicity assessment of most commonly used biodegradable metal alloying elements in zebrafish.

6.2 Materials and Methods

6.2.1 Cell cultures

For *in vitro* studies HL-1 cardiac muscle-like cells, Huh7 hepatocytes, and human umbilical vein endothelial cells (HUVEC) were utilized. The HL-1 cells were sourced as a gift from Dr. Craig Lygate, University of Oxford and cultured in Claycomb medium supplemented with 10% fetal bovine serum (FBS), 1% penicillin-streptomycin, and 1% L-glutamine in a fibronectin/gelatin pre-coated culture dish. Also, the Huh7 cells sourced as a gift from Dr. Leanne Hodson, University of Oxford were cultured in Dulbecco's Modified Eagle's Medium with 10% FBS and 1% penicillin-streptomycin. HUVEC (Sigma-Aldrich, St. Louis, MO, USA) were maintained in endothelial cell growth medium. Standard condition, i.e., 37°C, 5% CO_2, were maintained for all cell cultures.

6.2.2 Cell viability assay

The Water-Soluble Tetrazolium salt (WST)-1 colorimetric assay (Abcam, Cambridge, MA, USA) was used in order to assess the cell viability. In a 96-well plate, the Huh7 cells and HUVEC were seeded at a density of 1×10^4 cells/cm^2. A fibronectin/gelatin pre-coated 96-well plate was used for seeding HL-1 cells at a density of 1×10^4 cells/cm^2. WST-1 reagent was incorporated within the cultures, after 24 h. Following

which, an additional 2 h incubation was performed on the plates. On a spectrophotometer the enzymatic activity was measured at 450 nm. Data were calibrated to align with the absorbance value of cell-free medium and subsequently normalized to the value for cells cultured without ion treatment.

6.2.3 Zebrafish models

For the study purposes, Zebrafish Resource Bank (ZOMB) at Kyungpook National University (Daegu, Korea) was accessed to source: Wild-type (AB strain), Tg(flk1:EGFP), Tg(cmlc2:EGFP), Tg(lfabp:DsRed), Tg(GFAP:EGFP) and Tg(olig2:DsRed) zebrafish. These were maintained under a 14 hr: 10 hr light: dark cycle at 28 °C, as per the standard approved guidelines at the zebrafish facility of the Kyungpook National University. For necessary compliance, all experimental protocols were approved prior to conducting actual experiments, by the Institutional Review Board (IRB) of the Kyungpook National University.

6.2.4 Chemical treatment of zebrafish embryos

$MgCl_2$, $ZnCl_2$, $CaCl_2$, YCl_3, and $AlCl_3$ were dissolved with distilled water and diluted with zebrafish embryo medium in 6-well plates. A total of 10–15 zebrafish embryos were treated at various concentrations at 6 hpf with $MgCl_2$, $ZnCl_2$, $CaCl_2$, YCl_3, and $AlCl_3$ solutions. The embryos were observed with Stemi 2000, Imager Z1, and

Axioskop (Carl Zeiss, Oberkochen, Germany) and MZFL III, S6D, and DMI6000B (Leica, Wetzlar, Germany) microscope systems. The assay was repeated three times.

6.2.5 Zebrafish embryo developmental toxicity test

In order to assess the developmental toxicity, the experiments used embryos at 6 hpf with two or three replicates per exposure group and 10–15 fertilized eggs per replicate. Also, after the initial exposure once every 2 days the test solutions were refreshed. The biological defects rate was computed using the unhatched eggs and dead and abnormal larvae calculations, which were recorded during the experimental period [biological defects = (unhatched egg + total dead larvae + surviving abnormal larvae) / (initial count)]. Microscopy was performed at approximately 48, 72, 96, 120, 144, and 168 hpf. after YCl_3 and $AlCl_3$ exposure in order to monitor developmental toxicity.

6.2.6 Examination of heart function

In the experiment, for heartbeat counts at 48, 72, and 96 hpf. The control group constituted of wild type zebrafish. From each group, the number of 15 s heartbeats was counted in five zebrafish

6.2.7 Statistical analysis

For zebrafish embryos treated with $MgCl_2$, $ZnCl_2$, $CaCl_2$, YCl_3, and $AlCl_3$ the study generated sigmoidal dose-response curves. The post hoc Student-Newman-Keuls test was used to assess the combined effects of the mixtures, and this was preceded by use of SigmaPlot v.12.5 software (Systat, San Jose, CA, USA) for one-way variance analysis. The data is presented as the mean and ± standard error of mean with the statistical significance of $p < 0.05$.

6.3 Results and Discussion

6.3.1 Effects of $MgCl_2$, $ZnCl_2$, and $CaCl_2$ *in vitro* and in a zebrafish model

These studies evaluated Huh7 hepatocytes, HUVEC, and HL-1 cardiac muscle-like cells treated with Mg^{2+}, Zn^{2+}, and Ca^{2+} for 12 h for viability. Treatment with Mg^{2+} up to 48 mM, failed to show any significant impact on the relative viability of HL-1 and Huh7 cells after which, viability decreased to 67.49% ± 4.00% at 64 mM and 61.80% ± 13.85% at 128 mM as shown in Figure 6.2 (a). The study observed an increased sensitivity in HUVEC compared to the other cell types where relative viability to control was reduced from 103.22% ± 0.58% to below 44.44% ± 0.34% with increasing Mg^{2+} concentration from 16 to 64 mM. The viability profiles of all cell types did not show any significant impact of Zn^{2+} treatment as the viability sustained above the baseline value (100%) at up to 125 μM concentrations and reduced at a concentration higher than 250 μM (Figure 6.2 (a)). For instance, for cells exposed to 250 μM Zn, the viability was 88.87% ± 0.94%, 59.50% ± 11.52%, and 64.36% ± 5.30% for HL-1 and Huh7 cells and HUVEC, respectively. Similarly, the viability showed a decrease in Ca^{2+} exposed cells at concentrations of 48, 32, and 16 mM for HL-1 and Huh7 cells and HUVEC, respectively (Figure 6.2 (a)).

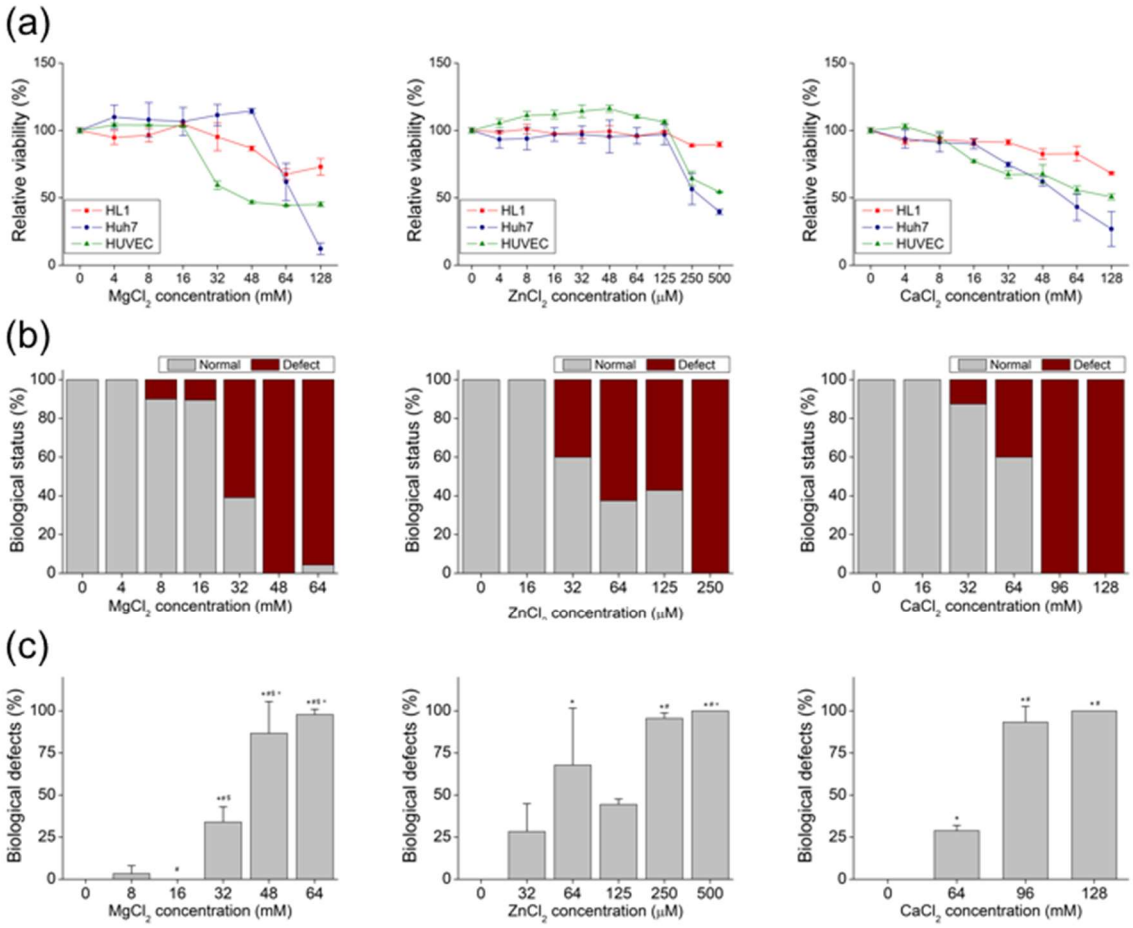


Figure 6.2. Evaluation of biological effect from increasing concentration of Mg, Zn, and Ca ions. (a) in vitro cellular viability of HL-1, Huh7 and HUVEC after treatment with different concentration of Mg, Zn, and Ca ion solution for 12 h. (b) Biological status of Zebrafish embryos (normal or defects) at 6 hpf after treatment with indicated concentration of Mg, Zn and Ca ion solutions. (c) Biological defects rate in Zebrafish embryos at 6 hpf after treatment with indicated concentration of Mg, Zn and Ca ion solutions.

**, #, &, and +, Significant difference vs. 0, 8, 16, and 32 mM Mg^{2+} ion, respectively.*

**, #, &, and +, Significant difference vs. 0, 32, 64, and 125 μM Zn^{2+} ion, respectively.*

** and #, Significant difference vs. 0 and 64 mM Ca^{2+} ion, respectively.*

To identify the *in vivo* biological impact of Mg, Zn, and Ca ions released from the biodegradable metal, zebrafish embryos were exposed to increasing $MgCl_2$, $ZnCl_2$, and $CaCl_2$ concentrations at 6 hours post fertilization (hpf). Biological defects were identified in the form of unhatched eggs and dead or abnormal larvae. Initially, the experiments used the concentration ranges identical to the *in vitro* cell viability assay. Groups which were exposed to 8 mM $MgCl_2$ started to show biological defects and embryos with biological defects reached 100% at 48 mM or higher concentrations (Figure 6.2 (b), (c)). Moreover, the biological defects started to emerge at 32 μM in $ZnCl_2$ exposed groups and at concentrations greater than 250 μM reached 100%. It was also observed that biological defects appeared in $CaCl_2$ presence at 64 mM with 128 mM and higher concentrations showing 100% occurrence of biological defects (Figure 6.2 (b), (c)). Thus, these results reflect the findings from *in vitro* studies and show that high concentration of Mg, Zn, and Ca ions can impair the growth of cells. During the embryo development process, blood vessels and heart are among the first organs to be exposed to foreign substances. As such, the experiments evaluated the embryonic defects in these tissues post exposure to alloying elements. This was achieved with the use of vasculature (Tg (flk1: EGFP)) and cardiac (Tg (cmlc2: EGFP)) transgenic zebrafish lines that express EGFP at the surface of blood vessels and cardiac tissue. This experiment used ion concentrations that showed 100% biological defects in the experiments conducted previously (64 mM, 500 μM, and 128 mM of Mg, Zn and Ca, respectively). The embryos treated with $MgCl_2$ showed normal blood vessels during development, and in contrast $ZnCl_2$ and $CaCl_2$ treated embryos showed abnormalities as presented in Figure 6.3 (a). Abnormal heart

phenotypes were only observed in those Tg (cmlc2: EGFP) zebrafish embryos treated with 128 mM $CaCl_2$ (Figure 6.3 (b)). The impact on cardiac function was evaluated by counting the heartbeat at 72 and 96 hpf. A decreased heart rate was evidenced in embryos treated with increasing concentration of Mg, Ca, and Zn in comparison to control groups (Figure 6.3 (c)) and specifically, in embryos with $CaCl_2$ exposure showed most significant decreases in heartbeats (Table 1). As shown in the results from Chapter 3 and Figure 6.2 of this chapter, the viability of various cells exposed to Mg, Zn and Ca ions showed similar toxicity to validate the effectiveness of Zebrafish model. These outcomes indicate that the intake of biocompatible metallic ions affect the vascular system and expedited deterioration of heart function at a similar toxic dosage found from *in vitro* results. The detoxification of harmful substances from the body is performed by the liver and correspondingly, the Tg (lfabp: DsRed) zebrafish line that expresses RFP specifically in the liver was utilized to examine $MgCl_2$, $ZnCl_2$, and $CaCl_2$ impact on liver development (Figure 6.3 (d), (e)). This experiment analysed the relative size of the liver in order to identify the defects. Compared to the control, the results showed a decrease by 55.82% ± 2.06%, 55.66% ± 20.07%, and 13.52% ± 4.89% at 96 hpf in the presence of $MgCl_2$ (64mM), $ZnCl_2$ (500 μM), and $CaCl_2$ (128mM), respectively. As illustrated in Figure 6. 3 (e), Tg (lfabp: RFP) embryos treated with the various ions were examined by fluorescence microscopy in order to confirm the decrease. Notably, results reflected the indications of cell viability experiments and the biological defects were found to be induced at similar or slightly lower concentrations for relatively biocompatible Mg, Zn and Ca ions (Table 2).

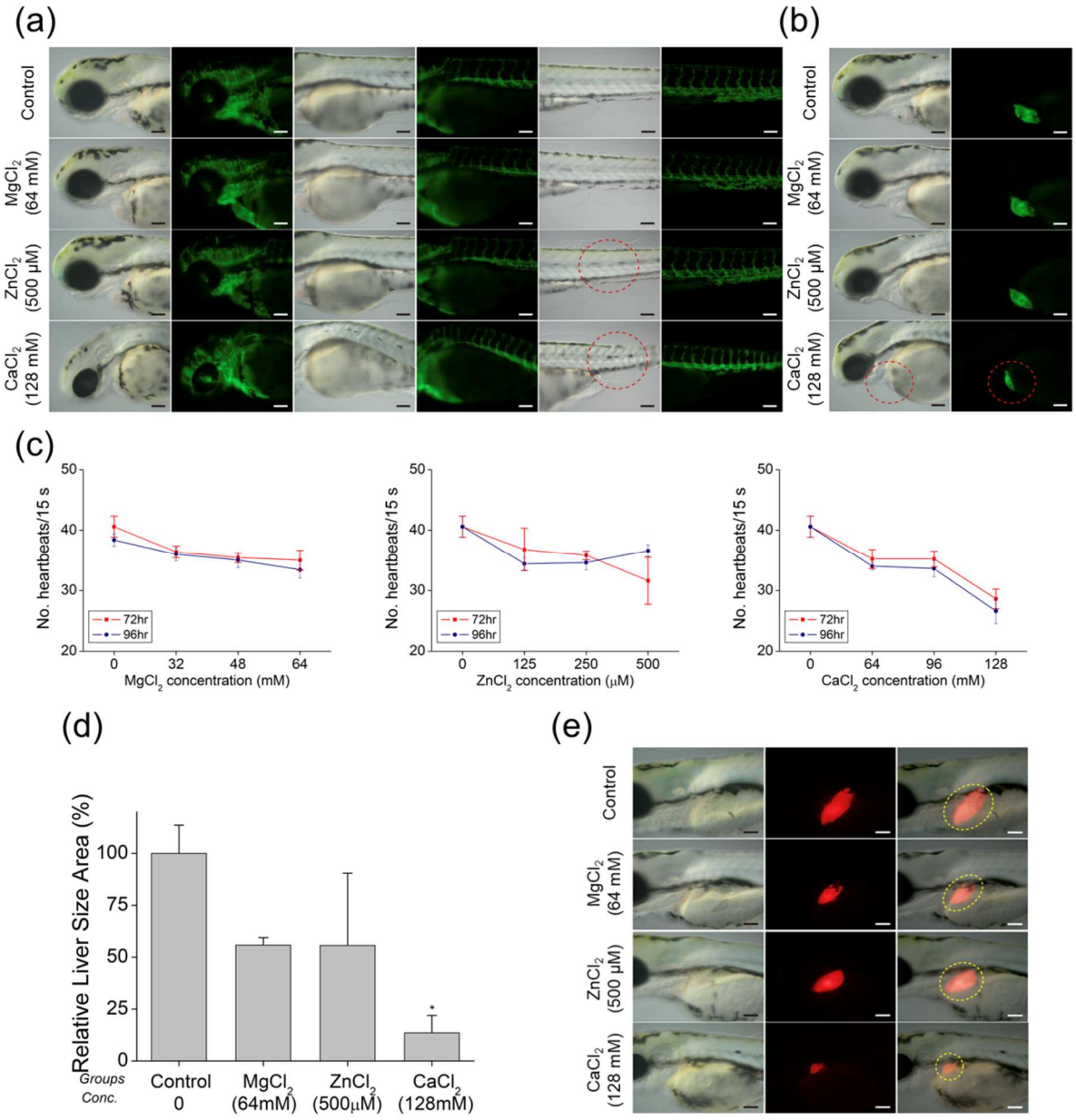


*Figure 6.3. (a) Biological defects from ion treated Zebrafish embryos at 72 hpf (b) The change in the heart size of ion treated Zebrafish embryos after 96 hpf. (c) The heart rate of zebrafish embryos subsequent to 72 and 96 hpf treatments with increasing concentrations of Mg, Zn, and Ca ions. (d) Relative liver size area of zebrafish embryos after treatment with 64 mM Mg. 500 μM Zn, and 128 mM Ca ions. (e) The change in liver size of ion-treated zebrafish embryos at 96 hpf. Scale bars, 100 μm. * indicates significant difference compared to Control ($p < 0.05$)*

		48 hpf	72 hpf	96 hpf
Control		38.55 ± 1.88	42.90 ± 2.80	42.60 ± 4.29
$MgCl_2$	32 mM	-	36.40 ± 1.02	36.00 ± 1.95
	48 mM	-	35.40 ± 0.80	35.00 ± 1.26
	64 mM	-	35.00 ± 1.67	33.40 ± 1.36
$ZnCl_2$	125 µM	-	36.80 ± 3.54	34.40 ± 1.02
	250 µM	-	35.80 ± 0.75	34.60 ± 1.20
	500 µM	-	31.60 ± 3.88	36.60 ± 1.02
$CaCl_2$	64 mM	-	35.20 ± 1.60	34.00 ± 0.63
	96 mM	-	35.20 ± 1.33	33.60 ± 1.36
	128 mM	-	28.60 ± 1.62	26.60 ± 2.06
YCl_3	5 µM	33.60 ± 0.80	40.40 ± 1.02	41.00 ± 0.89
	10 µM	32.60 ± 0.49	39.40 ± 1.74	39.20 ± 0.98
	25 µM	31.80 ± 0.98	39.60 ± 1.62	39.00 ±0.89
	50 µM	25.40 ± 1.96	24.80 ± 0.75	27.00 ± 1.67
$AlCl_3$	2.5 µM	41.00 ± 1.55	42.80 ± 0.75	43.60 ± 1.02
	5 µM	39.40 ± 0.49	41.60 ± 1.20	42.00 ± 1.67
	10 µM	38.80 ± 0.98	40.20 ± 0.98	41.80 ± 0.98
	25 µM	38.20 ±0.98	38.80 ± 0.98	39.00 ± 1.26

Table 1. Measured heartrate per 15 second after treatment with different concentration of Mg, Zn, Ca, Y, Al ions 48, 72 and 96 hpf

		Live embryos (%)	Abnormal development (%)	Not hatched (%)	Cardiac edema (%)	Shortage (%)	Bent tail (%)
Control		100	-	-	-	-	-
$MgCl_2$	8 mM	96.67 ± 4.71	-	-	-	-	-
	16 mM	100	-	-	-	-	-
	32 mM	70.63 ± 7.12	2.38 ± 3.37	-	2.22 ± 3.14	-	-
	48 mM	26.67 ± 37.71	11.11 ± 3.14	-	-	-	2.22 ± 3.14
	64 mM	2.22 ± 3.14	-	-	-	-	-
$ZnCl_2$	32 µM	100	15.00 ± 16.50	-	-	-	13.33 ± 18.86
	64 µM	97.78 ± 3.14	27.22 ± 31.34	-	-	-	38.33 ± 37.04
	125 µM	88.89 ± 3.14	2.22 ± 12.57	-	-	-	31.11 ± 3.14
	250 µM	20.00 ± 18.85	6.66 ± 9.42	-	-	-	8.88 ± 8.31
	500 µM	0	-	-	-	-	-
$CaCl_2$	64 mM	97.77 ± 3.14	26.66 ± 11.33	-	-	-	-
	96 mM	62.22 ± 44.00	55.56 ± 44.00	-	-	-	-
	128 mM	0	-	-	-	-	-
YCl_3	5 µM	91.11 ± 8.31	-	-	13.89 ± 14.16	-	21.66 ± 16.50
	10 µM	70.56 ± 15.89	-	-	9.44 ± 2.83	-	22.22 ± 15.71
	25 µM	54.44 ± 38.52	-	-	15.00 ± 10.80	-	12.78 ± 10.21
	50 µM	43.89 ± 31.63	-	-	32.78 ± 30.44	-	13.89 ± 14.16
$AlCl_3$	2.5 µM	97.22 ± 4.81	-	-	-	-	-
	5 µM	86.67 ± 18.85	-	20.00 ± 12.57	8.89 ± 12.57	-	32.22 ± 12.86
	10 µM	70.56 ± 26.40	-	17.78 ± 8.31	4.44 ± 6.28	-	27.22 ± 11.57
	25 µM	23.89 ± 24.96	-	15.55 ± 13.70	4.44 ± 6.28	17.22 ± 12.20	11.11 ± 8.31

Table 2. Detailed recorded biological defects from increasing concentration of alloying elements

6.3.2 Biological effects of YCl_3 *in vitro* and in a zebrafish model

The cellular viability of Huh7, HUVEC, and HL-1 subsequent to 12 h exposure to increasing concentrations of Y^{3+} ion was found to be unaltered at up to 25 μM concentrations in all groups. However, a marked viability reduction was seen at 200, 50, and 100 μM for HL-1 and Huh7 cells and HUVEC, respectively. The zebrafish embryos were subjected to varying YCl_3 (5 μM to 4 mM) concentrations in order to evaluate the biological effect of Y released from a biodegradable Mg alloy. The experiment demonstrated the observation of biological defects in the 5 μM treatment group, and as shown in Figure 6. 4 (b) and (c), this occurrence reached 100% in embryos treated with higher dosage than 50 μM. In order to observe the effect of Y on cardiac tissue and vessels the experiments utilized the Tg (flk1: EGFP) and Tg (cmlc2: EGFP) zebrafish lines. Correspondingly, Figure 6.4 (d) explicates the emergence of biological defects. The heart defects were observed in embryos treated with 25 μM YCl_3 and embryos exposed to 50 μM showed cardiac edema and a bent tail. Significant cardiac abnormalities, including delayed heart development and a reduced heart rate are seen on a closer examination as represented in Figure 6.4 (e). In the presence of 50 μM YCl_3, a marked heart rate decrease was observed in particular, which is closely related to cardiac function. Hence, introducing YCl_3 into a living organism at concentrations greater than 25 μM could lead to heart function deterioration, blood vessel defects, and diminished heart rate. Between Tg (lfabp: DsRed) embryos treated with 25 μM YCl_3 and control groups at 96 and 168 hpf, the liver size showed negligible difference.

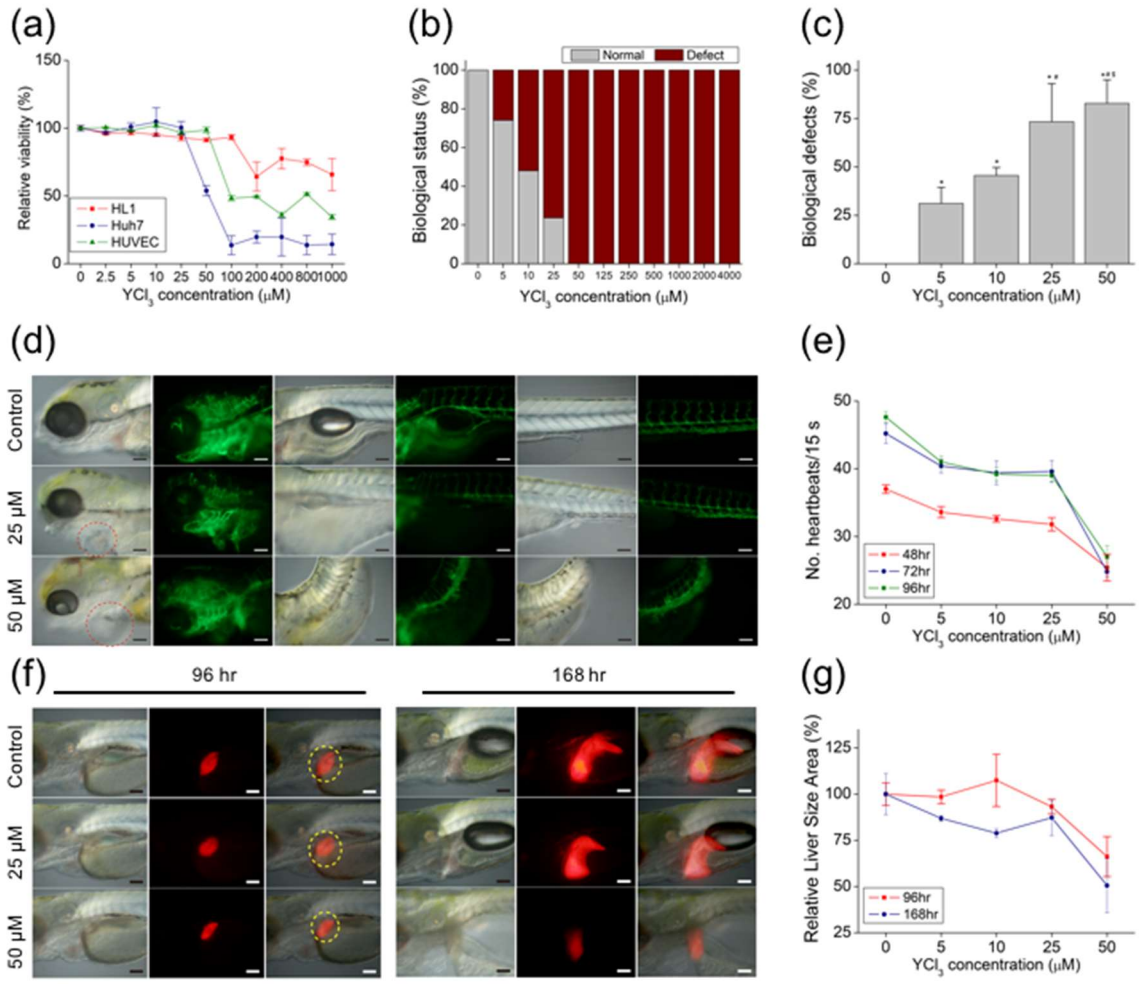


*Figure 6. 4. (a) Cellular viability of HL-1, Huh7, and HUVEC after treatment of Mg, Zn, and Ca ion solutions for 12 h. (b) Biological status of Zebrafish embryos (normal or defects) at 6 hpf after treatment with indicated concentration of Y ion solutions. (c) Biological defects rate in Zebrafish embryos at 6 hpf after treatment with indicated concentration of Y ion solutions. (d) Biological defects from ion treated Zebrafish embryos at 72 hpf. (e) The heart rate of zebrafish embryos subsequent to 72 and 96 hpf treatments with increasing concentrations of Y ions. (f) The change in liver size of ion-treated zebrafish embryos at 96 and 168 hpf. (e) Relative liver size area of zebrafish embryos after treatment of Y ions 96 hpf and 168 hpf. Scale bars, 100 μm. $^{+}$. *, #, &, and +, Significant difference vs. 0, 5, and 10 μM Y^{3+} ion, respectively*

However, the embryos treated with 50 μM YCl_3 resulted in significantly reduced liver size of 66.20% ± 6.23% at 96 hpf and 50.58% ± 8.49% at 168 hpf. Figure 6.4 (f) and (g) illustrate the morphological and phenotypic analyses to suggest that Y ions are tolerated up to a concentration of 25 μM. According to previously reported *in vitro* studies on toxic concentration of yttrium ions, cells started to show toxicity at concentrations of 1 mM or higher (Zhao and Zhu 2015). While the *in vitro* result from this study is in good agreement with the previously reported studies, *in vivo* Zebrafish evaluation of yttrium ion showed toxicity at much lower concentration. The biological defects were induced at significantly lower concentrations of 5 μM and reached 100% defect at 50 μM.

6.3.3 Biological effects of $AlCl_3$ in a zebrafish model

As presented in Figure 6.5 (a), the HL-1, Huh7, and HUVEC viability showed a decrease to 64.25% ± 10.72%, 47.88% ± 6.74%, and 76.19% ± 0.14% at $AlCl_3$ concentrations of 200, 100, and 400 μM, respectively. Interestingly, the biological defects in zebrafish embryos started to emerge in the 2.5 μM $AlCl_3$ and reached 100% at concentration higher than 25 μM (Figure 6.5 (b), (c)).

The Tg (flk1: EGFP) and Tg (cmlc2: EGFP) zebrafish lines were used to evaluate the Al ions effect on the circulatory system. A bent trunk phenotype was evidenced in embryos treated with 25 μM of $AlCl_3$ with an abnormal morphology due to the disorganized overall tissue structure as seen in Figure 6.5 (d). Despite the absence of any heart deformities, the heart rate showed a decline which followed a

concentration- and treatment time-dependent manner (Figure 6.5 (e)). According to the results, Al was shown to induce vascular defects and reduce cardiac function, even at an exceptionally low concentration. The Tg (lfabp: DsRed) zebrafish expressing RFP in the liver were subjected to variable $AlCl_3$ concentrations, with the objective to investigate the $AlCl_3$ impact on liver development. As seen in Figure 6. 5 (g), Al concentration of 10 and 25 μM decreased liver size to 36.43% ± 3.63% and 41.5% ± 3.55%, respectively, at 96 hpf and subsequently performed microscopic examination confirm the same trend (Figure 6.5 (f)). Moreover, the Tg (GFAP: EGFP) and Tg (olig2: DsRed) transformation zebrafish model was used *in vivo* for assessment of Al on neuronal growth. However, as seen in Figure 6.6, neurogenesis was not impacted by Al. According to previous cell viability studies (Zhao and Zhu 2015), $AlCl_3$ has been shown to induce toxicity at 800 μM or higher concentrations. In contrast, the *in vivo* results of the current study showed biological defects at a significantly lower 5 μM $AlCl_3$.

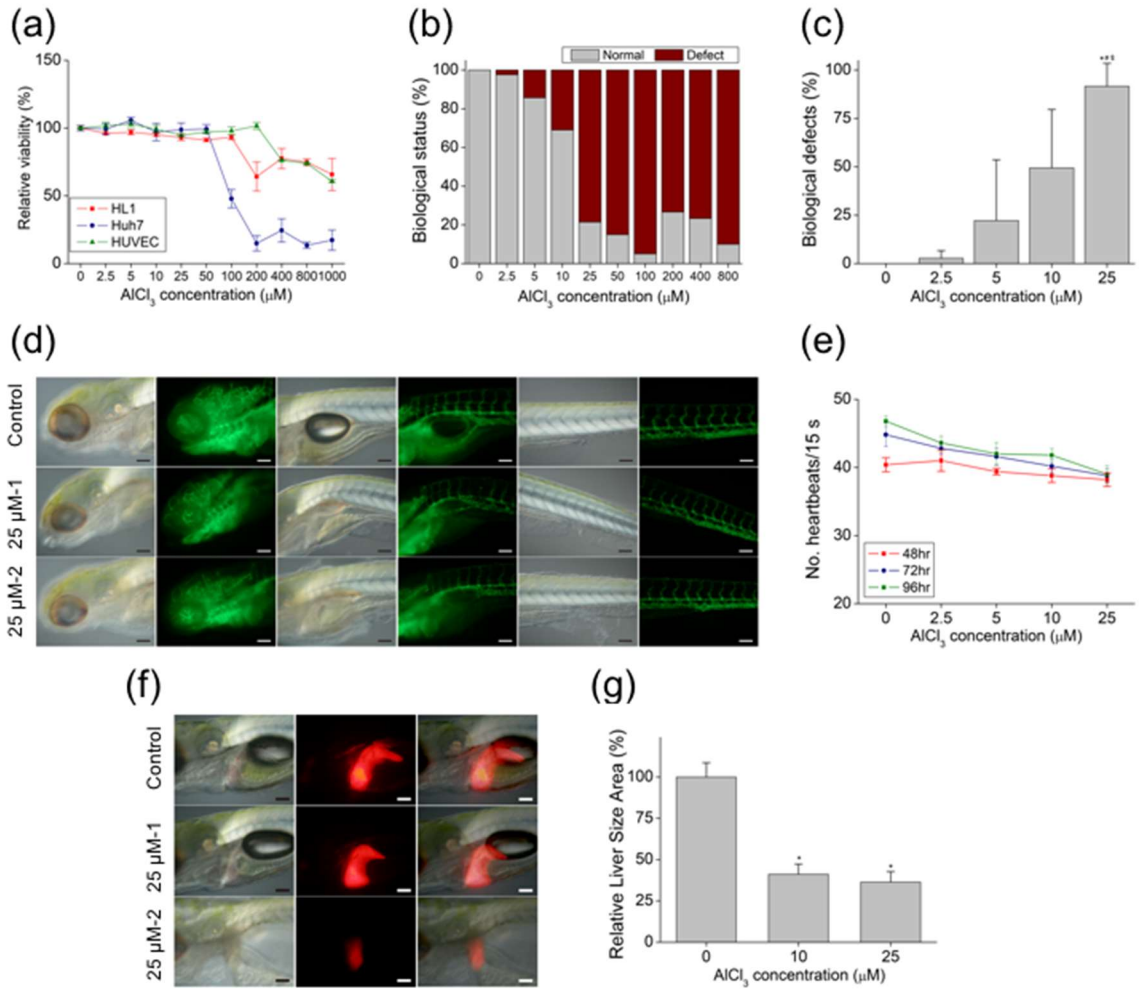


*Figure 6. 5. Biological effect of Al^{3+} in vitro and in a zebrafish model. (a) Viability of HL-1 and Huh7 cells and HUVEC after treatment with indicated ion solutions for 12 h. (b) Biological status of embryos (normal or defects) at 6 hpf after treatment with indicated ion solutions. (c) Biological defects in embryo at 6 hpf after treatment with indicated ion solutions. (d) Representative images of ion-treated zebrafish embryo used to determine heart rate. (e) Mean heart rate of zebrafish embryos following 48-, 72-, and 96-h treatments with different concentrations of Al^{3+}. (f) Representative images of ion-treated zebrafish embryo used to determine liver size at 96 and 168 hpf. (e) Mean liver size of zebrafish embryos following 96-and 168-h treatments with indicated concentrations of Al^{3+}. *, #, &, and +, Significant difference vs. 0, 2.5, and 5 μM of Al^{3+}, respectively. Scale bars, 100 μm.*

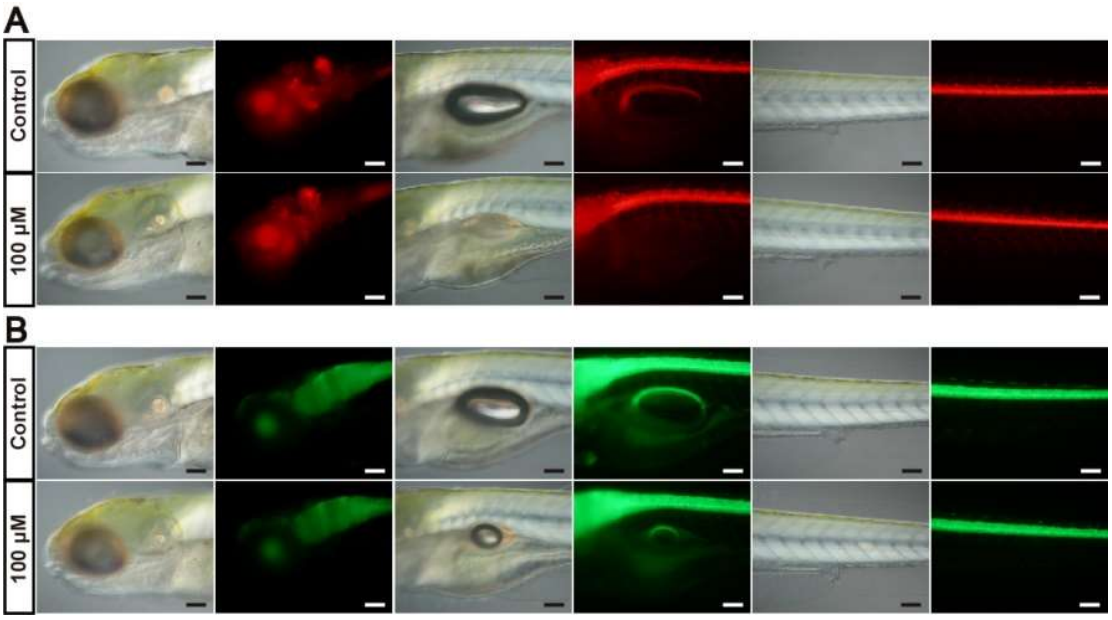


Figure 6.6. Evaluation of Al ion on neuronal growth A) Tg(olig2:DsRed) zebrafish treated with 100 µM of Al ion after 144 hpf. B) Tg(GFAP:EGFP) zebrafish treated with 100 µM of Al ion after 144hpf. Scale bars, 100 µm.

6.4 Conclusion

In the past decade, several studies have highlighted the usage of osteoblasts, macrophages, fibroblasts, and endothelial cells to assess the biocompatibility of biodegradable Mg alloys (Tie, Feyerabend et al. 2013, Liu, Fu et al. 2016, Mousa, Hussein et al. 2016, Kim, Han et al. 2017). Such extensive studies have resulted in variable cell viability rates and it has been revealed that some cell types exhibit much more resilience to toxic ions in comparison to living tissues. Presumably, more reliable biocompatibility data has been generated through *in vivo* studies. However, such *in vivo* studies have been limited due to the high cost and longer observation time involved in the development and evaluation process of biodegradable Mg alloy. To this end, the transgenic zebrafish serves as a useful *in vivo* model through facilitation of a direct observation of developmental defects in specific organs that are caused by exposure to released alloying elements (He, Gao et al. 2014, Kanungo, Cuevas et al. 2014). The evaluation of relatively biocompatible elements Mg, Zn, and Ca reflected the findings of *in vitro* assay to confirm the validity of this model. Furthermore, elements such as yttrium and aluminium are frequently utilized to increase corrosion rate and mechanical strength despite the hepatotoxicity of yttrium as studied by Su, Mackey et al. (2017) and aluminium's links to Alzheimer's disease (Geyikoglu, Turkez et al. 2013). Studies have highlighted the safety of these alloys through cellular viability experiments and emphasize that the released concentration of ions are not substantial to cause harm in living tissue. Results from this

investigation, however, explicate the *in vivo* biological responses which occur at significantly lower concentrations when compared to the previously reported results of conventional *in vitro* cellular assays.

Utilization of the zebrafish embryo model allows accurate, efficient and fast observation of *in vivo* toxicity of new biodegradable alloy systems. This method can be further optimized to test the media extracts from the degrading alloys to observe the real-time toxicity of degrading particles.

Chapter 7

Conclusions and Future Work

7.1 Conclusions

The concept of an implantable device which replaces the missing or damaged tissue dates back almost four thousand years to ancient Egypt where a functional wooden toe was used to replace a missing right big toe (Nerlich, Zink et al. 2000). With the huge advancements in metallurgy, countless studies in the last decade have provided a foundation for the successful application of biodegradable metals in bone replacement by controlling their mechanical and corrosion properties. These devices would degrade in the physiological environments once their goal is achieved and overcome the limitations of the bioinert implantable materials, thereby generating step-change in orthopaedic technology. Even after more than a decade of focused research on the development process, there are still a series of hurdles which must be addressed before these materials can be safely deployed in a clinical setting. This study explored the biological response to a novel biodegradable Mg5Ca1Zn alloy developed for orthopaedic repair and evaluated the bone remodelling process to assess the potential of the new implant.

Chapter 3 described the impact of Mg alloy biodegradation on the cells associated with the progression of bone regeneration through a series of comprehensive *in vitro* evaluations using released ions from pure Mg and Mg5Ca1Zn alloy. Result showed an overall improvement in osteogenesis through released metal ions at similar rates from both pure Mg and Mg alloy extracts which indicates an optimal stimulation of the initial phases of the bone formation process from the released metal ions. These findings also indicate that bone tissue regeneration can be facilitated through reduced osteoclastic activity by released metal ions from Mg alloy at the implant site. Chapter 4 explored the benefit of a 3D dynamic culture system and the osteogenic effect of released metallic ions from Mg5Ca1Zn were confirmed in 3D culture conditions. A conventional 2D culture system does not accurately portray the 3D *in vivo* environment when investigating the effects of biodegradable metals and where the corrosion profile depends heavily on the local environments. The key aspects of *in vivo* physiological conditions such as blood flow-induced magnesium corrosion, hydrogen evolution, and local pH change were simulated for the accurate evaluation of newly developed biodegradable materials. Recapitulation of an *in vivo*-like environment with flow-induced loading resulted in a statistically significant increase in proliferation and differentiation for all of the tested materials. The released ions from both Mg5Ca and Mg5Ca1Zn alloy showed positive effects on the progress of bone formation. However, fast corroding Mg5Ca showed detrimental effects on osteoblast cells, whereas osteoblast proliferation and differentiation were improved by released metal ions from the Mg5Ca1Zn alloy with much slower corrosion rates.

These findings suggested that the release of metal ions consisting of Mg, Ca and Zn also sufficiently stimulate osteoblasts.

Chapter 5 utilized several state-of-the-art techniques to observe the early phases of bone formation and matrix deposition around the biodegradable Mg5Ca1Zn alloy. The results suggest that the particles released by the degrading Mg alloy will confer a favourable effect within the bone microenvironment leading to increased number of blood vessels growth which in turn is followed by favourable osteogenesis. The *in vitro* assays and fetal mouse metatarsal assay validated the positive effect of released metallic particles on angiogenesis and SHG imaging showed an excellent deposit of collagen matrix on the implantation site of Mg5Ca1Zn. These results were validated with immunostained slides that showed good contact between newly generated collagen tissues and the degrading surface of the Mg5Ca1Zn sample. The findings from this chapter demonstrate that Mg5Ca1Zn samples facilitates optimal bone healing process by releasing metallic ions into the surrounding tissues to enhance the growth of blood vessels and actively recruiting osteoprogenitors near the implant site at a degradation rate acceptable for the tissue.

In summary, all of the experimental results have demonstrated that the optimized mechanical properties and corrosion rate of Mg5Ca1Zn alloy leads to release of metallic Mg, Ca and Zn ions at a rate that facilitate both angiogenesis and coupled osteogenesis for better bone healing without causing adverse effect at the implantation site.

Chapter 6 explores at limitation of current *in vivo* studies involved in the development and evaluation process of biodegradable Mg alloy. The use of transgenic zebrafish to

allow for a direct observation of developmental defects in specific organs was proposed as a new *in vivo* model for evaluation of Mg alloy. The evaluation of relatively biocompatible elements Mg, Zn, and Ca reflected the findings of *in vitro* assays to confirm the validity of the model. In addition, the study results from well-known toxic elements Y and Al explicate the *in vivo* biological responses to occur at significantly lower concentration when compared to the previously reported results of conventional *in vitro* cellular assays. Thus, utilization of a zebrafish embryo model allows accurate, efficient and fast observation of *in vivo* toxicity of new biodegradable alloy systems.

Compared to the conventional corrosion resistant materials used in orthopaedics, the research on biodegradable metals is currently in its infancy, with wide scope for innovation. Overall, I strongly believe that the currently ongoing development and refinement of biodegradable metal systems will act as a crucial portal technology to revolutionize a myriad of clinical applications in the near future.

7.2 Future work

This research assessed the potential of the biodegradable Mg5Ca1Zn alloy system for orthopaedic applications and confirmed the favourable bone healing conditions provided by the degrading implant. Various results from this study was used to support the process of obtaining the CE mark in 2018 which will allow the clinical trials and applications throughout Europe. In fact, the first clinical trial of Mg5Ca1Zn screw for small hand and wrist fracture in Europe is scheduled for the first quarter of 2019. However, this alloy system does not offer a solution for the treatment of fractures that require substantial amount of load bearing such as hip, femur, tibia and spine. This section addresses the limitation of the study and discusses the future direction of the research for biodegradable metals.

The main challenge of future works involves the design of the biodegradable alloy system. The current Mg5Ca1Zn alloy system has relatively high UCS (~380 MPa), UTS (~ 250 MPa), YS (~190 MPa) and good ductility (~10%) which is deemed enough for treatment of small fractures in skull, hand, foot and wrist. However, treatment of larger bone fractures would require a biodegradable metal system with much higher mechanical properties to guarantee the safe applications without implant failure. The most challenging aspect of alloy system optimization and revision process is the limited composing elements in the clinically approved alloy system. As mentioned in Chapter 2, alloying with Al or other rare earth elements would drastically increases the mechanical properties of the biodegradable metals. The

biocompatibilities of such elements, however, are known to be toxic and it would require years of work just to prove the safety of newly developed material. For some countries, the governing agencies rejects the approval of implantable materials consisting any elements with previously known toxicity. For this reason, it is crucial to work only with the biocompatible elements when developing new implantable materials. Following the clinical approval of Mg5Ca1Zn alloy system, the influence of Ca and Zn on biodegradation, microstructure and mechanical properties has been thoroughly investigated to develop the second-generation alloy system with higher mechanical properties. Controlling the number of secondary phases and balanced element composition resulted in a significant increase in mechanical properties, and the prototypes of second-generation implants are currently being tested through series of *in vitro* and *in vivo* experiments.

The application of perfusion bioreactor culture system allowed this study to overcome the limitation of the conventional 2D culture system which does not accurately portray the key aspects of *in vivo* physiological conditions such as blood flow-induced magnesium corrosion, hydrogen evolution, and local pH change. Further biological characterization should be undertaken using the perfusion bioreactor system to study the effect of released ions on osteoclasts and immune cells. Such study will allow further optimization of 3D culture system for *in vitro* testing of biodegradable metals and show the complete picture of bone formation effect from released ions of Mg5Ca1Zn.

The usage of SHG needs be explored further to optimize a technique to observe collagen structure around the degrading Mg alloy implant without requiring the

staining procedure. The staining of the section often results in damaged tissue due to hydrogen gas formation and the use of SHG will prevent such damages from the active biodegradation. Current study showed that the expression level of fibrillar collagen was higher in dynamic culture conditions for all the tested materials. However, it was not possible to identify the exact type of detected collagens through SHG alone and if available, such information could be used to distinguish between the normal bone healing and abnormal fibrosis. Study by Ranjit et al. (2015) have shown the separation of different collagen types using SHG and fluorescence lifetime imaging (FLIM). FLIM was used to separate the collagen I from collagen III in mouse femur and the same technique could be utilized for analysis of biodegradable metals.

In addition, utilization of a zebrafish embryo model could be further optimized to test the degrading implant sample in the media instead of different metallic ions diluted in the media. Current zebrafish testing kits did not allow the observation of real time degradation from implant samples without damaging the embryos. As mentioned before, there are several changes to the local environment during degradation of Mg alloy and development of such kit would enable more accurate and rapid *in vivo* toxicity testing of newly developed biodegradable alloy systems.

Bibliography

Acklin, Y. P., C. Michelitsch and C. Sommer (2016). "Elective implant removal in symptomatic patients after internal fixation of proximal humerus fractures improves clinical outcome." Bmc Musculoskeletal Disorders **17**.

Ajai Singh, S. A., RN Srivastava, NS Verma (2012). "Immunological Response to Post-trauma Bone Remodeling." Journal of Postgraduate Medicine **46**(3): 148-151.

Alvarez-Barreto, J. F., S. M. Linehan, R. L. Shambaugh and V. I. Sikavitsas (2007). "Flow perfusion improves seeding of tissue engineering scaffolds with different architectures." Ann Biomed Eng **35**(3): 429-442.

Alves, M. M., T. Prosek, C. F. Santos and M. F. Montemor (2017). "Evolution of the in vitro degradation of Zn-Mg alloys under simulated physiological conditions." RSC Advances **7**(45): 28224-28233.

Angrisani, N., J. Reifenrath, F. Zimmermann, R. Eifler, A. Meyer-Lindenberg, K. Vano-Herrera and C. Vogt (2016). "Biocompatibility and degradation of LAE442-based magnesium alloys after implantation of up to 3.5 years in a rabbit model." Acta Biomaterialia **44**: 355-365.

Arnett, T. R. (2008). "Extracellular pH regulates bone cell function." Journal of Nutrition **138**(2): 415s-418s.

Arnett, T. R. (2010). "Acidosis, hypoxia and bone." Arch Biochem Biophys **503**(1): 103-109.

Bachoura, A., R. Yoshida, C. Lattermann and S. Kamineni (2012). "Late removal of titanium hardware from the elbow is problematic." ISRN Orthop **2012**: 256239.

Balga, R., A. Wetterwald, J. Portenier, S. Dolder, C. Mueller and W. Hofstetter (2006). "Tumor necrosis factor-alpha: Alternative role as an inhibitor of osteoclast formation in vitro." Bone **39**(2): 325-335.

Barnes, G. L., P. J. Kostenuik, L. C. Gerstenfeld and T. A. Einhorn (1999). "Growth Factor Regulation of Fracture Repair." Journal of Bone and Mineral Research **14**(11): 1805-1815.

Bastian, O., J. Pillay, J. Alblas, L. Leenen, L. Koenderman and T. Blokhuis (2011). "Systemic inflammation and fracture healing." J Leukoc Biol **89**(5): 669-673.

Benjamin, D. C. and R. O. Hynes (2017). "Intravital imaging of metastasis in adult Zebrafish." Bmc Cancer **17**.

Berghmans, S., C. Jette, D. Langenau, K. Hsu, R. Stewart, T. Look and J. P. Kanki (2005). "Making waves in cancer research: new models in the zebrafish." Biotechniques **39**(2): 227-237.

Biber, R., J. Pauser, M. Brem and H. J. Bail (2017). "Bioabsorbable metal screws in traumatology: A promising innovation." Trauma Case Reports **8**: 11-15.

Biber, R., J. Pauser, M. Gesslein and H. J. Bail (2016). "Magnesium-Based Absorbable Metal Screws for Intra-Articular Fracture Fixation." Case Rep Orthop **2016**: 9673174.

Bohner, M. (2010). "Resorbable biomaterials as bone graft substitutes." Materials Today **13**(1-2): 24-30.

Bostman, O. and H. Pihlajamaki (2000). "Clinical biocompatibility of biodegradable orthopaedic implants for internal fixation: a review." Biomaterials **21**(24): 2615-2621.

Boyle, W. J., W. S. Simonet and D. L. Lacey (2003). "Osteoclast differentiation and activation." Nature **423**(6937): 337-342.

Brandao-Burch, A., J. C. Utting, I. R. Orriss and T. R. Arnett (2005). "Acidosis inhibits bone formation by osteoblasts in vitro by preventing mineralization." Calcif Tissue Int **77**(3): 167-174.

Carano, R. A. D. and E. H. Filvaroff (2003). "Angiogenesis and bone repair." Drug Discovery Today **8**(21): 980-989.

Cha, P. R., H. S. Han, G. F. Yang, Y. C. Kim, K. H. Hong, S. C. Lee, J. Y. Jung, J. P. Ahn, Y. Y. Kim, S. Y. Cho, J. Y. Byun, K. S. Lee, S. J. Yang and H. K. Seok (2013). "Biodegradability engineering of biodegradable Mg alloys: Tailoring the electrochemical properties and microstructure of constituent phases." Scientific Reports **3**.

Cha, P. R., H. S. Han, G. F. Yang, Y. C. Kim, K. H. Hong, S. C. Lee, J. Y. Jung, J. P. Ahn, Y. Y. Kim, S. Y. Cho, J. Y. Byun, K. S. Lee, S. J. Yang and H. K. Seok (2013). "Biodegradability engineering of biodegradable Mg alloys: tailoring the electrochemical properties and microstructure of constituent phases." Sci Rep **3**: 2367.

Chakraborty, C., A. R. Sharma, G. Sharma and S. S. Lee (2016). "Zebrafish: A complete animal model to enumerate the nanoparticle toxicity." Journal of Nanobiotechnology **14**.

Chaya, A., S. Yoshizawa, K. Verdelis, N. Myers, B. J. Costello, D. T. Chou, S. Pal, S. Maiti, P. N. Kumta and C. Sfeir (2015). "In vivo study of magnesium plate and screw degradation and bone fracture healing." Acta Biomaterialia **18**: 262-269.

Chen, Q. Z. and G. A. Thouas (2015). "Metallic implant biomaterials." Materials Science & Engineering R-Reports **87**: 1-57.

Chen, X., O. Nadiarynkh, S. Plotnikov and P. J. Campagnola (2012). "Second harmonic generation microscopy for quantitative analysis of collagen fibrillar structure." Nat Protoc **7**(4): 654-669.

Chen, Y., Z. Xu, C. Smith and J. Sankar (2014). "Recent advances on the development of magnesium alloys for biodegradable implants." Acta Biomater **10**(11): 4561-4573.

Chen, Y., S. Zhang, J. Li, Y. Song, C. Zhao and X. Zhang (2010). "Dynamic degradation behavior of MgZn alloy in circulating m-SBF." Materials Letters **64**(18): 1996-1999.

Cheng, J., T. Huang and Y. F. Zheng (2014). "Microstructure, mechanical property, biodegradation behavior, and biocompatibility of biodegradable Fe-Fe2O3 composites." Journal of Biomedical Materials Research Part A **102**(7): 2277-2287.

Cheng, P., P. Han, C. Zhao, S. Zhang, X. Zhang and Y. Chai (2016). "Magnesium inference screw supports early graft incorporation with inhibition of graft degradation in anterior cruciate ligament reconstruction." Sci Rep **6**: 26434.

Cheng, P. F., P. Han, C. L. Zhao, S. X. Zhang, H. L. Wu, J. H. Ni, P. Hou, Y. Z. Zhang, J. Y. Liu, H. D. Xu, S. Liu, X. N. Zhang, Y. F. Zheng and Y. M. Chai (2016). "High-purity magnesium interference screws promote fibrocartilaginous entheses

regeneration in the anterior cruciate ligament reconstruction rabbit model via accumulation of BMP-2 and VEGF." Biomaterials **81**: 14-26.

Cho, S. Y., S.-W. Chae, K. W. Choi, H. K. Seok, H. S. Han, S. J. Yang, Y. Y. Kim, J. T. Kim, J. Y. Jung and M. Assad (2012). "Load-bearing capacity and biological allowable limit of biodegradable metal based on degradation rate in vivo." Journal of Biomedical Materials Research Part B: Applied Biomaterials **100B**(6): 1535-1544.

Cho, S. Y., S. W. Chae, K. W. Choi, H. K. Seok, Y. C. Kim, J. Y. Jung, S. J. Yang, G. J. Kwon, J. T. Kim and M. Assad (2013). "Biocompatibility and strength retention of biodegradable Mg-Ca-Zn alloy bone implants." Journal of Biomedical Materials Research Part B-Applied Biomaterials **101B**(2): 201-212.

Cho, T.-J., L. C. Gerstenfeld and T. A. Einhorn (2002). "Differential Temporal Expression of Members of the Transforming Growth Factor β Superfamily During Murine Fracture Healing." Journal of Bone and Mineral Research **17**(3): 513-520.

Christenson, E. M., K. S. Anseth, J. J. van den Beucken, C. K. Chan, B. Ercan, J. A. Jansen, C. T. Laurencin, W. J. Li, R. Murugan, L. S. Nair, S. Ramakrishna, R. S. Tuan, T. J. Webster and A. G. Mikos (2007). "Nanobiomaterial applications in orthopedics." J Orthop Res **25**(1): 11-22.

Cipriano, A. F., J. J. Lin, A. Lin, A. Sallee, B. Le, M. C. C. Alcaraz, R. G. Guan, G. Botimer, S. Inceoglu and H. N. Liu (2017). "Degradation of Bioresorbable Mg-4Zn-1Sr Intramedullary Pins and Associated Biological Responses in Vitro and in Vivo." Acs Applied Materials & Interfaces **9**(51): 44332-44355.

Deckers, M., G. van der Pluijm, S. Dooijewaard, M. Kroon, V. van Hinsbergh, S. Papapoulos and C. Lowik (2001). "Effect of angiogenic and antiangiogenic

compounds on the outgrowth of capillary structures from fetal mouse bone explants." Lab Invest **81**(1): 5-15.

Di Mario, C., H. Griffiths, O. Goktekin, N. Peeters, J. Verbist, M. Bosiers, K. Deloose, B. Heublein, R. Rohde, V. Kasese, C. Ilsley and R. Erbel (2004). "Drug-eluting bioabsorbable magnesium stent." J Interv Cardiol **17**(6): 391-395.

Diekmann, J., S. Bauer, A. Weizbauer, E. Willbold, H. Windhagen, P. Helmecke, A. Lucas, J. Reifenrath, I. Nolte and M. Ezechieli (2016). "Examination of a biodegradable magnesium screw for the reconstruction of the anterior cruciate ligament: A pilot in vivo study in rabbits." Materials Science & Engineering C-Materials for Biological Applications **59**: 1100-1109.

Ding, Y. F., C. E. Wen, P. Hodgson and Y. C. Li (2014). "Effects of alloying elements on the corrosion behavior and biocompatibility of biodegradable magnesium alloys: a review." Journal of Materials Chemistry B **2**(14): 1912-1933.

Dorozhkin, S. V. and M. Epple (2002). "Biological and medical significance of calcium phosphates." Angew Chem Int Ed Engl **41**(17): 3130-3146.

El-Rahman, S. S. (2003). "Neuropathology of aluminum toxicity in rats (glutamate and GABA impairment)." Pharmacol Res **47**(3): 189-194.

Erlebacher, A., E. H. Filvaroff, S. E. Gitelman and R. Derynck (1995). "Toward a molecular understanding of skeletal development." Cell **80**(3): 371-378.

Flicek, P., M. R. Amode, D. Barrell, K. Beal, K. Billis, S. Brent, D. Carvalho-Silva, P. Clapham, G. Coates, S. Fitzgerald, L. Gil, C. G. Giron, L. Gordon, T. Hourlier, S. Hunt, N. Johnson, T. Juettemann, A. K. Kahari, S. Keenan, E. Kulesha, F. J. Martin, T. Maurel, W. M. McLaren, D. N. Murphy, R. Nag, B. Overduin, M. Pignatelli, B.

Pritchard, E. Pritchard, H. S. Riat, M. Ruffier, D. Sheppard, K. Taylor, A. Thormann, S. J. Trevanion, A. Vullo, S. P. Wilder, M. Wilson, A. Zadissa, B. L. Aken, E. Birney, F. Cunningham, J. Harrow, J. Herrero, T. J. Hubbard, R. Kinsella, M. Muffato, A. Parker, G. Spudich, A. Yates, D. R. Zerbino and S. M. Searle (2014). "Ensembl 2014." Nucleic Acids Res **42**(Database issue): D749-755.

Gaspar, D. A., V. Gomide and F. J. Monteiro (2012). "The role of perfusion bioreactors in bone tissue engineering." Biomatter **2**(4): 167-175.

Geetha, M., A. K. Singh, R. Asokamani and A. K. Gogia (2009). "Ti based biomaterials, the ultimate choice for orthopaedic implants - A review." Progress in Materials Science **54**(3): 397-425.

Gerstenfeld, L. C., Y. M. Alkhiary, E. A. Krall, F. H. Nicholls, S. N. Stapleton, J. L. Fitch, M. Bauer, R. Kayal, D. T. Graves, K. J. Jepsen and T. A. Einhorn (2006). "Three-dimensional Reconstruction of Fracture Callus Morphogenesis." Journal of Histochemistry & Cytochemistry **54**(11): 1215-1228.

Gerstenfeld, L. C., D. M. Cullinane, G. L. Barnes, D. T. Graves and T. A. Einhorn (2003). "Fracture healing as a post-natal developmental process: Molecular, spatial, and temporal aspects of its regulation." Journal of Cellular Biochemistry **88**(5): 873-884.

Geyikoglu, F., H. Turkez, T. O. Bakir and M. Cicek (2013). "The genotoxic, hepatotoxic, nephrotoxic, haematotoxic and histopathological effects in rats after aluminium chronic intoxication." Toxicol Ind Health **29**(9): 780-791.

Glowacki, J. (1998). "Angiogenesis in fracture repair." Clin Orthop Relat Res(355 Suppl): S82-89.

Goldring, S. R. (2003). "Inflammatory mediators as essential elements in bone remodeling." Calcif Tissue Int **73**(2): 97-100.

Goodman, S. B., E. Gibon and Z. Yao (2013). "The basic science of periprosthetic osteolysis." Instr Course Lect **62**: 201-206.

Granero-Moltó, F., J. A. Weis, M. I. Miga, B. Landis, T. J. Myers, L. O'Rear, L. Longobardi, E. D. Jansen, D. P. Mortlock and A. Spagnoli (2009). "Regenerative Effects of Transplanted Mesenchymal Stem Cells in Fracture Healing." STEM CELLS **27**(8): 1887-1898.

Grillo, C. A., F. Alvarez and M. A. F. L. de Mele (2016). "Degradation of bioabsorbable Mg-based alloys: Assessment of the effects of insoluble corrosion products and joint effects of alloying components on mammalian cells." Materials Science & Engineering C-Materials for Biological Applications **58**: 372-380.

Gu, Q. L., Q. Shi and H. L. Yang (2012). "The Role of TLR and Chemokine in Wear Particle-Induced Aseptic Loosening." Journal of Biomedicine and Biotechnology.

Guan, X. M., M. P. Xiong, F. Y. Zeng, B. Xu, L. D. Yang, H. Guo, J. L. Niu, J. Zhang, C. X. Chen, J. Pei, H. Huang and G. Y. Yuan (2014). "Enhancement of Osteogenesis and Biodegradation Control by Brushite Coating on Mg-Nd-Zn-Zr Alloy for Mandibular Bone Repair." Acs Applied Materials & Interfaces **6**(23): 21525-21533.

Hadjidakis, D. J. and Androulakis, II (2006). "Bone remodeling." Ann N Y Acad Sci **1092**: 385-396.

Han, G., J.-Y. Lee, Y.-C. Kim, J. H. Park, D.-I. Kim, H.-S. Han, S.-J. Yang and H.-K. Seok (2012). "Preferred crystallographic pitting corrosion of pure magnesium in Hanks' solution." Corrosion Science **63**(0): 316-322.

Han, H.-S., Y.-Y. Kim, Y.-C. Kim, S.-Y. Cho, P.-R. Cha, H.-K. Seok and S.-J. Yang (2012). "Bone formation within the vicinity of biodegradable magnesium alloy implant in a rat femur model." Metals and Materials International **18**(2): 243-247.

Han, H.-S., S. Loffredo, I. Jun, J. Edwards, Y.-C. Kim, H.-K. Seok, F. Witte, D. Mantovani and S. Glyn-Jones (2018). "Current status and outlook on the clinical translation of biodegradable metals." Materials Today.

Han, P., P. F. Cheng, S. X. Zhang, C. L. Zhao, J. H. Ni, Y. Z. Zhang, W. R. Zhong, P. Hou, X. N. Zhang, Y. F. Zheng and Y. M. Chai (2015). "In vitro and in vivo studies on the degradation of high-purity Mg (99.99wt.%) screw with femoral intracondylar fractured rabbit model." Biomaterials **64**: 57-69.

Haynes, D. R., T. N. Crotti and H. Zreiqat (2004). "Regulation of osteoclast activity in peri-implant tissues." Biomaterials **25**(20): 4877-4885.

He, J. H., J. M. Gao, C. J. Huang and C. Q. Li (2014). "Zebrafish models for assessing developmental and reproductive toxicity." Neurotoxicol Teratol **42**: 35-42.

Henderson, S. E., K. Verdelis, S. Maiti, S. Pal, W. L. Chung, D. T. Chou, P. N. Kumta and A. J. Almarza (2014). "Magnesium alloys as a biomaterial for degradable craniofacial screws." Acta Biomaterialia **10**(5): 2323-2332.

Hornberger, H., S. Virtanen and A. R. Boccaccini (2012). "Biomedical coatings on magnesium alloys - a review." Acta Biomater **8**(7): 2442-2455.

Hort, N., Y. Huang, D. Fechner, M. Stormer, C. Blawert, F. Witte, C. Vogt, H. Drucker, R. Willumeit, K. U. Kainer and F. Feyerabend (2010). "Magnesium alloys as implant materials--principles of property design for Mg-RE alloys." Acta Biomater **6**(5): 1714-1725.

Huan, Z. G., M. A. Leeflang, J. Zhou, L. E. Fratila-Apachitei and J. Duszczyk (2010). "In vitro degradation behavior and cytocompatibility of Mg-Zn-Zr alloys." J Mater Sci Mater Med **21**(9): 2623-2635.

Huang, T., J. Cheng, D. Bian and Y. F. Zheng (2016). "Fe-Au and Fe-Ag composites as candidates for biodegradable stent materials." Journal of Biomedical Materials Research Part B-Applied Biomaterials **104**(2): 225-240.

Janssen, F. W., J. Oostra, A. Oorschot and C. A. van Blitterswijk (2006). "A perfusion bioreactor system capable of producing clinically relevant volumes of tissue-engineered bone: in vivo bone formation showing proof of concept." Biomaterials **27**(3): 315-323.

Jung, J.-Y., S.-J. Kwon, H.-S. Han, J.-Y. Lee, J.-P. Ahn, S.-J. Yang, S.-Y. Cho, P.-R. Cha, Y.-C. Kim and H.-K. Seok (2012). "In vivo corrosion mechanism by elemental interdiffusion of biodegradable Mg–Ca alloy." Journal of Biomedical Materials Research Part B: Applied Biomaterials **100B**(8): 2251-2260.

Kanungo, J., E. Cuevas, S. F. Ali and M. G. Paule (2014). "Zebrafish model in drug safety assessment." Curr Pharm Des **20**(34): 5416-5429.

Kelava, T., A. Sucur, S. Kuzmac and V. Katavic (2014). "Interactions between bone and immune systems: A focus on the role of inflammation in bone resorption and fracture healing." Periodicum Biologorum **116**(1): 45-52.

Ketenjian, A. Y. and C. Arsenis (1975). "Morphological and biochemical studies during differentiation and calcification of fracture callus cartilage." Clin Orthop Relat Res(107): 266-273.

Kim, H. J., U. J. Kim, G. G. Leisk, C. Bayan, I. Georgakoudi and D. L. Kaplan (2007). "Bone regeneration on macroporous aqueous-derived silk 3-D scaffolds." Macromol Biosci **7**(5): 643-655.

Kim, H. K., H. S. Han, K. S. Lee, D. H. Lee, J. W. Lee, H. Jeon, S. Y. Cho, H. J. Roh, Y. C. Kim and H. K. Seok (2017). "Comprehensive study on the roles of released ions from biodegradable Mg-5 wt% Ca-1 wt% Zn alloy in bone regeneration." J Tissue Eng Regen Med **11**(10): 2710-2724.

Kirkland, N. T., J. Lespagnol, N. Birbilis and M. P. Staiger (2010). "A survey of bio-corrosion rates of magnesium alloys." Corrosion Science **52**(2): 287-291.

Kolar, P., K. Schmidt-Bleek, H. Schell, T. Gaber, D. Toben, G. Schmidmaier, C. Perka, F. Buttgereit and G. N. Duda (2010). "The Early Fracture Hematoma and Its Potential Role in Fracture Healing." Tissue Engineering Part B-Reviews **16**(4): 427-434.

Kolar, P., K. Schmidt-Bleek, H. Schell, T. Gaber, D. Toben, G. Schmidmaier, C. Perka, F. Buttgereit and G. N. Duda (2010). "The early fracture hematoma and its potential role in fracture healing." Tissue Eng Part B Rev **16**(4): 427-434.

Kon, T., T.-J. Cho, T. Aizawa, M. Yamazaki, N. Nooh, D. Graves, L. C. Gerstenfeld and T. A. Einhorn (2001). "Expression of Osteoprotegerin, Receptor Activator of NF-κB Ligand (Osteoprotegerin Ligand) and Related Proinflammatory Cytokines During Fracture Healing." Journal of Bone and Mineral Research **16**(6): 1004-1014.

Kraus, T., S. F. Fischerauer, A. C. Hanzi, P. J. Uggowitzer, J. F. Loffler and A. M. Weinberg (2012). "Magnesium alloys for temporary implants in osteosynthesis: In vivo studies of their degradation and interaction with bone." Acta Biomaterialia **8**(3): 1230-1238.

Kraus, T., F. Moszner, S. Fischerauer, M. Fiedler, E. Martinelli, J. Eichler, F. Witte, E. Willbold, M. Schinhammer, M. Meischel, P. J. Uggowitzer, J. F. Loeffler and A. Weinberg (2014). "Biodegradable Fe-based alloys for use in osteosynthesis: Outcome of an in vivo study after 52 weeks." Acta Biomaterialia **10**(7): 3346-3353.

Kusumbe, A. P., S. K. Ramasamy and R. H. Adams (2014). "Coupling of angiogenesis and osteogenesis by a specific vessel subtype in bone." Nature **507**(7492): 323-328.

Laroche, M. (2002). "Intraosseous circulation from physiology to disease." Joint Bone Spine **69**(3): 262-269.

Lee, J. W., H. S. Han, K. J. Han, J. Park, H. Jeon, M. R. Ok, H. K. Seok, J. P. Ahn, K. E. Lee, D. H. Lee, S. J. Yang, S. Y. Cho, P. R. Cha, H. Kwon, T. H. Nam, J. H. Lo Han, H. J. Rho, K. S. Lee, Y. C. Kim and D. Mantovani (2016). "Long-term clinical study and multiscale analysis of in vivo biodegradation mechanism of Mg alloy." Proceedings of the National Academy of Sciences of the United States of America **113**(3): 716-721.

Lee, K. Y., G. H. Jang, C. H. Byun, M. Jeun, P. C. Searson and K. H. Lee (2017). "Zebrafish models for functional and toxicological screening of nanoscale drug delivery systems: promoting preclinical applications." Biosci Rep **37**(3).

Lee, S. K. and J. Lorenzo (2006). "Cytokines regulating osteoclast formation and function." Curr Opin Rheumatol **18**(4): 411-418.

Li, H. F., X. H. Xie, Y. F. Zheng, Y. Cong, F. Y. Zhou, K. J. Qiu, X. Wang, L. Huang, L. Tian and L. Qin (2015). "Development of biodegradable Zn-1X binary alloys with nutrient alloying elements Mg, Ca and Sr." Scientific Reports **5**(10719).

Li, M., P. He, Y. H. Wu, Y. Zhang, H. Xia, Y. F. Zheng and Y. Han (2016). "Stimulatory effects of the degradation products from Mg-Ca-Sr alloy on the osteogenesis through regulating ERK signaling pathway." Scientific Reports **6**.

Li, X., X. M. Liu, S. L. Wu, K. W. K. Yeung, Y. F. Zheng and P. K. Chu (2016). "Design of magnesium alloys with controllable degradation for biomedical implants: From bulk to surface." Acta Biomaterialia **45**: 2-30.

Li, Y., X. Q. Miao, T. K. Chen, X. Yi, R. B. Wang, H. T. Zhao, S. M. Y. Lee, X. Q. Wang and Y. Zheng (2017). "Zebrafish as a visual and dynamic model to study the transport of nanosized drug delivery systems across the biological barriers." Colloids and Surfaces B-Biointerfaces **156**: 227-235.

Li, Y. C., C. S. Wong, C. Wen and P. D. Hodgson (2012). "Biodegradable Mg-Zr-Ca alloys for bone implant materials." Materials Technology **27**(1): 49-51.

Li, Z., G.-L. Song and S. Song (2014). "Effect of bicarbonate on biodegradation behaviour of pure magnesium in a simulated body fluid." Electrochimica Acta **115**: 56-65.

Li, Z. J., X. N. Gu, S. Q. Lou and Y. F. Zheng (2008). "The development of binary Mg-Ca alloys for use as biodegradable materials within bone." Biomaterials **29**(10): 1329-1344.

Liu, C., X. K. Fu, H. B. Pan, P. Wan, L. Wang, L. L. Tan, K. H. Wang, Y. Zhao, K. Yang and P. K. Chu (2016). "Biodegradable Mg-Cu alloys with enhanced osteogenesis, angiogenesis, and long-lasting antibacterial effects." Scientific Reports **6**.

Liu, H. (2011). "The effects of surface and biomolecules on magnesium degradation and mesenchymal stem cell adhesion." J Biomed Mater Res A **99**(2): 249-260.

Liu, Y., Y. H. Wu, D. Bian, S. Gao, S. Leeflang, H. Guo, Y. F. Zheng and J. Zhou (2017). "Study on the Mg-Li-Zn ternary alloy system with improved mechanical properties, good degradation performance and different responses to cells." Acta Biomaterialia **62**: 418-433.

Liu, Y. K., Q. Z. Lu, R. Pei, H. J. Ji, G. S. Zhou, X. L. Zhao, R. K. Tang and M. Zhang (2009). "The effect of extracellular calcium and inorganic phosphate on the growth and osteogenic differentiation of mesenchymal stem cells in vitro: implication for bone tissue engineering." Biomed Mater **4**(2): 025004.

Ma, J., J. Ge, S. Zhang, A. Sun, J. Shen, L. Chen, K. Wang and Y. Zou (2005). "Time course of myocardial stromal cell–derived factor 1 expression and beneficial effects of intravenously administered bone marrow stem cells in rats with experimental myocardial infarction." Basic Research in Cardiology **100**(3): 217-223.

Maeno, S., Y. Niki, H. Matsumoto, H. Morioka, T. Yatabe, A. Funayama, Y. Toyama, T. Taguchi and J. Tanaka (2005). "The effect of calcium ion concentration on osteoblast viability, proliferation and differentiation in monolayer and 3D culture." Biomaterials **26**(23): 4847-4855.

Maes, C., S. Goossens, S. Bartunkova, B. Drogat, L. Coenegrachts, I. Stockmans, K. Moermans, O. Nyabi, K. Haigh, M. Naessens, L. Haenebalcke, J. P. Tuckermann, M. Tjwa, P. Carmeliet, V. Mandic, J. P. David, A. Behrens, A. Nagy, G. Carmeliet and J. J. Haigh (2010). "Increased skeletal VEGF enhances β-catenin activity and results in excessively ossified bones." The EMBO Journal **29**(2): 424-441.

Maes, C., T. Kobayashi, M. K. Selig, S. Torrekens, S. I. Roth, S. Mackem, G. Carmeliet and H. M. Kronenberg (2010). "Osteoblast Precursors, but Not Mature Osteoblasts, Move into Developing and Fractured Bones along with Invading Blood Vessels." Developmental Cell **19**(2): 329-344.

Marino, S., K. A. Staines, G. Brown, R. A. Howard-Jones and M. Adamczyk (2016). "Models of ex vivo explant cultures: applications in bone research." Bonekey Rep **5**: 818.

Marsell, R. and T. A. Einhorn (2009). "The role of endogenous bone morphogenetic proteins in normal skeletal repair." Injury **40**: S4-S7.

Marsell, R. and T. A. Einhorn (2011). "The biology of fracture healing." Injury **42**(6): 551-555.

Marsell, R. and T. A. Einhorn (2011). "The biology of fracture healing." Injury **42**(6): 551-555.

Marukawa, E., M. Tamai, Y. Takahashi, I. Hatakeyama, M. Sato, Y. Higuchi, H. Kakidachi, H. Taniguchi, T. Sakamoto, J. Honda, K. Omura and H. Harada (2016). "Comparison of magnesium alloys and poly-l-lactide screws as degradable implants in a canine fracture model." Journal of Biomedical Materials Research Part B-Applied Biomaterials **104**(7): 1282-1289.

McGrath, P. and C. Q. Li (2008). "Zebrafish: a predictive model for assessing drug-induced toxicity." Drug Discov Today **13**(9-10): 394-401.

Mert, F., C. Blawert, K. U. Kainer and N. Hort (2012). "Influence of cerium additions on the corrosion behaviour of high pressure die cast AM50 alloy." Corrosion Science **65**: 145-151.

Mohd Daud, N., N. B. Sing, A. H. Yusop, F. A. Abdul Majid and H. Hermawan (2014). "Degradation and in vitro cell–material interaction studies on hydroxyapatite-coated biodegradable porous iron for hard tissue scaffolds." Journal of Orthopaedic Translation **2**(4): 177-184.

Mostaed, E., M. Sikora-Jasinska, A. Mostaed, S. Loffredo, A. G. Demir, B. Previtali, D. Mantovani, R. Beanland and M. Vedani (2016). "Novel Zn-based alloys for biodegradable stent applications: Design, development and in vitro degradation." Journal of the mechanical behavior of biomedical materials **60**: 581-602.

Mountziaris, P. M. and A. G. Mikos (2008). "Modulation of the inflammatory response for enhanced bone tissue regeneration." Tissue Eng Part B Rev **14**(2): 179-186.

Mountziaris, P. M. and A. G. Mikos (2008). "Modulation of the inflammatory response for enhanced bone tissue regeneration." Tissue Engineering Part B-Reviews **14**(2): 179-186.

Mousa, H. M., K. H. Hussein, A. A. Raslan, J. Lee, H. M. Woo, C. H. Park and C. S. Kim (2016). "Amorphous apatite thin film formation on a biodegradable Mg alloy for bone regeneration: strategy, characterization, biodegradation, and in vitro cell study." Rsc Advances **6**(27): 22563-22574.

Murni, N. S., M. S. Dambatta, S. K. Yeap, G. R. A. Froemming and H. Hermawan (2015). "Cytotoxicity evaluation of biodegradable Zn-3Mg alloy toward normal human osteoblast cells." Materials Science & Engineering C-Materials for Biological Applications **49**: 560-566.

Nabiyouni, M., T. Bruckner, H. Zhou, U. Gbureck and S. B. Bhaduri (2018). "Magnesium-based bioceramics in orthopedic applications." Acta Biomaterialia **66**: 23-43.

Nakamura, S., T. Matsumoto, J. Sasaki, H. Egusa, K. Y. Lee, T. Nakano, T. Sohmura and A. Nakahira (2010). "Effect of calcium ion concentrations on osteogenic differentiation and hematopoietic stem cell niche-related protein expression in osteoblasts." Tissue Eng Part A **16**(8): 2467-2473.

Nerlich, A. G., A. Zink, U. Szeimies and H. G. Hagedorn (2000). "Ancient Egyptian prosthesis of the big toe." Lancet **356**(9248): 2176-2179.

Nich, C., Y. Takakubo, J. Pajarinen, M. Ainola, A. Salem, T. Sillat, A. J. Rao, M. Raska, Y. Tamaki, M. Takagi, Y. T. Konttinen, S. B. Goodman and J. Gallo (2013). "Macrophages-Key cells in the response to wear debris from joint replacements." J Biomed Mater Res A **101**(10): 3033-3045.

Niyibizi, C. and D. R. Eyre (1989). "Bone type V collagen: chain composition and location of a trypsin cleavage site." Connect Tissue Res **20**(1-4): 247-250.

Niyibizi, C. and D. R. Eyre (1994). "Structural characteristics of cross-linking sites in type V collagen of bone. Chain specificities and heterotypic links to type I collagen." Eur J Biochem **224**(3): 943-950.

Noviana, D., D. Paramitha, M. F. Ulum and H. Hermawan (2016). "The effect of hydrogen gas evolution of magnesium implant on the postimplantation mortality of rats." Journal of Orthopaedic Translation **5**: 9-15.

Park, J. B. and J. D. Bronzino (2002). Biomaterials: Principles and Applications, CRC Press.

Pietak, A., P. Mahoney, G. J. Dias and M. P. Staiger (2008). "Bone-like matrix formation on magnesium and magnesium alloys." Journal of Materials Science-Materials in Medicine **19**(1): 407-415.

Plaass, C., S. Ettinger, L. Sonnow, S. Koenneker, Y. Noll, A. Weizbauer, J. Reifenrath, L. Claassen, K. Daniilidis, C. Stukenborg-Colsman and H. Windhagen (2016). "Early results using a biodegradable magnesium screw for modified chevron osteotomies." Journal of Orthopaedic Research **34**(12): 2207-2214.

Pogorielov, M., E. Husak, A. Solodivnik and S. Zhdanov (2017). "Magnesium-based biodegradable alloys: Degradation, application, and alloying elements." Interventional Medicine and Applied Science **9**(1): 27-38.

Purdue, P. E., P. Koulouvaris, B. J. Nestor and T. P. Sculco (2006). "The central role of wear debris in periprosthetic osteolysis." HSS J **2**(2): 102-113.

Pyati, U. J., A. T. Look and M. Hammerschmidt (2007). "Zebrafish as a powerful vertebrate model system for in vivo studies of cell death." Seminars in Cancer Biology **17**(2): 154-165.

Qiao, Z., Z. Shi, N. Hort, N. I. Zainal Abidin and A. Atrens (2012). "Corrosion behaviour of a nominally high purity Mg ingot produced by permanent mould direct chill casting." Corrosion Science **61**: 185-207.

Radha, R. and D. Sreekanth (2017). "Insight of magnesium alloys and composites for orthopedic implant applications - a review." Journal of Magnesium and Alloys **5**(3): 286-312.

Raisz, L. G. (1999). "Physiology and pathophysiology of bone remodeling." Clinical Chemistry **45**(8B): 1353-1358.

Ramakrishna, S., J. Mayer, E. Wintermantel and K. W. Leong (2001). "Biomedical applications of polymer-composite materials: a review." Composites Science and Technology **61**(9): 1189-1224.

Ranjit, S., A. Dvornikov, M. Stakic, S.-H. Hong, M. Levi, R. M. Evans and E. Gratton (2015). "Imaging Fibrosis and Separating Collagens using Second Harmonic Generation and Phasor Approach to Fluorescence Lifetime Imaging." Scientific Reports **5**: 13378.

Reith, G., V. Schmitz-Greven, K. O. Hensel, M. M. Schneider, T. Tinschmann, B. Bouillon and C. Probst (2015). "Metal implant removal: benefits and drawbacks - a patient survey." Bmc Surgery **15**.

Riddle, R. C., R. Khatri, E. Schipani and T. L. Clemens (2009). "Role of hypoxia-inducible factor-1α in angiogenic–osteogenic coupling." Journal of Molecular Medicine **87**(6): 583-590.

Robling, A. G., A. B. Castillo and C. H. Turner (2006). "Biomechanical and molecular regulation of bone remodeling." Annu Rev Biomed Eng **8**: 455-498.

Rossig, C., N. Angrisani, P. Helmecke, S. Besdo, J. M. Seitz, B. Welke, N. Fedchenko, H. Kock and J. Reifenrath (2015). "In vivo evaluation of a magnesium-

based degradable intramedullary nailing system in a sheep model." Acta Biomaterialia **25**: 369-383.

Rubinstein, A. L. (2006). "Zebrafish assays for drug toxicity screening." Expert Opinion on Drug Metabolism & Toxicology **2**(2): 231-240.

Rucci, N. (2008). "Molecular biology of bone remodelling." Clinical Cases in Mineral and Bone Metabolism **5**(1): 49-56.

Sailon, A. M., A. C. Allori, E. H. Davidson, D. D. Reformat, R. J. Allen and S. M. Warren (2009). "A novel flow-perfusion bioreactor supports 3D dynamic cell culture." J Biomed Biotechnol **2009**: 873816.

Saris, N. E., E. Mervaala, H. Karppanen, J. A. Khawaja and A. Lewenstam (2000). "Magnesium. An update on physiological, clinical and analytical aspects." Clin Chim Acta **294**(1-2): 1-26.

Schaller, B., N. Saulacic, S. Beck, T. Imwinkelried, B. T. Goh, K. Nakahara, W. Hofstetter and T. Iizuka (2016). "In vivo degradation of a new concept of magnesium-based rivet-screws in the minipig mandibular bone." Materials Science & Engineering C-Materials for Biological Applications **69**: 247-254.

Schaller, B., N. Saulacic, S. Beck, T. Imwinkelried, E. W. Y. Liu, K. Nakahara, W. Hofstetter and T. Iizuka (2017). "Osteosynthesis of partial rib osteotomy in a miniature pig model using human standard-sized magnesium plate/screw systems: Effect of cyclic deformation on implant integrity and bone healing." Journal of Cranio-Maxillofacial Surgery **45**(6): 862-871.

Schinhammer, M., A. C. Hänzi, J. F. Löffler and P. J. Uggowitzer (2010). "Design strategy for biodegradable Fe-based alloys for medical applications." Acta Biomaterialia **6**(5): 1705-1713.

Seal, C. K., K. Vince and M. A. Hodgson (2009). "Biodegradable surgical implants based on magnesium alloys – A review of current research." IOP Conference Series: Materials Science and Engineering **4**: 012011.

Seitz, J. M., R. Eifler, F. W. Bach and H. J. Maier (2014). "Magnesium degradation products: Effects on tissue and human metabolism." Journal of Biomedical Materials Research Part A **102**(10): 3744-3753.

Seo, H. J., Y. E. Cho, T. Kim, H. I. Shin and I. S. Kwun (2010). "Zinc may increase bone formation through stimulating cell proliferation, alkaline phosphatase activity and collagen synthesis in osteoblastic MC3T3-E1 cells." Nutr Res Pract **4**(5): 356-361.

Sikavitsas, V. I., G. N. Bancroft, H. L. Holtorf, J. A. Jansen and A. G. Mikos (2003). "Mineralized matrix deposition by marrow stromal osteoblasts in 3D perfusion culture increases with increasing fluid shear forces." Proc Natl Acad Sci U S A **100**(25): 14683-14688.

Sikavitsas, V. I., J. S. Temenoff and A. G. Mikos (2001). "Biomaterials and bone mechanotransduction." Biomaterials **22**(19): 2581-2593.

Sims, N. A. and J. H. Gooi (2008). "Bone remodeling: Multiple cellular interactions required for coupling of bone formation and resorption." Seminars in Cell & Developmental Biology **19**(5): 444-451.

Sivaraj, K. K. and R. H. Adams (2016). "Blood vessel formation and function in bone." Development **143**(15): 2706-2715.

Song, G. (2007). "Control of biodegradation of biocompatable magnesium alloys." Corrosion Science **49**(4): 1696-1701.

Song, G. L. (2007). "Control of biodegradation of biocompatable magnesium alloys." Corrosion Science **49**(4): 1696-1701.

Song, W., C. W. Fhu, K. H. Ang, C. H. Liu, N. A. B. Johari, D. Lio, S. Abraham, W. Hong, S. E. Moss, J. Greenwood and X. Wang (2015). "The fetal mouse metatarsal bone explant as a model of angiogenesis." Nature Protocols **10**: 1459.

Staiger, M. P., A. M. Pietak, J. Huadmai and G. Dias (2006). "Magnesium and its alloys as orthopedic biomaterials: A review." Biomaterials **27**(9): 1728-1734.

Stevens, M. M. (2008). "Biomaterials for bone tissue engineering." Materials Today **11**(5): 18-25.

Sun, W., G. D. Zhang, L. L. Tan, K. Yang and H. J. Ai (2016). "The fluoride coated AZ31B magnesium alloy improves corrosion resistance and stimulates bone formation in rabbit model." Materials Science & Engineering C-Materials for Biological Applications **63**: 506-511.

Tie, D., F. Feyerabend, W. D. Muller, R. Schade, K. Liefeith, K. U. Kainer and R. Willumeit (2013). "Antibacterial biodegradable Mg-Ag alloys." Eur Cell Mater **25**: 284-298; discussion 298.

Toben, D., I. Schroeder, T. El Khassawna, M. Mehta, J. E. Hoffmann, J. T. Frisch, H. Schell, J. Lienau, A. Serra, A. Radbruch and G. N. Duda (2011). "Fracture Healing Is

Accelerated in the Absence of the Adaptive Immune System." Journal of Bone and Mineral Research **26**(1): 113-124.

Tomlinson, R. E. and M. J. Silva (2013). "Skeletal Blood Flow in Bone Repair and Maintenance." Bone Res **1**(4): 311-322.

Trueta, J. and J. D. Morgan (1960). "The vascular contribution to osteogenesis. I. Studies by the injection method." J Bone Joint Surg Br **42-B**: 97-109.

Ulum, M. F., A. Arafat, D. Noviana, A. H. Yusop, A. K. Nasution, M. R. A. Kadir and H. Hermawan (2014). "In vitro and in vivo degradation evaluation of novel iron-bioceramic composites for bone implant applications." Materials Science & Engineering C-Materials for Biological Applications **36**: 336-344.

Ulum, M. F., A. K. Nasution, A. H. Yusop, A. Arafat, M. R. A. Kadir, V. Juniantito, D. Noviana and H. Hermawan (2015). "Evidences of in vivo bioactivity of Fe-bioceramic composites for temporary bone implants." Journal of Biomedical Materials Research Part B-Applied Biomaterials **103**(7): 1354-1365.

Vandrovcova, M. and L. Bacakova (2011). "Adhesion, growth and differentiation of osteoblasts on surface-modified materials developed for bone implants." Physiol Res **60**(3): 403-417.

Venkatraman, S., F. Boey and L. L. Lao (2008). "Implanted cardiovascular polymers: Natural, synthetic and bio-inspired." Progress in Polymer Science **33**(9): 853-874.

Viguet-Carrin, S., P. Garnero and P. D. Delmas (2006). "The role of collagen in bone strength." Osteoporos Int **17**(3): 319-336.

Virtanen, S. (2011). "Biodegradable Mg and Mg alloys: Corrosion and biocompatibility." Materials Science and Engineering: B **176**(20): 1600-1608.

Vormann, J. (2003). "Magnesium: nutrition and metabolism." Mol Aspects Med **24**(1-3): 27-37.

Vormann, J. (2003). "Magnesium: nutrition and metabolism." Molecular aspects of medicine **24**(1): 27-37.

Vos, D. I. and M. H. J. Verhofstad (2013). "Indications for implant removal after fracture healing: a review of the literature." European Journal of Trauma and Emergency Surgery **39**(4): 327-337.

Waizy, H., J. Diekmann, A. Weizbauer, J. Reifenrath, I. Bartsch, V. Neubert, R. Schavan and H. Windhagen (2014). "In vivo study of a biodegradable orthopedic screw (MgYREZr-alloy) in a rabbit model for up to 12 months." J Biomater Appl **28**(5): 667-675.

Wang, J., V. Giridharan, V. Shanov, Z. Xu, B. Collins, L. White, Y. Jang, J. Sankar, N. Huang and Y. Yun (2014). "Flow-induced corrosion behavior of absorbable magnesium-based stents." Acta Biomater **10**(12): 5213-5223.

Wang, J., Y. Jang, G. Wan, V. Giridharan, G. L. Song, Z. Xu, Y. Koo, P. Qi, J. Sankar, N. Huang and Y. Yun (2016). "Flow-induced corrosion of absorbable magnesium alloy: In-situ and real-time electrochemical study." **104**: 277-289.

Wang, J. L., J. K. Xu, W. M. Fu, W. X. Cheng, K. M. Chan, P. S. H. Yung and L. Qin (2017). "Biodegradable Magnesium Screws Accelerate Fibrous Tissue Mineralization at the Tendon-Bone Insertion in Anterior Cruciate Ligament Reconstruction Model of Rabbit." Scientific Reports **7**.

Wang, J. L., J. K. Xu, W. C. Liu, Y. D. Li and L. Qin (2016). "Biodegradable Magnesium (Mg) Implantation Does Not Impose Related Metabolic Disorders in Rats with Chronic Renal Failure." Scientific Reports **6**.

Wang, T., J. C. Zhang, Y. Chen, P. G. Xiao and M. S. Yang (2007). "Effect of zinc ion on the osteogenic and adipogenic differentiation of mouse primary bone marrow stromal cells and the adipocytic trans-differentiation of mouse primary osteoblasts." J Trace Elem Med Biol **21**(2): 84-91.

Weinans, H., R. Huiskes and H. J. Grootenboer (1992). "Effects of Material Properties of Femoral Hip Components on Bone Remodeling." Journal of Orthopaedic Research **10**(6): 845-853.

Wendeberg, B. (1961). "Mineral metabolism of fractures of the tibia in man studied with external counting of Sr85." Acta Orthop Scand Suppl **52**: 1-79.

Windhagen, H., K. Radtke, A. Weizbauer, J. Diekmann, Y. Noll, U. Kreimeyer, R. Schavan, C. Stukenborg-Colsman and H. Waizy (2013). "Biodegradable magnesium-based screw clinically equivalent to titanium screw in hallux valgus surgery: short term results of the first prospective, randomized, controlled clinical pilot study." Biomed Eng Online **12**: 62.

Witte, F. (2010). "The history of biodegradable magnesium implants: a review." Acta Biomater **6**(5): 1680-1692.

Witte, F., N. Hort, C. Vogt, S. Cohen, K. U. Kainer, R. Willumeit and F. Feyerabend (2008). "Degradable biomaterials based on magnesium corrosion." Current Opinion in Solid State and Materials Science **12**(5-6): 63-72.

Witte, F., V. Kaese, H. Haferkamp, E. Switzer, A. Meyer-Lindenberg, C. J. Wirth and H. Windhagen (2005). "In vivo corrosion of four magnesium alloys and the associated bone response." Biomaterials **26**(17): 3557-3563.

Wynn, T. A. (2008). "Cellular and molecular mechanisms of fibrosis." J Pathol **214**(2): 199-210.

Xia, Z. and J. T. Triffitt (2006). "A review on macrophage responses to biomaterials." Biomedical Materials **1**(1): R1-R9.

Yang, C., G. Yuan, J. Zhang, Z. Tang, X. Zhang and K. Dai (2010). "Effects of magnesium alloys extracts on adult human bone marrow-derived stromal cell viability and osteogenic differentiation." Biomed Mater **5**(4): 045005.

Yang, X., B. F. Ricciardi, A. Hernandez-Soria, Y. Shi, N. Pleshko Camacho and M. P. G. Bostrom (2007). "Callus mineralization and maturation are delayed during fracture healing in interleukin-6 knockout mice." Bone **41**(6): 928-936.

Yeatts, A. B. and J. P. Fisher (2011). "Bone tissue engineering bioreactors: dynamic culture and the influence of shear stress." Bone **48**(2): 171-181.

Yun, Y., Z. Y. Dong, D. E. Yang, M. J. Schulz, V. N. Shanov, S. Yarmolenko, Z. G. Xu, P. Kumta and C. Sfeir (2009). "Biodegradable Mg corrosion and osteoblast cell culture studies." Materials Science & Engineering C-Materials for Biological Applications **29**(6): 1814-1821.

Yusop, A. H. M., N. M. Daud, H. Nur, M. R. A. Kadir and H. Hermawan (2015). "Controlling the degradation kinetics of porous iron by poly(lactic-co-glycolic acid) infiltration for use as temporary medical implants." Scientific Reports **5**.

Zberg, B., P. J. Uggowitzer and J. F. Löffler (2009). "MgZnCa glasses without clinically observable hydrogen evolution for biodegradable implants." Nature Materials **8**(11): 887-891.

Zeng, R. C., W. Dietzel, F. Witte, N. Hort and C. Blawert (2008). "Progress and challenge for magnesium alloys as biomaterials." Advanced Engineering Materials **10**(8): B3-B14.

Zhang, B. P., Y. Wang and L. Geng (2011). "Research on Mg-Zn-Ca Alloy as Degradable Biomaterial." Biomaterials - Physics and Chemistry: 183-204.

Zhang, Y., J. Xu, Y. C. Ruan, M. K. Yu, M. O'Laughlin, H. Wise, D. Chen, L. Tian, D. Shi, J. Wang, S. Chen, J. Q. Feng, D. H. Chow, X. Xie, L. Zheng, L. Huang, S. Huang, K. Leung, N. Lu, L. Zhao, H. Li, D. Zhao, X. Guo, K. Chan, F. Witte, H. C. Chan, Y. Zheng and L. Qin (2016). "Implant-derived magnesium induces local neuronal production of CGRP to improve bone-fracture healing in rats." Nat Med **22**(10): 1160-1169.

Zhao, D. L., T. T. Wang, K. Nahan, X. F. Guo, Z. P. Zhang, Z. Y. Dong, S. N. Chen, D. T. Chou, D. H. Hong, P. N. Kumta and W. R. Heineman (2017). "In vivo characterization of magnesium alloy biodegradation using electrochemical H-2 monitoring, ICP-MS, and XPS." Acta Biomaterialia **50**: 556-565.

Zhao, D. W., S. B. Huang, F. Q. Lu, B. J. Wang, L. Yang, L. Qin, K. Yang, Y. D. Li, W. R. Li, W. Wang, S. M. Tian, X. Z. Zhang, W. B. Gao, Z. P. Wang, Y. Zhang, X. H. Xie, J. L. Wang and J. L. Li (2016). "Vascularized bone grafting fixed by biodegradable magnesium screw for treating osteonecrosis of the femoral head." Biomaterials **81**: 84-92.

Zhao, D. W., F. Witte, F. Q. Lu, J. L. Wang, J. L. Li and L. Qin (2017). "Current status on clinical applications of magnesium-based orthopaedic implants: A review from clinical translational perspective." Biomaterials **112**: 287-302.

Zhao, N. and D. Zhu (2015). "Endothelial responses of magnesium and other alloying elements in magnesium-based stent materials." Metallomics **7**(1): 118-128.

Zheng, Y. F., X. N. Gu and F. Witte (2014). "Biodegradable metals." Materials Science & Engineering R-Reports **77**: 1-34.

Zreiqat, H., C. R. Howlett, A. Zannettino, P. Evans, G. Schulze-Tanzil, C. Knabe and M. Shakibaei (2002). "Mechanisms of magnesium-stimulated adhesion of osteoblastic cells to commonly used orthopaedic implants." J Biomed Mater Res **62**(2): 175-184.

Appendix

Protocol for Fetal Mouse Metatarsal Assay

This protocol is based on protocol published by Song, Fhu et al. (2015).

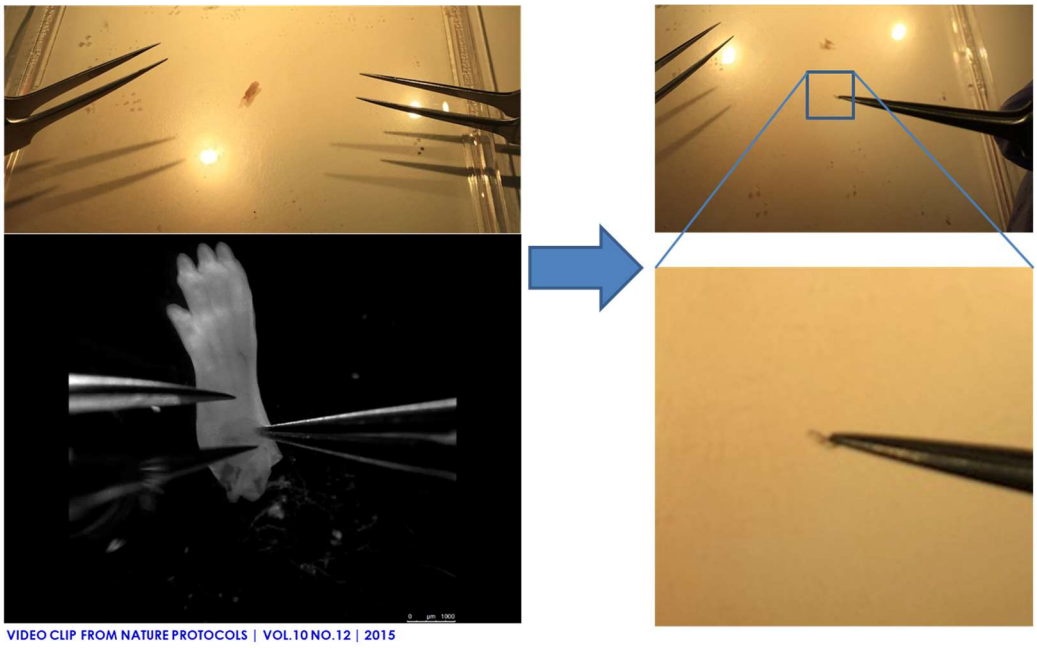
Materials:

- **Gelatin solution (0.1%)**
  Add 0.1 g gelatin (Type A, from porcine skin, Sigma G1890 from chemical room) in 100 mL of autoclaved distilled H_2O. Heat it up on microwave on medium-high power for 2-4 min to dissolve the gelatin, and filter the solution with a 0.2-µm syringe filter under the sterile hood.
- **Cold Dissection medium**
  Add 10% FBS to sterile 1X PBS and keep it on ice. Prepare fresh medium every time.
- **Culture medium**
  Add 10% of heat inactivated FBS to MEMα medium containing antibiotics (1X penicillin/Strep)
- **Dissection tools**
  Two pairs of tweezers, scissors and forceps must be autoclaved prior to use.
- **Ethanol (70%)**
  Dilute absolute ethanol in dH_2O and must be stored at room temperature.

- **Paraformaldehyde (4%, wt/vol)**
  Dissolve 2 g of PFA in 50 ml of 1× PBS by heating the solution to 60 °C in a magnetic stirrer system. Every time prepare fresh PFA and keep it on ice.

Procedure:

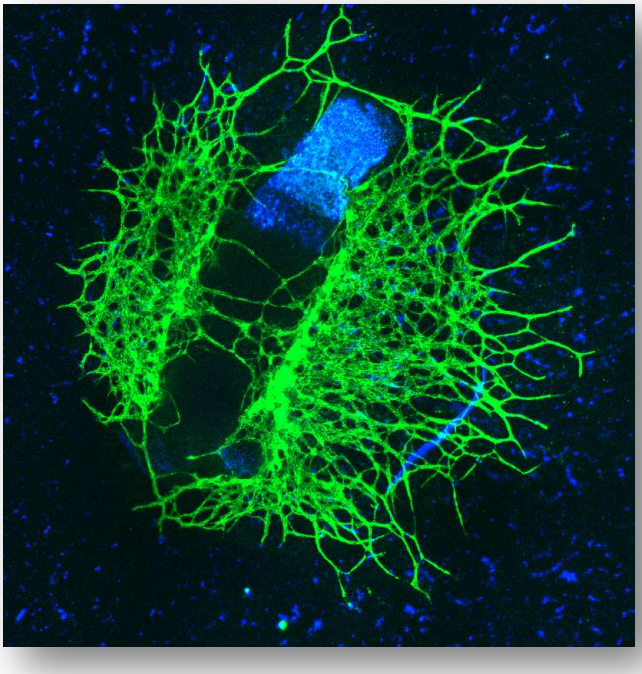
1. Coat each well of a 24-well plate with 300 µl of freshly prepared gelatin coating solution and keep the coated plate on incubator (37 °C) overnight prior to the assay begins.
2. Next day morning remove the gelatin and wash the wells once with cold sterile 1X PBS and put back the plate in incubator.
3. Choose the pregnant dam at the desired gestational stage E15.5 to E18.5 and bring it to the procedure room and cull it by cervical dislocation.
4. Surface-sterilize the mouse with 70% ethanol.
5. Open the abdominal cavity with a single cut using sterile scissors to expose the uterus.
6. Transfer the uterine horns into a 10-cm culture dish containing ice-cold dissection medium, and then place the culture dish on ice.
7. Cut between each sac to separate individual fetuses. Sever each sac with tweezers and separate the fetuses from the placentas.
8. Transfer the fetus under a dissection stereomicroscope, cut the feet off just above the ankle joint and transfer the feet with tweezers to a fresh 10-cm culture dish containing ice-cold dissection medium.
9. Grasp the exposed fibula with one pair of tweezers. Gently insert the other pair of tweezers between the calcaneus and the skin, and advance into the footpad. Pull the skin off as if removing a glove. Phalanges will be removed together with the skin, leaving metatarsals and tarsals intact
10. Hold the tarsals with one pair of tweezers and remove excessive connective tissue left underneath the metatarsals.
11. Hold tarsals with one pair of tweezers, and use the other pair to separate neighbouring metatarsals. Remove the first and fifth metatarsals, only use middle 3 metatarsals for the culture.



Appendix Figure 1. Surgically removed metatarsal from the feet of fetal mouse

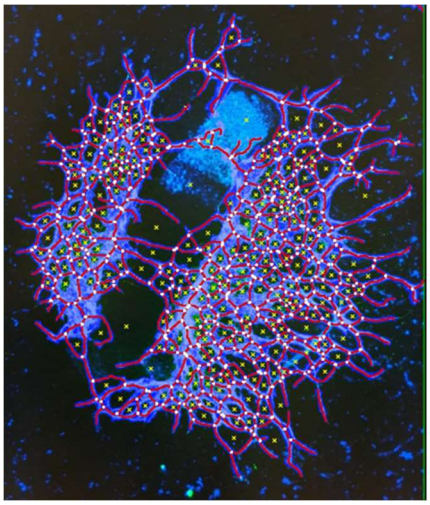
12. Transfer the isolated metatarsals to a fresh 10-cm culture dish containing ice-cold dissection medium
13. Takeout the coated 24 well plate from incubator and wash the plate with 250 µl of culture medium.
14. Place each metatarsal at the centre of each wells.
15. Gently remove any excess dissection solution that was transferred with metatarsals, and allow the metatarsals to adhere for 5 min inside the cell culture hood.
16. Slowly feed the metatarsals with 200 µl of culture medium.
17. Carefully place the culture plate at the incubator at 37 °C with 5% CO_2.
18. On day 2 onwards fibroblasts will start grow around the metatarsal.
19. Metal ion treatment can be started from day 2.
20. From day 3 vessel outgrowths will start appear and will be more evident on day 7.
21. On day 7, remove culture medium wash metatarsal gently and slowly using sterile PBS

22. Then fix the metatarsal using freshly prepared 4%PFA for 20 minutes at room temperature.
23. Remove PFA and wash wells slowly with sterile PBS twice
24. Store the metatarsal in sterile PBS at 4°C until use
25. Stain the sprouting blood vessels with CD31 antibody



Appendix Figure 2. Staining of CD31 showing sprouting blood vessels from metatarsal after 5 days of culture

26. Observe the growth of the blood vessel using confocal microscope
27. Upload the image on image processing software



Global Metrics			
Vessels Density [%]	Vessels Area [px]	ROI Area [px]	Total Branching Points
19.4	178768	922071	549

Vessel Segments Characteristics			
Total Vessels Length [px]	Total Segments	Mean Segment Length [px]	Standard Deviation Segment Length [px]
17244.69	803	21.48	15.33

Loop Characteristics				
Total Loops	Mean Loop Area [px]	Standard Deviation Loop Area [px]	Mean Loop Perimeter [px]	Standard Deviation Loop Perimeter [px]
248	335.69	1060.9	64.8	74.06

Appendix Figure 3. Processed image and generated data from new blood vessels using Wimasis angiogenesis analysis platform